UNIVERSITY OF CALIFORNIA,
IRVINE

Relativistic Laser-Solid Interactions Driven by Multiple Wavelengths

THESIS

submitted in partial satisfaction of the requirements
for the degree of

DOCTOR OF PHILOSOPHY

in Chemical and Materials Physics - Physics

by

Nicholas F. Beier

Thesis Committee:
Professor Franklin Dollar, Chair
Professor Roger McWilliams
Professor Christopher P. J. Barty

2021

DEDICATION

I dedicate this thesis to my parents.
For always loving, supporting, and encouraging me to pursue what I find most interesting.

TABLE OF CONTENTS

LIST OF FIGURES

LIST OF TABLES

ACKNOWLEDGMENTS

I would like to thank my advisor Professor Franklin Dollar for introducing me to the sometimes frustrating and always exciting world of laser-plasma physics. I am thankful for his his expertise, guidance, and willingness to spend countless hours in the lab or discussing physics. I had the fortune of joining a lab that was just beginning to start setup experiments. It was an invaluable experience to be able to design and build so many different diagnostics and experimental setups. I am grateful for the opportunities you provided me to go experience collaborative science both in our own group as well as across universities. Finally, thank you for always insisting that I need to meditate on the Fourier transform, because I almost certainly do.

I would like to thank Professor Roger McWilliams for our many impromptu (or perhaps entirely expected) discussions of physics, and for keeping my head out of the rabbit hole that is graduate research. I would also like to thank Professor Christopher Barty for insightful conversations about lasers from both a theoretical and practical side. I would like to thank Professor Amina Hussein both for being a great mentor as a postdoctoral research in our group, and for giving me the opportunity to participate in the LaserNetUS experiment.

Much of the experimental research carried out in this thesis would not be possible without access to external facilities through collaboration. A portion of this research was performed at the University of Michigan on the Lambda-cubed laser. I would like to thank Professor Karl Krushelnick for the opportunity and always great advice on where to look next, John Nees for teaching me how to start-up a laser and put together pellicles with just your ears, and Jinpu Lin for conducting the experiments every day with Tam and me. While not directly relevant to research in this thesis, I would like to thank some other members of the University of Michigan: Professor Alec Thomas, Professor Louise Willingale, Anatoly Maksimchuk, and Yong Ma. I would also like to thank Professor Jorge Rocca, Huanyu Song, Shoujun Wang, Reed Hollinger, and Ryan Netbailo of Colorado State University. Thank you for your willingness to accommodate the extraneous circumstances by allowing me to come alone to CSU during the height of the Covid-19 pandemic. Without your constant assistance and expertise our experiment would not have been possible.

My undergraduate research experience played a large role in my development as a researcher. I would like to thank my undergraduate research advisor Dr. Richard Haglund. In his lab I was able to get my first exposure to experimental research, and become familiar with the basics of optics. I would also like to thank the various graduate students who helped mentor me during this time, and specifically my partner-in-crime Christina McGahan for our late nights spent fabricating plasmonic devices.

I would like to thank my friends and colleagues who have supported me over the years. Michael, Mishu, Cody, Anna, Jake, Brian, Drew, and everyone else from UCI, thank you for helping to make Irvine a home for five years. Tam and Deano, thank you for teaching me the ropes of how to perform an experiment. Danny, Chris, and Yasmeen, thank you for listening to my convoluted explanations and for dealing with me constantly disassembling

your setups. Matt, Sahel, and Hunter, thank you for spending the countless late nights in lab together in our efforts to collect even a small amount of data. Finally, thank you Taylor, Michael, Nick, Sigi, and William for the continuous shenanigans we have gone through over the years.

Finally, and most of all, I would like to thank my family. Thank you Mom and Dad for the constant encouragement and support of my interests growing up. David, Kate, and Ben thank you for putting up with me being your older brother.

This work was funded by: the U.S. Department of Energy through the National Science Foundation (CAREER: National Science Foundation under Grant No. PHY-1753165; STROBE: A National Science Foundation Science & Technology Center under Grant No. DMR-1548924) and the Office of Fusion Energy Sciences and Lawrence Livermore National Lab under Sub-Contract B643845, and the Air Force Office of Science and Research under Grant No. FA9550-16-1-0121. I would like to acknowledge the OSIRIS consortium of UCLA and IST Portugal for the use of the OSIRIS 4.0 framework. Simulations were performed on the Green Planet cluster at the University of California, Irvine (supported by NSF Grant CHE-0840513).

CURRICULUM VITAE

Nicholas F. Beier

Education

University of California, Irvine — **Irvine, CA**
Ph.D. in Physics - Chemical and Materials Physics (ChaMP) — September 2021
Advisor: Professor Franklin Dollar
M.S. in Physics - Chemical and Materials Physics (ChaMP) — December 2020

Vanderbilt University — **Nashville, TN**
B.A. in Physics, *cum Laude*, with Highest Honors — May 2016
Minors in Mathematics and Scientific Computing
Honors Thesis Advisor: Professor Richard Haglund

Refereed Journal Publications

1. M. Stanfield, **N. F. Beier**, S. Hakimi, H. Allison, D. Farinella, A. E. Hussein, T. Tajima, and F. Dollar. *Millijoule few-cycle pulses from staged compression for strong and high field science*, Optics Express **29**, 6 (2021)

2. Y. Ma, D. Seipt, A. E. Hussein, S. Hakimi, **N. F. Beier**, S. B. Hansen, J. Hinojosa, A. Maksimchuk, J. Nees, K. Krushelnick, A. G. R. Thomas, and F. Dollar. *Enhanced Self-Injection by Above Threshold Ionization Heating in a Laser Wakefield Accelerator*, Physical Review Letters **124**, 11 (2020)

3. D. M. Farinella, M. Stanfield, **N. Beier**, T. Nguyen, S. Hakimi, T. Tajima, F. Dollar, J. Wheeler and G. Mourou. *Demonstration of thin film compression for short-pulse X-ray generation*, International Journal of Modern Physics A Vol. 34, No. 34, 1943015 (2019)

4. **N. Beier**, T. Nguyen, J. Lin, J. Nees, K. Krushelnick, F. Dollar. *Relativistic short-pulse high harmonic generation at 1.3 and 2.1 micron wavelengths*, New Journal of Physics **21**, 4 (2019)

5. D. M. Farinella, J. Wheeler, A. E. Hussein, J. Nees, M. Stanfield, **N. Beier**, Y. Ma, G. Cojocaru, R. Ungureanu, M. Pittman, J. Demailly, E. Baynard, R. Fabbri, M. Masruri, R. Secareanu, A. Naziru, R. Dabu, A. Maksimchuk, K. Krushelnick, D. Ros, G. Mourou, T. Tajima, and F. Dollar. *Focusability of laser pulses at petawatt transport intensities in thin-film compression*, Journal of the Optical Society of America B **36**, 2 (2019)

Conference Proceedings

1. M. Stanfield, H. Allison, **N. F. Beier**, S. Hakimi, A. E. Hussein, F. Dollar. *Few Cycle EUV Continuum Generation via Thin Film Compression*, Conference on Lasers and Electro-Optics (2020).

Conference and Workshop Presentations

1. **Talk: N. F. Beier**, Y. Heffes, H. Allison, M. Stanfield, Y. Musthafa, S. Hakimi, A. E. Hussein, F. Dollar. *The Role of Polarization in Relativistic High Harmonic Generation*, 62nd Annual Meeting of the APS Division of Plasma Physics, Remote, November 2020

2. **Poster: N. Beier**, M. Stanfield, H. Allison, S. Hakimi, T. Nguyen, A. Hussein, J. Lin, J. Nees, K. Krushelnick, F. Dollar. *Platform for kilohertz relativistic laser-solid interactions*, NIF and JLF User Group Meeting, Lawrence Livermore National Lab, CA, February 2020

3. **Talk: N. Beier**, T. Nguyen, J. Lin, M. Stanfield, H. Allison, S. Hakimi, J. Nees, K. Krushelnick, F. Dollar. *Mid-Infrared High-order Laser-Plasma Interactions in Solids*, 61th Annual Meeting of the APS Division of Plasma Physics, Fort Lauderdale, FL, October 2019

4. **Poster: N. Beier**, T. Nguyen, J. Lin, H. Allison, D. Farinella, S. Hakimi, M. Stanfield, J. Nees, K. Krushelnick, and F. Dollar. *Mid-Infrared High-order Laser Plasma Interactions in Solids*, High Energy Density Summer School, San Diego, CA, August 2019.

5. **Poster:** T. Nguyen, **N. Beier**, J. Lin, H. Allison, D. Farinella, S. Hakimi, M. Stanfield, J. Nees, K. Krushelnick, and F. Dollar. *Mid-Infrared High-order Laser Plasma Interactions in Solids*, 60th Annual Meeting of the APS Division of Plasma Physics, Portland, OR, November 2018
   **Presented Poster*

ABSTRACT OF THE THESIS

Relativistic Laser-Solid Interactions Driven by Multiple Wavelengths

By

Nicholas F. Beier

Doctor of Philosophy in Chemical and Materials Physics - Physics

University of California, Irvine, 2021

Professor Franklin Dollar, Chair

This thesis presents an experimental and computational study of relativistically-intense, laser-plasma interactions driven at wavelengths ranging from 400 - 2100 nm. Studying such interactions gives us insight to the complex interplay between high electromagnetic fields and relativistically-moving charged particles. The recent development of high peak-power, ultrafast laser systems has enabled the exploration of relativistic laser-plasma interactions with table-top systems at high repetition rates.

In this thesis, relativistically driven harmonics of infrared light sources (1.3μm and 2.1μm) were experimentally observed using solid density targets. The harmonic dependence on the driving laser polarization was measured by polarization measurements of the output harmonics up to the sixth harmonic. The introduction of a second, non-commensurate beam provides additional control over the relativistic harmonics, which are governed by the electron critical surface during the interaction. Finally, copper foils irradiated at intensities $> 10^{21}\mathrm{W/cm}^2$ indicate that thin, < 5 μm thick targets may be uniformly heated to temperatures exceeding 3 keV while remaining near solid density through the use of K-shell x-ray spectroscopy as part of a LaserNetUS experiment at the ALEPH laser facility.

Chapter 1

Introduction

The invention of the laser in 1960 [7] can be viewed as the advent of an explosion of scientific production on par with that of the RF accelerator of the early 20th century. The extraordinarily bright, coherent light provided by laser systems enabled the study of charged particles interacting with strong electric fields. Due to their high spatial coherence, some lasers can be focused to diffraction-limited spot sizes on the order of a few microns. Only one year after the first lasers were demonstrated, the field of nonlinear optics was born with the realization of second harmonic generation using a ruby laser [8]. Since then, there has been a constant push to expand the investigation of nonlinear laser-matter interactions. Nonlinear interactions have strong intensity-dependence, thus the requirement for high peak power lasers that can be tightly focused has been a driving force behind laser development.

The development of high-power, short-pulse[1] laser technology through chirped pulse amplification [9] has enabled the generation of focal intensities in which the laser electric field strength exceeds those of the atomic systems. The interaction of such high-intensity lasers with matter generates high energy density (HED) states with extremes in temperature and density. Simultaneously, the laser field strengths are capable of driving electron velocities

[1] In the context of this thesis "short-pulse" or "ultrafast" are defined as pulse durations $\tau \leq 100$ fs

to near the speed of light, producing highly-nonlinear motion in the laser focal region. The accelerating charged particles from laser-plasma interactions emit radiation, which opens up the possibility of high brightness, short pulse duration ultraviolet and x-ray sources. Modern, commercially-available, Ti:Sapphire-based laser systems enable the investigation of high-intensity, laser-plasma interactions that deliver only a few millijoules of energy in tens of femtoseconds. This thesis focuses on the investigation of high-intensity, laser-solid interactions carried out on both high-repetition rate, mJ systems as well as mid-scale, petawatt-class laser facilities. The following sections will act as a short survey of relevant information pertaining to this thesis work.

1.1 Pulsed Laser Technology

Immediately after the first lasers were demonstrated, laser peak power has been systematically increased by dramatically increasing laser pulse energy and decreasing pulse durations. The first pulsed lasers were realized through the modulation of the laser cavity quality-factor (Q-switching) to release pulses on the nanosecond timescale with megawatt pulse power [10]. In 1964, the realization of locking the longitudinal modes of the laser (mode-locking) enabled the pulse duration to be reduced by a factor of a thousand, down to the picosecond range, bringing the peak pulse power up to the gigawatt level [11, 12]. However, after mode-locking the increase in laser intensity advanced quite slowly as seen in Fig. 1.1.

At this point, the intensities produced through the amplification of short pulsed laser were approaching levels where nonlinear corrections to the index of refraction due to laser intensity ($\mathrm{GW/cm^2}$) becomes significant through a process known as the optical Kerr effect ($n = n_0 + n_2 I$). This nonlinear effect leads to catastrophic self-focusing and beam filamentation [13]. If self-focusing occurs inside of the optical components comprising the laser system then damage would occur quickly [14]. Since it was impossible to increase the pulse power any further, the

only method of increasing pulse energy was through increasing the laser beam size, resulting in systems becoming larger and thus more expensive. Eventually, practical considerations such as developing optics and gain media of certain diameters became prohibitive. Further, efficient laser energy extraction occurs when laser fluence matches the saturation fluence of the amplification material. Typically the saturation fluence for solid state laser materials ranges between 1 and 10 J/cm^2. Therefore, only nanosecond laser systems could be efficiently amplified without catastrophic self-focusing. Short-pulse (femtosecond) amplification was limited to materials with low saturation fluence ($F_{\text{sat}} \sim 10^{-3}$J/cm^2) to prevent material damage [14]. In the time between the discovery of mode-locking and the mid-1980s, numerous theoretical papers discussed the possible scientific discoveries that would be made possible with significantly higher peak powers, most notably Tajima and Dawson in 1979 proposed the laser wakefield accelerator which is achieved through the acceleration of trapped electrons by the plasma wave formed in the wake of an intense laser pulse [15].

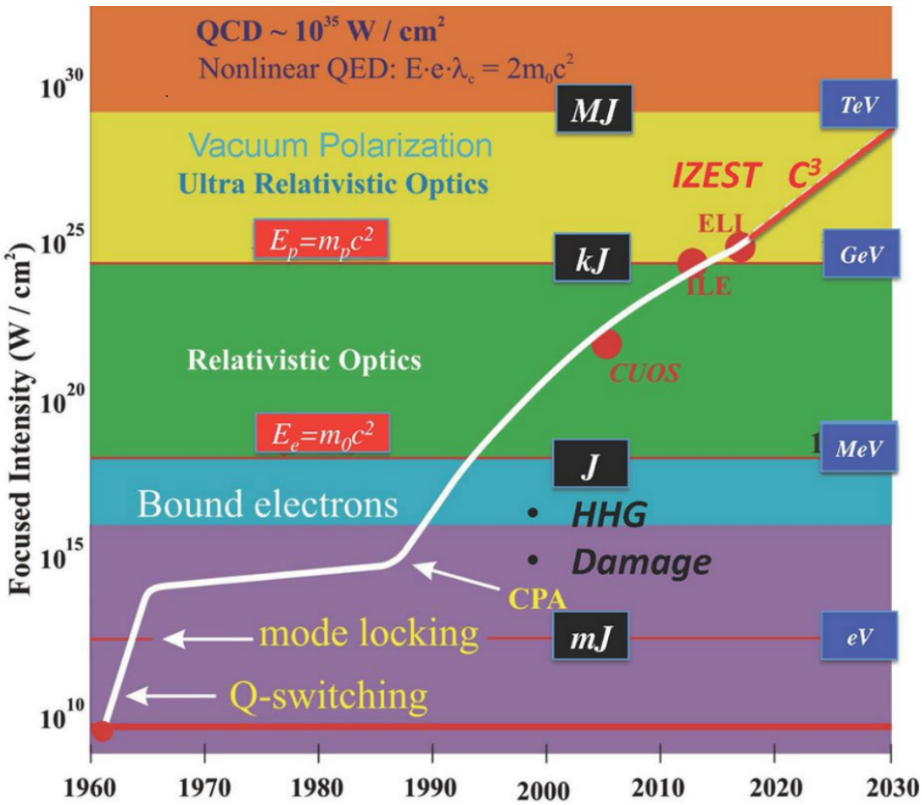

Figure 1.1: The evolution of peak laser intensity, i.e. peak laser power, as a function of time. Image credit: [1]

1.1.1 Chirped Pulse Amplification

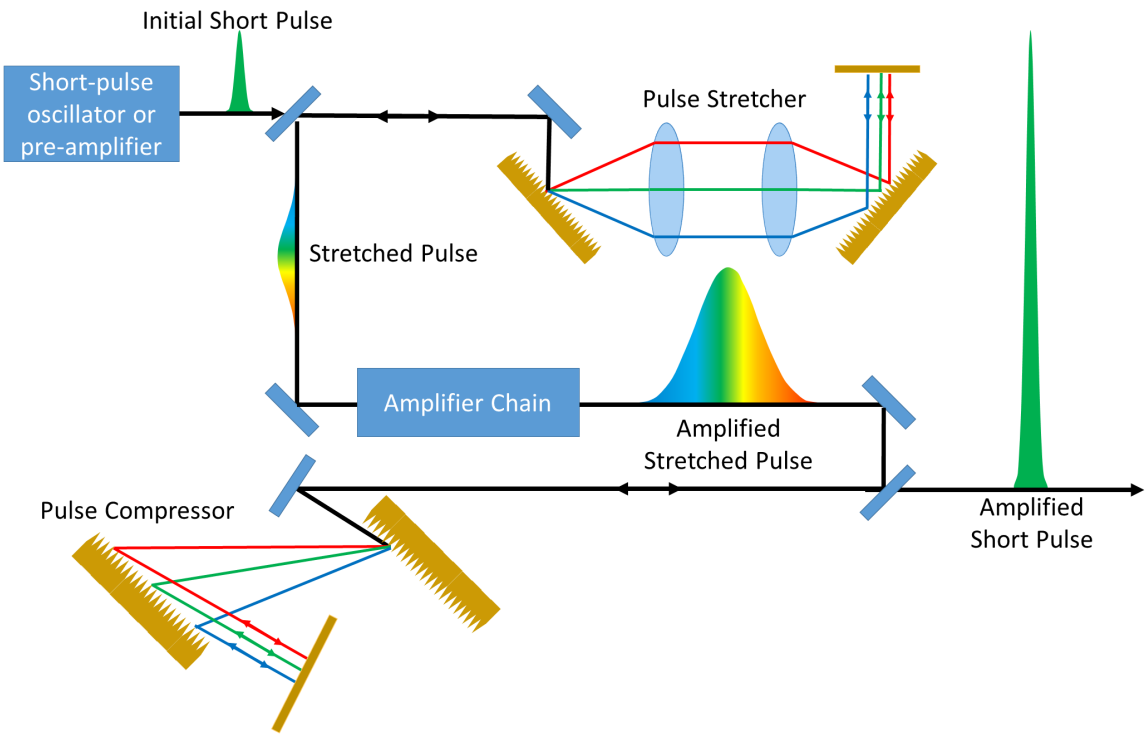

Figure 1.2: Example of Chirped Pulse Amplification. An initially ultrashort high power laser pulse is stretched many orders of magnitude allowing it to be amplified without introducing nonlinearity and damage to the amplification medium. The pulse undergoes amplification until reaching the saturation fluence of the amplifying medium. The pulse is subsequently re-compressed to near transform limit with dramatically increased peak power.

The invention of chirped-pulse amplification (CPA) [9] in 1985, which developed the solution to the short pulse amplification problem, can be viewed as a revolution for the field of nonlinear optics. CPA provided a rapid increase in ultrafast, high-power laser systems ranging from the petawatt-class facility-scale systems to commercial millijoule lasers available on the tabletop. The clever trick developed by Strickland and Mourou is through stretching a femtosecond pulse by dispersive elements, typically with diffraction gratings today, to several tens or hundreds of picoseconds. The pulse stretching drops the pulse power, and peak intensity, of the laser by many orders of magnitude. Some CPA systems[2] increase the beam diameter throughout the amplification chain, which further reduces the pulse inten-

[2]While petawatt-class lasers are the most obvious example, even the millijoule laser at UCI increases the beam diameter from 2-3 mm to 13 mm before recompression to help reduce optical damage.

sity. This enables an additional energy amplification by many orders of magnitude a before recompression.

Through the use of dispersive elements, CPA could be used to amplify short-pulse lasers with the use of high energy storage solid-state laser media ($F_{\text{sat}} \simeq \text{J/cm}^2$) [14]. A widespread solid state laser today is Ti:Sapphire, which provides an exceptionally broad emission spectrum to produce and amplify short-pulse lasers. Ti:Sapphire amplifiers are commonly used as the gain medium to achieve orders of magnitude amplification in the near-infrared region of the spectrum using regenerative [16] or multi-pass [17] amplification schemes. For large, multi-terrawatt or petawatt class laser systems amplification is chained through multiple stages with the beam diameter periodically increased to remain below material damage threshold.

1.1.2 Optical Parametric Amplification

Solid-state femtosecond laser technology is present in a myriad of applications in both industrial and research settings. However, the accessible wavelengths are limited by the available lasing materials with broad emission spectra capable of sustaining femtosecond pulse durations. In order to study wavelength-scaling of laser-plasma interactions, as well as to explore new wavelength regimes there is a necessity to produce tunable, ultrafast sources through various nonlinear optical processes including harmonic generation and four-wave mixing.

One such nonlinear process that can be employed to down-convert near-infrared light to the mid-infrared wavelength region using existing laser systems is known as optical parametric amplification (OPA). OPA is a parametric process that amplifies one signal beam through overlapping with a pump beam inside of a nonlinear medium. A typical non-linear crystal used in Ti:Sapphire pumped OPAs is beta-barium borate (BBO). As the two beams overlap inside the crystal proper phase-matching depletes the pump beam to amplify the signal beam and produce a third idler beam through difference frequency generation.

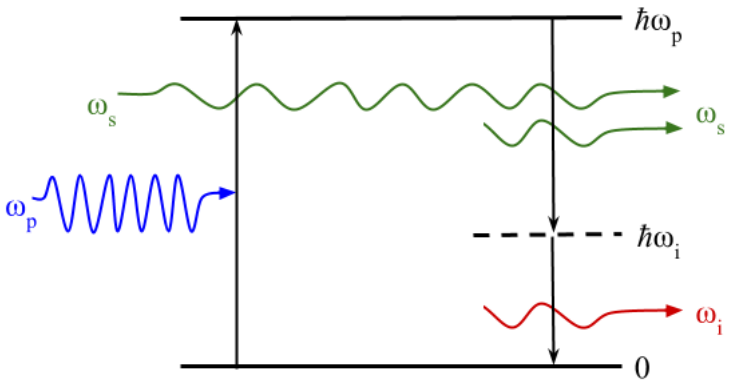

Figure 1.3: Energy level diagram of the OPA process. Pump and signal beam are incident on an energy level system. The pump excites the system to a higher energy level, $E = \hbar\omega_p$. The system the relaxes to the ground state through an intermediate virtual state, releasing a photon at the signal frequency and a photon at the idler frequency, ω_i.

The principle of OPA [18] uses a high frequency, high intensity beam (the *pump*, at frequency ω_p) to amplify a lower frequency, lower intensity beam (the *signal*, at frequency ω_s in a nonlinear medium; a third beam (the *idler*, at frequency ω_i, $\omega_i < \omega_s < \omega_p$) is generated in order to conserve energy,

$$\hbar\omega_p = \hbar\omega_s + \hbar\omega_i. \tag{1.1}$$

In order for the interaction to be efficient, momentum conservation (or phase matching) must also be satisfied,

$$\hbar\mathbf{k}_p = \hbar\mathbf{k}_s + \hbar\mathbf{k}_i, \tag{1.2}$$

where $\mathbf{k}_p, \mathbf{k}_s$, and $\mathbf{k}_i$ are the wave vectors of the pump, signal and idler, respectively. The amplified signal frequency can vary from $\omega_p/2$ to ω_p, and the corresponding idler varies from $\omega_p/2$ to 0; $\omega_p/2$ is known as the degeneracy condition. At degeneracy, signal and idler have the same frequency. The tunable nature of the OPA process enables studies that vary over a wide range of wavelengths. For instance, an OPA pumped by the Ti:Sapphire laser at UCI can produce laser-like radiation of considerable energy spanning 1.2-2.4μm.

1.2 Relativistic Laser-Plasma Interactions

Chirped pulse amplification has pushed laser technology to deliver light pulses with joules of energy over a few tens of femtoseconds (10^{-15}s) producing petawatt-class (10^{15}W) lasers. When focused to produce intensities on the order of tens of TW/cm^2 material breakdown in the focal region begins to occur leading to ionization and plasma formation. The laser is then capable of interacting directly with free charges within the plasma. Once intensities approach 10^{18}W/cm^2 , the electric fields are capable of driving the free electrons within the plasma to relativistic speeds after ionization. High-field (or high-intensity) science studies the dynamics of such relativistic interactions. When focused to near diffraction-limit spot sizes ($\sim 1\mu$m) these ultrafast lasers can exceed intensities of 10^{22} W/cm^2 [19] giving access to ultra-relativistic laser-plasma interactions. High-intensity laser-plasma interactions have been shown to produce relativistic electron bunches [15, 20], high energy ions [21, 22], and the higher-order harmonics of the laser [23, 24].

Initially, the study of relativistic laser-plasma interactions was restricted to single-shot or few hertz systems with central wavelengths in the near-infrared (NIR) spectral range. However, improvements in laser technology have enabled kilohertz laser systems with low energy, ultrashort pulse durations, and excellent mode quality to produce focal intensities necessary to studying relativistic laser-plasma interactions [25–28]. The increased repetition rate provides several benefits including increased statistics and signal-to-noise ratio, while operation in thermal steady-state conditions leads to improved shot-to-shot stability. The improved stability and increased shot rate enables the implementation of active feedback control systems for optimization [29, 30].

The scaling of laser-plasma interactions with the wavelength have been extensively studied. In laser-solid interactions, the driving wavelength can influence the laser-absorption and hot electron generation [31–34]. Relativistic electron generation and betatron radia-

tion through laser wakefield acceleration have also shown favorable scalings towards shorter wavelengths [35, 36]. The combination of nonlinear frequency conversion processes such as OPA producing tunable, ultrashort pulses with millijoule-level energies [37] at high repetition rates allows for further study of the influence of the driving wavelength on relativistic laser-plasma interaction.

1.2.1 Relativistic High Harmonic Generation

In the 1980s, experiments with long-pulse CO_2 lasers demonstrated harmonic spectra reflected from solid targets that extended into the optical [38]. It was then predicted that high harmonic generation should be achieved with ultra-short, ultra-intense lasers incident on solid-density plasmas [39]. Indeed, the 1990s saw the advent of high field laser systems able to produce on target intensities in excess of 10^{18} W/cm^2 . The subsequent discovery of relativistic HHG using solid density targets [23, 39–41] provided a mechanism of producing coherent, short wavelength light sources with minimum pulse durations on the order of tens of attoseconds. In fact, an advantage of relativistic harmonic generation is that the efficiency of the interaction scales favorably to ultra-relativistic intensities; an experimental campaign on the Vulcan Petawatt produced hundreds of harmonics extending to photon wavelengths of a few nanometers [24]. Laser-solid harmonic generation is also one of many laser-driven candidates for the generation of an isolated attosecond source [27, 42–44].

1.2.2 X-ray Emission Spectroscopy

Near-solid density plasmas with temperatures exceeding 1 keV can be produced by short-pulse lasers with intensities greater than 10^{19} W/cm^2 . The charge separation that can occur from laser-plasma interactions results in acceleration gradients approaching hundreds of GeV/m. Elucidating the properties of this HED matter including opacity and equations of

state is essential to understanding the physics of stellar interiors [45–47] and the development of inertial confinement fusion [48–50]. Developing an accurate description of these HED states remains an experimental and theoretical challenge due to the hot electron generation and transport, small spatial gradients, and strong self-generated magnetic and electric fields occurring in the highly-transient plasma conditions [51, 52].

The intensity, energy, and location of atomic emission lines give useful information about the constituent atoms in a plasma, as well as information about their local environments. X-ray emission spectroscopy has been used extensively as a diagnostic of electron density, temperature, and hot electron dynamics in laser-produced plasmas [53–61]. However, there have been few studies of high-resolution spectroscopy of matter formed via ultra-relativistic, laser-solid interactions [62–64]. In thin targets, energetic electrons can be rapidly accelerated through refluxing [65], and can ionize inner-shell electrons directly or create inner-shell vacancies *via* Bremsstrahlung radiation. However, for ultrashort lasers with high temporal contrast, the plasma pre-expansion is minimized enabling the target to maintain near-solid density and restricting electron heating to a few microns near the interaction surface [63].

1.3 Applications

Capturing ultrafast dynamics of atomic systems has become a significant thrust of the scientific community in order to gain an understanding of processes in the fields of chemistry [66], material science [67, 68], condensed-matter physics [69, 70], and biology [35]. Furthermore, materials can have remarkably different absorption features in the extreme ultraviolet (EUV) - wavelengths between 10-100nm - or soft x-ray - wavelengths between 1-10nm, which enables the discrimination of the chemical makeup of a sample with high resolution. For instance, the so-called "water-window" between 2.3nm and 4.4nm is a spectral region where the difference in absorption between water and carbon enables high contrast imaging of biological

samples [41]. If the light is circularly-polarized, it may be used to probe the electronic and magnetic properties of materials through techniques such as molecular chirality [71] and magnetic circular dichroism [72].

The complexity of these measurements is two-fold. If we wish to optically resolve features at a certain scale the Rayleigh criterion requires that the probe must be at a wavelength on the same scale or shorter. For probing molecular and crystalline systems, which contain structure on the few nanometer scale, x-rays are the necessary choice. Similarly, if we wish to observe time-resolved dynamics of a system, we need a temporal probe that is shorter than the dynamics in question. The motion of electrons around their parent nuclei occurs on ultrafast timescales: from attoseconds (10^{-18}) to femtoseconds (10^{-15}). Such timescales are too short to be measured electronically, therefore time-resolved rely on the generation of ultrashort light pulses.

One of the most promising applications of relativistic harmonic generation lies in the generation of attosecond, x-ray pulses. The scientific community has for decades been able to probe nanometer-scale systems on femtosecond timescales using well-developed radio-frequency (RF) technology. Fourth generation light sources, known as x-ray free electron lasers (XFEL) are capable of generating femtosecond, hard x-ray radiation through a combination of RF acceleration and undulator magnets for high flux, high energy photon sources for scientific research. These facilities include the Linear Coherent Light Source (LCLS) at Stanford Linear Accelerator Center (SLAC) [73]. LCLS also hosts the Matter in Extreme Conditions instrument, which combines the capabilities of the LCLS beam with a high power optical laser to study HED physics. However, the number of available XFEL facilities - there are only a few worldwide - is small compared to their high demand. This is in no small part due to their immense size and the extreme cost required to build and maintain. Conversely, EUV harmonic sources enable the generation of coherent short-wavelength light producing bright, compact, sub-fs pulse durations on the table top. The short pulse durations of such

EUV sources enable the study of attosecond science [74–77] while achieving spatial resolutions required for nanometer-scale imaging [78].

1.4 Thesis Organization

This thesis presents results from experimental and computational studies on relativistic laser-solid interactions driven at wavelengths ranging from 400 - 2100 nm. Harmonics of relativistically-intense infrared light sources (1.3μm and 2.1μm) were experimentally observed using solid density targets. The harmonic dependence on the driving laser polarization was characterized by polarization measurements of the output harmonics. The introduction of a second beam provides additional control over the relativistic harmonics, which are governed by the electron critical surface during the interaction. Finally, x-ray spectroscopy of copper foils irradiated at intensities $> 10^{21}\mathrm{W/cm^2}$ indicate that thin, < 5 μm thick targets may be uniformly heated to temperatures exceeding 3 keV while remaining near solid density.

Chapter 2 presents an overview of relevant physics applicable to the presented research. Chapter 3 discusses the experimental setups and diagnostics fielded in the experimental studies. A brief discussion of particle-in-cell (PIC) simulations is also included. Chapter 4 presents the results of midinfrared high harmonic generation studied at the high repetition rate lasers facilities at the University of California, Irvine and the Gérard Mourou Center for Ultrafast Optical Science at the University of Michigan. Chapter 5 examines the control of relativistic high harmonic generation driven by two-color fields. Chapter 6 summarizes the preliminary experimental results performed at the ALEPH laser facility at Colorado State University studying the K-shell x-ray emission from copper targets. Finally, Chapter 7 contains concluding remarks and future work.

Chapter 2

Background

In this thesis, the interaction of relativistically-intense lasers with overdense plasma is studied through experimental and computational methods. The experimental studies used ultrafast, Ti:Sapphire-based lasers to drive nonlinear frequency conversion processes in order to produce the highly nonlinear conditions of relativistic laser-matter interactions. The following chapter will constitute a brief overview of the physics of high-intensity laser-plasma interactions necessary for understanding the work detailed in later chapters including the technology of pulsed lasers, single electron dynamics in a relativistic field, and short-pulse, laser-solid interactions.

2.1 High Intensity Laser Physics

In order to produce high intensity laser-matter interactions, it is necessary to focus high power lasers to near diffraction limited focal spots - typically a few microns in diameter. Such short pulse lasers can be decomposed into a spectrum of frequencies associated with sinusoidal solutions of the wave equation. With the assumption that the solution can be

formed from separation of variables, a general solution of the wave equation is of the form

$$E(r,t) = u(\mathbf{r})T(t), \tag{2.1}$$

where $u(\mathbf{r})$ and $T(t)$ correspond to the spatial and temporal profiles respectively. The plane-wave, monochromatic solution to this takes the form of

$$E(r,t) = E_0 e^{i(\mathbf{k_0}\cdot\mathbf{r}-\omega_0 t)}, \tag{2.2}$$

where E_0 is the maximum field amplitude, $|\mathbf{k_0}| = 2\pi/\lambda_0$ is the wavenumber for wavelength λ_0, and $\omega_0 = 2\pi f_0$ is the angular frequency. Written in this form, the electric field is a complex-valued function. Since the field amplitude ($\mathrm{Re}\{E\}$) or intensity (I) are the values measured in experiments it is useful to remember that $\mathrm{Re}\{E\} = E_0 \cos(\mathbf{k_0}\cdot\mathbf{z} - \omega_0 t)$ replaces the exponential with a cosine function due to Euler's equation and the intensity is the absolute square of the field amplitude $I = |\mathbf{E}|^2 = E_0^2$.

The plane wave is a special case for electromagnetic fields whose value is constant over any plane that is perpendicular to the direction of motion. In other words, the plane that produces a constant phase given by $\mathbf{k_0}\cdot\mathbf{r} - \omega_0 t$. These points of constant phase are known as the wavefront. In general, wavefronts do not have to take the form of a plane, for example the wavefront of a point source is described by a spherical wave. From a geometrical optics standpoint the plane wave is produced by rays parallel to one another, i.e. collimated light. While the plane-wave solution is a good starting point for understanding laser-matter interaction, all lasers have some spectral bandwidth and spatial extent, and therefore do not obey the plane wave solution.

A further complication arises when discussing electromagnetic waves propagating through material that can be described by an index of refraction n. The one-dimensional electromag-

netic wave equation in matter can be written in the form:

$$\frac{\partial^2 \mathbf{E}}{\partial t^2} = \frac{c^2}{n^2}\frac{\partial^2 \mathbf{E}}{\partial z^2}. \tag{2.3}$$

For material with indices of refraction that are isotropic, then the free-space wavenumber is modified by $k = nk_0$. If instead the index varies as a function of position, $n(z)$, the resulting differential equation doesn't necessarily produce sinusoidal oscillations. This is especially true for variations that occur over length scales on the order of the free-space wavelength. However, if the variations are assumed to be "slowly-varying," or $(dn/dz)/k_0 n^2 \ll 1$, then plane-wave solutions are good approximations of the electromagnetic wave propagation.

2.1.1 Gaussian Optics

Returning to Equation 2.1, the spatial component of the wave equation can be shown to equal the solution of the Helmholtz equation:

$$\nabla^2 u(\mathbf{r}) + k_0^2 u(\mathbf{r}) = 0. \tag{2.4}$$

The Helmholtz equation can be further simplified by assuming that field envelope, $u(\mathbf{r})$, is varying slowly in space compared to the wavelength,

$$|\nabla^2 u| \ll |\mathbf{k_0} \cdot \nabla u|. \tag{2.5}$$

This is known as the slowly-varying envelope approximation, or the paraxial approximation. The paraxial approximation is valid when considering optical systems in which rays make only small angles with the optical axis. By redefining the system such that the wave propagates along z, and spatially varies in the transverse plane, $r = \sqrt{x^2 + y^2}$, a solution to the

Helmholtz equation is given by

$$u(r,z) = A(r)e^{ik_0 z} \tag{2.6}$$

One solution to the paraxial Helmholtz equation of the form given by Equation 2.6 is known as the Gaussian beam. Assuming that the electric field is polarized along x and propagating in z, the spatial component of a focusing Gaussian beam is given by:

$$u(r,z) = E_0 \frac{w_0}{w(z)} e^{-r^2/w^2(z)} e^{ikz} e^{-ikr^2/2R(z)} e^{i\varphi(z)}, \tag{2.7}$$

where w_0[1] and $w(z)$ are the beam waist at focus and at a distance z from focus, $R(z)$ is the radius of curvature of the wavefront, and $\varphi(z)$ is the Guoy phase. However, it should be noted that there are an infinite number of solutions to the paraxial wave equation. A complete basis set that can be used to describe free space electromagnetic waves are the TEM, or Gaussian, modes of which the Gaussian beam is described above is known as the fundamental Gaussian. The transverse intensity profile of a focusing TEM_{00} Gaussian beam is given by

$$I(r,z) = I_0 (\frac{w_0}{w(z)})^2 e^{-\frac{2r^2}{w(z)^2}}. \tag{2.8}$$

The beam waist is the radius at which the intensity has decreased to $1/e^2$ of its peak value, and if given by:

$$w(z) = w_0 \sqrt{1 + (\frac{z}{z_R})^2}, \tag{2.9}$$

where z_R is the Rayleigh length and is determined by the beam's smallest beam size and

[1]By convention, the variables for beam waist w_0 and angular frequency ω_0 are visually very similar. However, they are distinct parameters.

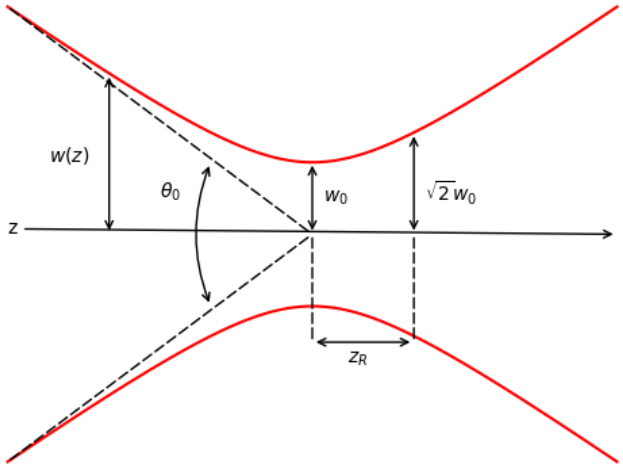

Figure 2.1: The evolution of the beam diameter of a Gaussian laser as a function of distance from the focal plane defined at $z = 0$.

wavelength,

$$z_R = \frac{\pi w_0^2}{\lambda_0}. \tag{2.10}$$

At a distance z_R from the focus, the width of the beam is $\sqrt{2}$ larger than it is at the focus $w(z_R) = \sqrt{2}w_0$. The Rayleigh length is the distance $z = \pm z_R$ from the focal plane where the peak (on-axis) intensity of the Gaussian has dropped by half of the maximum. In the context of high intensity experiments, it is common to say that the beam is "in focus" over the confocal parameter, defined to be twice the Rayleigh length. The peak (on-axis or $r = 0$) intensity of a Gaussian with pulse duration τ_p and E_p energy is given by

$$I_{\text{peak}} = \frac{2P}{\pi w(z)^2} \tag{2.11}$$

where P is the peak laser power.

Laser systems that use optical cavities to enforce specific beam modes, such as oscillators and

regenerative amplifiers, typically have output beam profiles that can be described through the paraxial approximation. The output intensity profile of a laser can therefore be described by the family of allowed TEM modes which form an orthogonal basis set. Two such sets are the Laguerre-Gaussian modes, which describe lasers with cylindrical symmetry, and the Hermite-Gaussian modes, which describe lasers with rectangular symmetry.

2.1.2 Focal Spot Profiles

When a monochromatic plane wave passes through an aperture, the far field profile, from Frauenhofer diffraction theory, will simply be the Fourier transform of the input aperture. Similarly, for a plane wave being focused by an optic such as a lens, we can model the focus as equivalent to the far field diffraction pattern of an aperture of the optic. Because lasers and focusing optics are finite in extent we can consider the focusing optic or beam diameter (whichever is smaller!) as the optical stop. For a beam much larger than the stop, in one dimension we can approximate it as a plane wave incident on a single slit. The single slit diffraction experiment has the well-known solution of a Sinc function. Similarly, a plane wave incident on a circular aperture (i.e. a finite beam and a finite lens) produces an Airy disk. The focal spot produced by different beam profiles can be described as the convolution of the input profile and the circular aperture. One caveat is that in reality lasers are not plane waves and thus not perfectly collimated. This means the focal spot profile is not exactly the Fourier transform of the input function. A quirk of nature is how similar the Gaussian profile is to the Airy pattern (see Fig. 2.2), so a focused Gaussian beam will have defined properties similar to those found in collimated Gaussian beams, e.g. peak intensity and beam waist.

The beam waist of a Gaussian is similar to the radial location of the first zero of the Airy disk. Therefore, it is useful to define them such that

$$2w_0 \approx 1.22\lambda_0 f/\#, \tag{2.12}$$

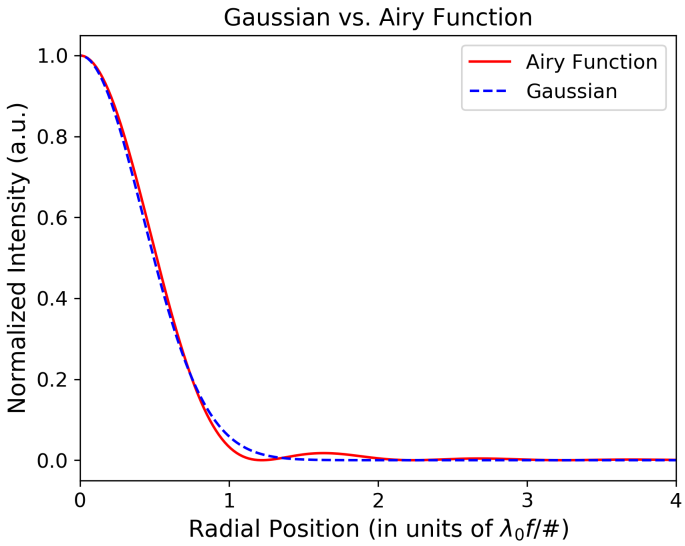

Figure 2.2: Radial profiles of Airy function and Gaussian. The Gaussian standard deviation has been chosen such that $\sigma = 0.42\lambda_0 f/\#$ the value at which the peak intensity of the Gaussian and Airy disk match.

where $f/\#$ is the f-number, or ratio of the beam diameter divided by the focal length of a lens. In other words, diffraction limited optics produce a focal diameter on the order of the f-number divided by the wavelength. For a Ti:Sapphire system with central wavelength $\lambda_0 = 0.8$ μm , focusing with an $f/1$ optic should produce a spot with an approximate diameter of 1 μm while an $f/2$ will have a 2 μm focus. In practice, these numbers will always be larger due to wavefront imperfections leading to deviations from diffraction limited focusing.

High intensity experiments are enabled through the use of low $f/\#$ optics producing small focal diameters. Practically achieving such small focal diameters can be challenging. Tightly-focused light, i.e. to focal sizes approaching the wavelength of light ($w_0 \sim \lambda_0$), require a near-perfect wavefront. Spherical mirrors and lenses introduce additional wavefront distortions due to spherical aberrations; parallel rays reflecting from near the edge of the optic do not focus to a single point. For monochromatic light, specifically designed aspheric lenses can be used as an effective means of producing high quality focal spots. However, short-pulse lasers have spectra with broad bandwidths, which leads to a spatial smearing of the focal

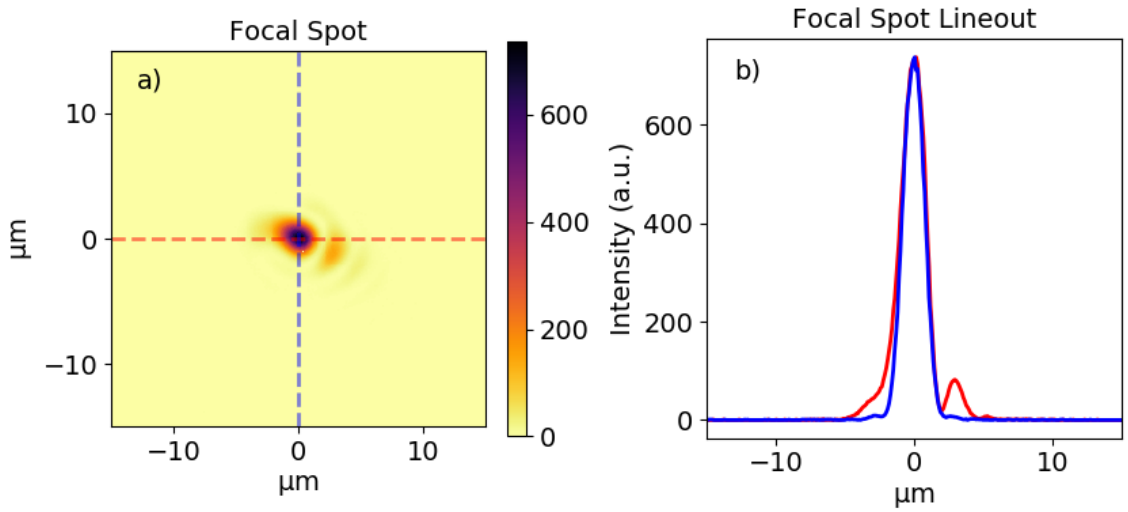

Figure 2.3: Measured focus of Solstice Ace output produced with an f/2 gold-coated off axis parabolic mirror. a) Combining multiple images taken with a filter stack increased effective bit depth of 8-bit camera. b) Lineouts of peak fluence in horizontal (red) and vertical (blue) directions.

spot due to chromatic aberrations where each color will focus to a different position along the propagation axis. Therefore, metallic-coated parabolic mirrors are required in order to produce near diffraction-limited focal spots for ultrafast lasers.

There exists a trade-off between tight foci and practical utilization. Focal length smaller than $f/1$ require target positioning that would obstruct portions of the incident beam. This can be an issue for laser-gas interactions, but solid targets will significantly obstruct the beam causing diffraction and worsening of the focal spot. Another challenge in tight focusing geometries arises from target alignment. In order to study high intensity laser-matter experiments, solid targets must be placed at the focus to maximize intensity. A target is said to be "in focus" if it is within one Rayleigh length of the focal plane. It is possible to re-write the Rayleigh length in terms of the $f/\#$,

$$z_R = \frac{\pi w_0^2}{\lambda_0} = 4.67 \lambda_0 f/\#^2. \tag{2.13}$$

Due to the quadratic dependence on the focal diameter, or the f-number, the tolerances for positioning a target becomes significantly harsher for sharp focusing optics. An $f/1$ optic

focusing 800nm light will have a Rayleigh length of $\sim 4\mu$m, while an $f/2$ optic will have a Rayleigh length of $\sim 16\mu m$, already making positioning much easier.

In many simulations and theoretical studies of high intensity laser-plasma interactions, the incident laser field is assumed to be nearly planar. This simplifies the interaction, and is approximately valid in experiments given loose focusing geometries ($w_0 \gg \lambda_0$). However, for a tightly focusing beam ($\sim f/1$) the plane wave approximation is no longer valid. The transverse spatial gradients of a Gaussian focus can play a significant role in the interaction. Simulation results have shown that in extreme cases, the spatial gradients lead to the production of isolated attosecond pulses emitted in completely different directions compared to the driving pulse [27].

2.1.3 Temporal Phase

The temporal profile and spectral content of a laser pulse are related through the Fourier transform. As such a laser pulse follows a time-bandwidth relationship defined by the uncertainty relation

$$\tau \Delta\omega = 2\pi c_B, \tag{2.14}$$

where τ is the Fourier-transform-limited (FTL) pulse duration, $\Delta\omega$ is the laser bandwidth centered about frequency ω_0, and c_B is a constant related to the temporal envelope of the pulse. For a Gaussian pulse, $c_B \approx 0.44$. Then for a 30 fs Gaussian pulse, the required frequency bandwidth is 14.7 THz.

The temporal profile of a Gaussian electric field is given by:

$$E(t) = E_0 \exp[-2\ln 2(t/\tau)^2] \exp[-i(\omega_0 t + \phi(t))] + c.c., \tag{2.15}$$

where E_0 is the peak electric field strength, and $\phi(t)$ is the temporal phase. An FTL pulse is defined such that the temporal phase $\phi(t) = 0$. However, achieving this is non-trivial, as the large bandwidth of an ultrafast pulse can quickly cause phase mismatch. When a pulse travels through any material that is not vacuum, the propagation of the spectral components of the pulse are determined by $n(\omega)$, the material index of refraction. Even small variation in index can quickly lead to differences in phase velocity large enough to lower the peak peak of a laser pulse.

It is more common to discuss the impact of phase in the frequency domain. The electric field in the frequency domain is given by:

$$E(t) = \tilde{E}_0 \exp[-4 \ln 2((\omega - \omega_0)/\Delta\omega)^2] \exp[-i\phi(\omega - \omega_0)], \tag{2.16}$$

where $\phi(\omega - \omega_0)$ is the spectral phase. In general, $\phi(\omega)$ can be an arbitrary function but typically the phase is approximated by a Taylor expansion. The full Taylor expansion is given by:

$$\phi(\omega) = \sum_{n=0}^{\infty} \frac{\partial^n \phi(\omega)}{\partial \omega^n}\bigg|_{\omega=\omega_0} \frac{(\omega - \omega_0)^n}{n!} = \sum_{n=0}^{\infty} \phi^{(n)}(\omega = \omega_0) \frac{(\omega - \omega_0)^n}{n!} \tag{2.17}$$

The individual terms of the Taylor expansion are typically discussed in terms of the prefactor $\phi^{(n)}(\omega = \omega_0)$ terms. The constant term is known as the carrier-envelope phase (CEP), which determines the location of the field maximum in relation to the envelope function. The linear term, group delay, determines the relative delay of the entire pulse, and in most situations can be ignored. The dominant term for the shape temporal envelope is the quadratic term, group delay dispersion (GDD).

We can determine how the material index of refraction impacts the spectral phase. If we assume that the index of refraction is slowly varying across the spectral bandwidth, we may make a Taylor expansion of the $n(\omega)$ about the central frequency ω_0. The first three terms

of the expansion are:

$$v_\phi = \frac{c}{n} \tag{2.18}$$

$$v_g = (\frac{\omega}{c}\frac{dn}{d\omega} + \frac{n}{c})^{-1} \tag{2.19}$$

$$\text{GVD} = \frac{dv_g}{d\omega} = -v_g^2(\frac{\omega}{c}\frac{d^2n}{d\omega^2} + \frac{2}{c}\frac{dn}{d\omega})^{-1}, \tag{2.20}$$

where v_ϕ is the phase velocity, v_g is the group velocity and GVD is the group velocity dispersion or material dispersion. For a material of thickness z, the carrier envelope phase is related to the phase velocity by $\phi^0(\omega = \omega_0) = z/v_\phi$. The group delay is $\phi^1(\omega = \omega_0) = z/v_g$. Finally, the group delay dispersion is given by GDD = zGVD. In order for the pulse to remain near the FTL it is important to keep propagation through material to a minimum, thereby reducing material dispersion.

Practically, the introduction of GDD can be understood through a simple example. A Fourier-transform-limited pulse in vacuum is a superposition of many frequencies perfectly in-phase with each other. For this case, the phase velocities of the individual components are equal, and the instantaneous frequency given by $\omega(t) = \frac{d\phi}{dt} = 0$. As the pulse propagates through material, the accumulated GDD from material dispersion leads to a relative phase shift between the individual frequency components. Thus certain frequencies begin to "outrun" others, producing a nonzero instantaneous frequency and a broadening of the pulse envelope. If the dispersion is purely through GDD, then the change in frequency is linear, and is known as linear chirp. Positive chirp, where red components outrun blue components, is most common for NIR pulses transmitting through dielectric materials.

2.1.4 Self Phase Modulation

Dispersion is a linear effect that plays a significant role in the temporal shape of the laser pulse. There are also nonlinear effects that impact short-pulse laser interaction. Linear optics requires that the material responds proportionally to the electric field strength, but for very intense fields this assumption is no longer valid. When a very intense pulse propagates through a medium, the material index changes in response to the applied field proportional to the applied field known as the Kerr effect. The nonlinear index of refraction is given by:

$$n \approx n_0 + n_2 I(t) = n_0 + \frac{\chi^3_{eff}}{4n_0^2\epsilon_0 c} I(t), \tag{2.21}$$

where n_2 is the nonlinear Kerr index. For common dielectric materials, n_2 is on the order of $10^{-18} - 10^{-16}$ cm^2/W.

The index of refraction now contains a dependence on the intensity profile of the laser pulse. Self-phase modulation (SPM) is a non-linear change in phase of the pulse due to the non-linear refractive index. By making the assumption that the material response is instantaneous, and the material length, z, is short enough to ignore dispersion, SPM has an analytical solution that results in a phase change given by:

$$\phi(t) = \omega_0 t - \frac{\omega_0}{c}(n_0 + n_2 I(t))z, \tag{2.22}$$

where $\phi_{\mathrm{NL}} = -\frac{\omega_0}{c} n_2 I(t) z$ is the non-linear phase associated with SPM.

The analytical solution to SPM results in a temporal duration of the laser remains constant. Therefore, the non-linear phase due to SPM results in a change in FTL of the laser pulse. Depending on the initial phase of the laser and the sign of n_2 this can lead to the generation or removal of new frequencies termed spectral broadening and narrowing, respectively. When coupled with material dispersion or dispersion compensation optics such as chirped mirrors

this can lead to an increase or decrease in the pulse duration.

2.1.5 Laser Contrast

High intensity lasers used in laser-solid interactions consist of a main femtosecond pulse but also can contain significant structure in the laser pre-pulse. The pre (and post)-pulsing effects occur due to a myriad of effects including misaligned Pockels cells used in the amplification process, or amplified spontaneous emission (ASE). One metric of the laser pre-pulse can be through an intensity contrast - the ratio of the pulse peak intensity to the pulse intensity at some other time. A laser with an intensity contrast of 10^{-6} at one nanosecond has one-millionth the intensity of the main pulse one nanosecond prior to the peak of the pulse. While this might seem insignificant, if the main laser is focused to $I_0 > 10^{18}$ W/cm^2 then the pre-pulse at one nanosecond will exceed the damage threshold of most materials ($I \approx 10^{12}$ W/cm^2). This can cause material ionization and plasma formation before the arrival of the main pulse.

One of the highest gain methods found in CPA-based lasers is regenerative amplification [16]. Regenerative amplifiers inject a seed pulse into an optical cavity which will then undergo several round trip passes before ejection. Because this method leads to significant ASE buildup, lasers systems with a regenerative amplification scheme of CPA can exhibit significantly lower contrast ratios than those amplified through a multi-pass design. Methods of improving laser contrast include cross-polarized wave generation (XPW) [79], and plasma mirrors [80].

One benefit gained in moving to non-linear frequency conversion processes such as second harmonic generation (SHG) or OPA to drive laser-plasma interactions is the boost in contrast ratio. The SHG process scales as $|E|^2 = I$, and requires a sufficiently high-intensity during propagation through the non-linear crystal for high conversion efficiency. The second har-

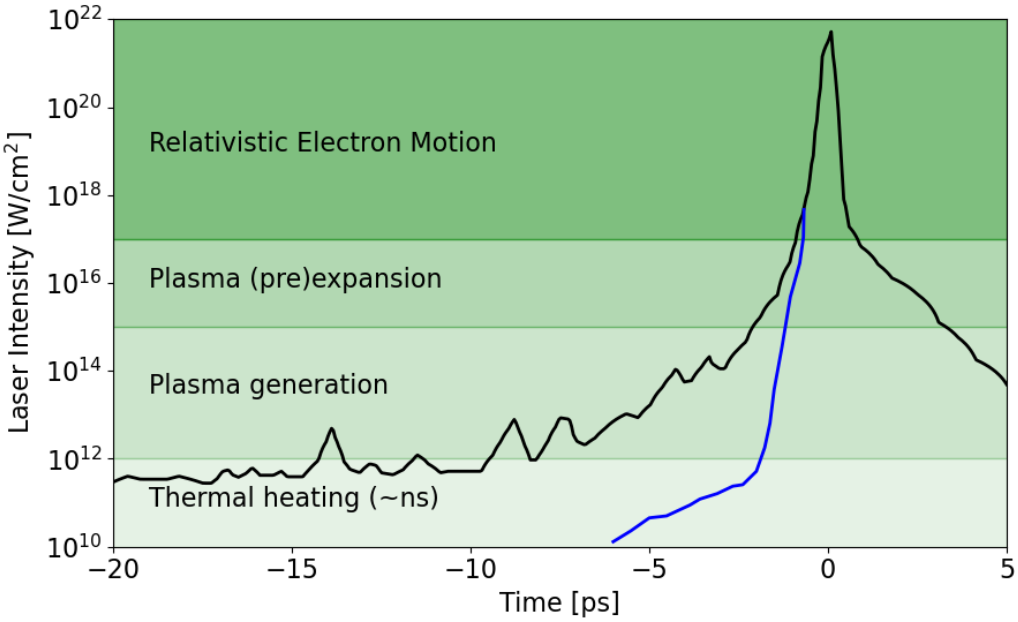

Figure 2.4: Cartoon of two potential picosecond contrasts of high intensity laser. Adapted from [2].

monic of Ti:Sapphire lasers such as the ALEPH laser at Colorado State University [3] have been shown to produce very high contrast beams (10^{-12} picosecond intensity contrast). The OPA process occurs only when the pump and seed beams are overlapped spatio-temporally inside the nonlinear crystal. Therefore, OPA processes produce significantly higher contrast ratios as there exists less amplification away from the main pulse. Such beams enable studies of sharp density gradient plasmas without the necessity of high loss, pulse cleaning instruments. Of course, a higher contrast pump laser will lead to higher contrast in the OPA beams, so there exists a trade-off between the two.

2.2 Single Electron Dynamics

When a short-pulse, high-intensity laser is incident on any form of matter, the target may begin to ionize when the pulse intensity approaches TW/cm^2. Free electrons interacting with such high electric fields undergo highly non-linear motion while simultaneously accelerating

to near the speed of light. As the electron motion occurs on the femtosecond timescale, the heavier ions remain a fixed background. To gain an understanding of the complex dynamics, we can start with the toy model of a single electron in a laser field. The underlying concepts can then be extended to more-complicated physical systems. For example, a plasma exhibits collective motion that is non-existent in the single electron case.

2.2.1 Relativistic Electron Motion

All charged particles experience a force from an electric field, and an additional force if moving transverse to a magnetic field. The relativistic equations of motion are described by the Lorentz force and an associated energy equation

$$\frac{d\mathbf{p}}{dt} = q(\mathbf{E} + \mathbf{v} \times \mathbf{B}) \tag{2.23}$$

$$\frac{d\gamma mc^2}{dt} = q\mathbf{v} \cdot \mathbf{E}, \tag{2.24}$$

where $\mathbf{E}$ and $\mathbf{B}$ are the total electric and magnetic fields, q and m are the particle's charge and mass, $\gamma = 1/\sqrt{1 - v^2/c^2} = \sqrt{1 + p^2/m^2c^2}$ is the Lorentz factor, and $\mathbf{p} = \gamma m\mathbf{v}$ is the relativistic momentum. Maxwell's equations determine the electric and magnetic fields a charged particle experiences, which in turn undergoes motion determined by the Lorentz force. Maxwell's equations can be reformulated to be expressed through the scalar (Φ) and vector ($\mathbf{A}$) potentials with the electric and magnetic fields of the laser defined by:

$$\mathbf{E} = -\nabla\Phi - \frac{1}{c}\frac{\partial \mathbf{A}}{\partial t} \tag{2.25}$$

$$\mathbf{B} = \nabla \times \mathbf{A} \tag{2.26}$$

The total electron momentum gained over a laser cycle which has strength A_0 is given by eA_0. We can then normalize the momentum gain to the electron rest momentum through

the normalized vector potential a_0,

$$a_0 = \frac{eA_0}{m_e c} = \frac{eE_0}{m_e c \omega_0}, \tag{2.27}$$

where ω_0, E_0, e, m_e, and c are the laser frequency and peak electric field, the electron charge and mass, and the speed of light, respectively.

We can consider a free electron moving in a laser field, written as a sinusoidal oscillation component inside an envelope function, $\mathbf{E}_0(\mathbf{r})$ propagating along the $\hat{z}$-direction with frequency ω_0 and wavenumber $k_0 = \omega_0/c$

$$\mathbf{E}(\mathbf{r}, t) = \mathbf{E}_0(\mathbf{r}) e^{i(k_0 z - \omega_0 t)} \hat{x} \tag{2.28}$$

$$\mathbf{B}(\mathbf{r}, t) = \mathbf{B}_0(\mathbf{r}) e^{i(k_0 z - \omega_0 t)} \hat{y}, \tag{2.29}$$

where $\mathbf{B}_0(\mathbf{r}) = \mathbf{E}_0(\mathbf{r})/c$.

An electron initially at rest will start to move along the laser polarization direction due to the electric force. Once the electron begins to oscillate, the velocity induced by the electric field then causes a force along the laser axis - in the $\hat{z}$-direction - from the $\mathbf{v} \times \mathbf{B}$ component of the Lorentz force. Provided the wave amplitude is not sufficiently large to drive the electron to relativistic velocities, the magnetic force component is much weaker than the electric force component in the Lorentz force. Taking the first order approximation of Equation 2.23

$$\frac{d\gamma m_e \mathbf{v}}{dt} = -|e|[\mathbf{E} + \mathbf{v} \times \mathbf{B}] \approx -|e|\mathbf{E}, \tag{2.30}$$

then integrating once with respect to time yields the electron velocity amplitude

$$v_{\text{osc}} = \frac{eE_0}{\gamma m_e \omega_0} \tag{2.31}$$

known as the quiver velocity. The normalized vector potential is therefore defined as $a_0 = eE_0/m_e c\omega_0 = \gamma m_e v_{\rm osc}/m_e c$, or $a_0 = \gamma\beta$, where $\beta = v_{\rm osc}/c$. For $a_0 = 1$ an electron's quiver velocity is given by $\beta = c/\sqrt{2}$ The conversion between normalized and practical units is found through

$$a_0 = 0.85 \times 10^{-9}\sqrt{I_0[\mathrm{W/cm^2}]\lambda_0[\mu\mathrm{m}]^2}. \tag{2.32}$$

The normalized vector potential quantifies the strength of the interaction between a high intensity laser and a free electron. For laser field strengths $a_0 \geq 1$, the momentum imparted to the electron becomes strongly relativistic ($\gamma m_e v_{\rm osc} \geq m_e c$), and the quiver velocity is approximately equal to c. The magnitude of $\mathbf{v} \times \mathbf{B}$ is now comparable to the electric field strength, and can no longer be ignored. Note, that the normalized vector potential depends not only on the intensity, but also on the wavelength of light. This enables relativistic experiments to be conducted with longer wavelength drivers, e.g. ultrafast pulses from an OPA process, that produce nominally lower intensity interactions.

2.2.2 Free Electron in a Relativistically Intense Laser Field

The motion of a free electron in a plane-wave laser field has an exact solution, but typically there are no closed form solutions for relativistic laser-plasma interactions. For the single laser case, we will follow the derivation by P. Gibbon in his book. [81]. First, we will define our electromagnetic field propagating in the $\hat{z}$-direction in terms of the vector potential:

$$\mathbf{A}_{\rm wave} = \delta a_0 \cos\xi\ \hat{x} + (1-\delta^2)^{1/2} a_0 \sin\xi\ \hat{y}, \tag{2.33}$$

where $\xi = \omega t - kz$ is the phase of the wave, a_0 is the normalized vector potential, and δ is a polarization parameter. The polarization parameter is defined such that $\delta = \pm 1, 0$

for a linearly polarized wave and $\pm 1/\sqrt{2}$ for a circularly polarized wave. The electric and magnetic fields are defined as the time derivative and curl of the vector potential from Eqs 2.25 and 2.26

$$\mathbf{E}_{wave} = -\frac{\partial \mathbf{A}}{\partial t} = \delta a_0 \sin\xi \ \hat{x} - (1-\delta^2)^{1/2} a_0 \cos\xi \ \hat{y} \tag{2.34}$$

$$\mathbf{B}_{wave} = \nabla \times \mathbf{A} = (-\frac{\partial A_y}{\partial z}, \frac{\partial A_x}{\partial z}, 0) = \delta a_0 \sin\xi \ \hat{y} + (1-\delta^2)^{1/2} a_0 \cos\xi \ \hat{x} \tag{2.35}$$

Using the expressions for the total fields, we write Equation 2.23 in terms of the vector potential. The perpendicular components becomes:

$$\frac{d\mathbf{p}_\perp}{dt} = \frac{\partial \mathbf{A}}{\partial t} + v_z \frac{\partial \mathbf{A}}{\partial z} = \frac{d\mathbf{A}}{dt}. \tag{2.36}$$

We can therefore integrate Eq 2.36 with respect to time

$$\mathbf{p}_\perp = \mathbf{A} + \mathbf{p}_{\perp,0}, \tag{2.37}$$

where $\mathbf{p}_{\perp,0}$ is the initial perpendicular motion of the electron. We are interested in an electron initially at rest, therefore we choose $\mathbf{p}_{\perp,0} = 0$. In this case, the longitudinal momentum is identically the vector potential of the laser field. Next, we are interested in the longitudinal motion.

The longitudinal component of Equation 2.23 is

$$\frac{dp_z}{dt} = v_y B_x - v_x B_y = -v_x \frac{\partial A_x}{\partial z} - v_y \frac{\partial A_y}{\partial z}. \tag{2.38}$$

We can also express the energy relation (Equation 2.24) in terms of the vector potential:

$$\frac{d\gamma}{dt} = v_x \frac{\partial A_x}{\partial t} + v_y \frac{\partial A_y}{\partial t}. \tag{2.39}$$

Subtracting Equations 2.38 and 2.39 gives

$$\frac{dp_z}{dt} - \frac{d\gamma}{dt} = -v_x(\frac{\partial A_x}{\partial t} + \frac{\partial A_x}{\partial z}) - v_y(\frac{\partial A_y}{\partial t} + \frac{\partial A_y}{\partial z}). \tag{2.40}$$

Because the electromagnetic wave is a function of $\xi = t - z$, the right hand terms vanish identically. We can then integrate the left hand side of Equation 2.40 to get $p_z - \gamma = \alpha$, where α is another constant of motion. We can rearrange the relationship between the gamma factor and momentum, $\gamma^2 = 1 + \mathbf{p} \cdot \mathbf{p} = 1 + \mathbf{p}_\perp^2 + p_z^2$, which we can use to eliminate γ:

$$p_z = \frac{1 - \alpha^2 + \mathbf{p}_\perp^2}{2\alpha} \tag{2.41}$$

For an electron initially at rest, $p_x = p_y = p_z = 0$, we can solve Eq 2.41 to find that $\alpha = 1$. Equations 2.37 and 2.41 constitute the general equations of motion of a free electron in a laser field. The exact orbits can be solved by integrating both equations and specifying α. Finally, these equations are motion are not restricted to a single electromagnetic field. While we initially assumed a single field, the solution only requires the vector potential to be written as functions of $\xi = t - x$. Therefore, we can take this general solution and understand how the interaction changes for different incident waveforms.

2.2.3 Free Electron in Single Color Laser Field

Consider the case of a single laser field propagating in the $\hat{z}$ direction with arbitrary polarization. As a reminder, the vector potential of such a field is given by

$$\mathbf{A} = (\delta a_0 \cos\xi, (1 - \delta^2)^{1/2} a_0 \sin\xi, 0) \tag{2.42}$$

The electron is initially at rest before the EM wave arrives, so at $t = 0$, $p_{x,0} = p_{y,0} = p_{z,0} = 0$, $\gamma = 1$, and $\alpha = 1$. The transverse momenta equations are as follows:

$$p_x = \delta a_0 \cos\xi \tag{2.43}$$

$$p_y = (1-\delta^2)^{1/2} a_0 \sin\xi, \tag{2.44}$$

and the longitudinal momentum is given by

$$p_z = \frac{p_\perp^2}{2} = \delta^2 a_0^2 \cos^2\xi + (1-\delta^2) a_0^2 \sin^2\xi. \tag{2.45}$$

By using the trig identities $\sin^2\xi = 1 - \cos^2\xi$ and $\cos 2\xi = 2\cos^2\xi - 1$,

$$p_z = \frac{a_0^2}{4}[1 + (2\delta^2 - 1)\cos 2\xi] \tag{2.46}$$

We can integrate Equations 2.43,2.44, and 2.46 to obtain the electron orbits:

$$x = \delta a_0 \sin\xi \tag{2.47}$$

$$y = -(1-\delta^2)^{1/2} a_0 \cos\xi \tag{2.48}$$

$$z = \frac{a_0^2}{4}[\xi + \frac{2\delta^2 - 1}{2}\sin 2\xi]. \tag{2.49}$$

Linearly Polarized Field

We choose the laser polarization as linearly polarized in the $\hat{x}$ direction, which corresponds to $\delta = 1$. The electron orbit is then

$$x = a_0 \sin \xi \tag{2.50}$$

$$y = 0 \tag{2.51}$$

$$z = \frac{a_0^2}{4}[\xi + \frac{1}{2}\sin 2\xi]. \tag{2.52}$$

We can see that the electron orbit in the transverse direction has the same form as the non-relativistic case. This solution exhibits a similarity in $(x/a_0, z/a_0^2)$, i.e. the solutions looks identical when scaled by the normalized vector potential. As we can see in Figure 2.5a the electron begins to drift in the direction of laser propagation with a drift velocity of

$$v_D = \frac{a_0^2}{4 + a_0^2}. \tag{2.53}$$

The presence of this longitudinal drift velocity contrasts with non-relativistic dynamics, where the electron only oscillates in the transverse plane at the frequency of the laser.

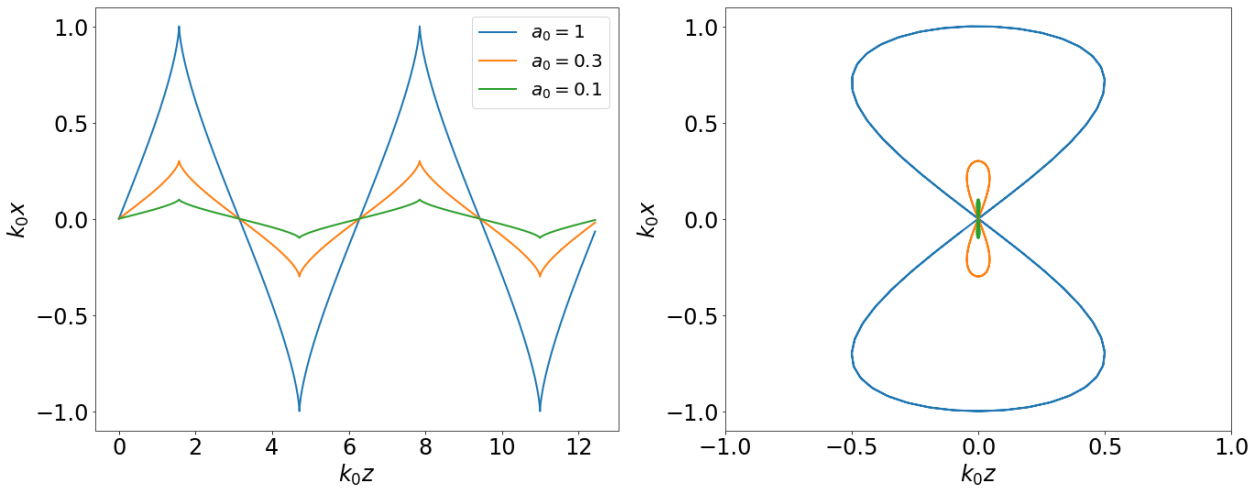

(a) Electron motion in lab frame

(b) Classic figure-8 motion in the drifting frame.

If we were to shift our coordinates to the average drift frame of the electron, we obtain the well-known figure-8 motion shown in Figure 2.5b. As we can see, the electron oscillates at twice the frequency in the longitudinal frame due to the $\mathbf{v} \times \mathbf{B}$ force. The difference in oscillation frequency from the two components of the Lorentz force is actually the mechanism behind the different allowed harmonics during overdense high harmonic generation, which will be discussed later.

Circularly Polarized Field

Next, we choose the laser polarization as left-hand circular , which corresponds to $\delta = 1/\sqrt{2}$. The electron orbit is then

$$x = \frac{a_0}{\sqrt{2}} \sin \xi \tag{2.54}$$

$$y = -\frac{a_0}{\sqrt{2}} \cos \xi \tag{2.55}$$

$$z = \frac{a_0^2}{4} \xi. \tag{2.56}$$

Once again we see the classical electron oscillation in the transverse direction; the electron orbit traces out a circular orbit. However, the longitudinal motion is significantly different from the linearly polarized case. The longitudinal drift term is still present, however the oscillatory term at twice the laser frequency vanishes identically.

The ponderomotive force is a force that acts upon charged particles due to spatial gradients of high frequency electric fields, for instance in the Gaussian intensity profile of optical light. It is possible to derive the ponderomotive force by neglecting relativistic effects using a simple model. Consider an electron initially at rest that resides in an electric field that linearly increasing in a single transverse direction, for example Equation 2.28 where E_0 is replaced by $E(x) = E_0 x$. After substituting this electric field into the Lorentz force, the equation

becomes nearly intractable even after neglecting the magnetic field term:

$$m_e\ddot{x} = qE_0 x \cos(k_0 z - \omega_0 t). \tag{2.57}$$

To simplify, we can separate the electron motion into a stationary (initial position), a rapidly varying (due to the laser frequency) and a slowly varying component, such that $x(t) = x_0 + x_{\text{fast}}(t) + x_{\text{slow}}(t)$. We also make the assumptions that the magnitude of the fast motion and its derivatives are much larger than the slowly varying motion, $x_{\text{fast}} \gg x_{\text{slow}}$. These two assumptions are known as the slowly-varying envelope approximation.

Taylor expanding the electric field about the initial electron position results in

$$E(x) = E(x_0) + \frac{dE(x_0)}{dx}(x - x0) = E(x_0) + \frac{dE(x_0)}{dx}(x_{\text{fast}} + x_{\text{slow}}). \tag{2.58}$$

With this substituting Equation 2.58 into Equation 2.57 gives us

$$m_e(\ddot{x}_{\text{fast}} + \ddot{x}_{\text{slow}}) = q\Big[E(x_0) + x_{\text{fast}}\frac{dE(x_0)}{dx} + x_{\text{slow}}\frac{dE(x_0)}{dx}\Big]\cos(k_0 z - \omega_0 t). \tag{2.59}$$

To first order we can neglect the time derivative of the slow electron motion ($\ddot{x}_{\text{fast}} \gg \ddot{x}_{\text{slow}}$) and the spatial derivatives because for high frequency light $E(x_0) \gg x_{\text{fast}}\dfrac{dE(x_0)}{dx}$. With this, substituting Equation 2.58 into Equation 2.57 gives us

$$m_e\ddot{x}_{\text{fast}} \approx -eE(x_0)\cos(k_0 z - \omega_0 t). \tag{2.60}$$

The first order solution can then be solved to find

$$x_{\text{fast}} = -\frac{eE(x_0)}{m_e\omega_0^2}\cos(k_0 z - \omega_0 t). \tag{2.61}$$

We can now determine the second order solution,

$$\ddot{x}_{\text{fast}} + \ddot{x}_{\text{slow}} = -\frac{e}{m_e}\Big[E(x_0) + x_{\text{fast}}\frac{dE(x_0)}{dx} + x_{\text{slow}}\frac{dE(x_0)}{dx}\Big]\cos\left(k_0 z - \omega_0 t\right). \tag{2.62}$$

Subtracting out the first order motion from Equation 2.60 and substituting Equation 2.61 yields

$$m_e\ddot{x}_{\text{slow}} = -ex_{\text{fast}}\frac{dE(x_0)}{dx}\cos\left(k_0 z - \omega_0 t\right) \tag{2.63}$$

$$m_e\ddot{x}_{\text{slow}} = -\frac{e^2 E(x_0)}{m_e\omega_0^2}\frac{dE(x_0)}{dx}\cos^2\left(k_0 z - \omega_0 t\right). \tag{2.64}$$

Using the chain rule, the term $E(x_0)\dfrac{dE(x_0)}{dx} = \dfrac{1}{2}\dfrac{dE^2(x_0)}{dx}$. Finally, because we are looking for slowly-varying motion, we take the time average over one laser period of the right hand side:

$$F_{\text{pond}} = m_e\frac{dx_{\text{slow}}^2}{dt^2} = -\frac{1}{4}\frac{e^2}{m_e\omega_0^2}\nabla||E||^2. \tag{2.65}$$

The ponderomotive force acts to slowly push charged particles away from regions of high electric fields. Ions will also experience the force, but with reduced strength due to the increase in mass compared to electrons. Notably, there exists no dependence on the sign of the electric charge; ions and electrons move in the same direction.

In general, the ponderomotive force has contributions from other terms, e.g. magnetic fields or circularly polarized light, and is a ubiquitous effect in high field laser-matter interactions. The relativistic generalization of the ponderomotive force [82] can be written in terms of the Lorentz factor as

$$F_{\text{pond}} = m_e c^2(\nabla < \gamma > -1) \tag{2.66}$$

where $< \gamma >$ is the time averaged of electron Lorentz factor over a laser cycle.

2.3 Laser-Solid Interactions

The field of plasma physics is truly diverse in scope. Astrophysical plasmas, magnetically-confined fusion, and laser-plasma interactions are only a few of the sub-fields. While seemingly disconnected in scope and scale there exists a common thread amongst all of plasma physics. This thesis will restrict our focus to the sub-field of relativistic, overdense, laser-plasma physics, but some core concepts of plasma physics will be briefly covered. In part, this is because the interaction of an intense laser with a plasma is highly dependent upon the laser *and* plasma conditions at the time of the interaction. For example, overdense, laser-plasma interactions are particularly interesting due to the the complex interplay between strong electric fields and a dense collection of charged particles. This section will briefly touch on a few select topics relevant to laser-solid interactions.

2.3.1 Laser Ionization Mechanisms

In order to generate a plasma, bound electrons must be freed from their parent nuclei. One such method of ionization is through photoionization, also known as the photoelectric effect [83]. For metals with electrons in the conduction band single photon ionization can occur for energies greater than a few eV, e.g. the common optical elements of aluminum and gold have work functions of 5.99eV (207nm) and 9.23eV (134nm), respectively. Dielectrics with larger bandgaps require higher photon energies to photoionize.[2] For NIR and optical lasers, the photon energies are not sufficient to cause single photon photoionization and thus this effect does not occur for interactions of interest in this thesis.

[2]For example, silicon photoionizes at 8.15eV.

Beyond single-photon ionization, there exist other mechanisms that cause electron ionization. Multi-photon ionization (MPI) can occur when multiple photons interact with an electron at the same time. This event can only occur when photon intensities are high enough for a significant probability that multiple photons are interacting with the same electron wavefunction. In the perturbative regime, the rate of ionization for n photons is given by

$$\Gamma_n = \sigma_n I_0^n \tag{2.67}$$

where the cross-section of the multi-photon interaction and the light intensity is given by σ and I_0 respectively. The higher value of n the smaller the interaction cross-section, requiring a significantly higher photon flux. This should make sense qualitatively; multiple photons absorbed by an atom is harder to achieve. Quantitatively, the number of photons per units time per units area is the photon flux, which is proportional to the photon, or laser, intensity.

At high enough intensities there exists a cross-over point where MPI becomes insignificant as tunnel ionization becomes available. Tunnel ionization occurs when the electric field of the laser becomes comparable with the atomic Coulombic potential. When this occurs, the electric field alters the potential well of the atom which becomes high asymmetric. This asymmetry enables the electron to tunnel through the potential barrier and escape into free space. An estimate of the necessary field strength can be made by considering the classical electric field strength of the Bohr atom at 500 GV/m when in the ground state.

We can define the laser field intensity as the time average of the Poynting vector,

$$I_0 =< \mathbf{S} >=< \frac{1}{\mu_0}\mathbf{E} \times \mathbf{B} >= \frac{\epsilon_0 c}{2} E_{Hydrogen}^2 \tag{2.68}$$

to arrive at an ionization intensity of $3.3 \times 10^{16}\mathrm{W/cm^2}$ for the hydrogen atom. These intensities are indeed achievable with moderate energy femtosecond laser systems.

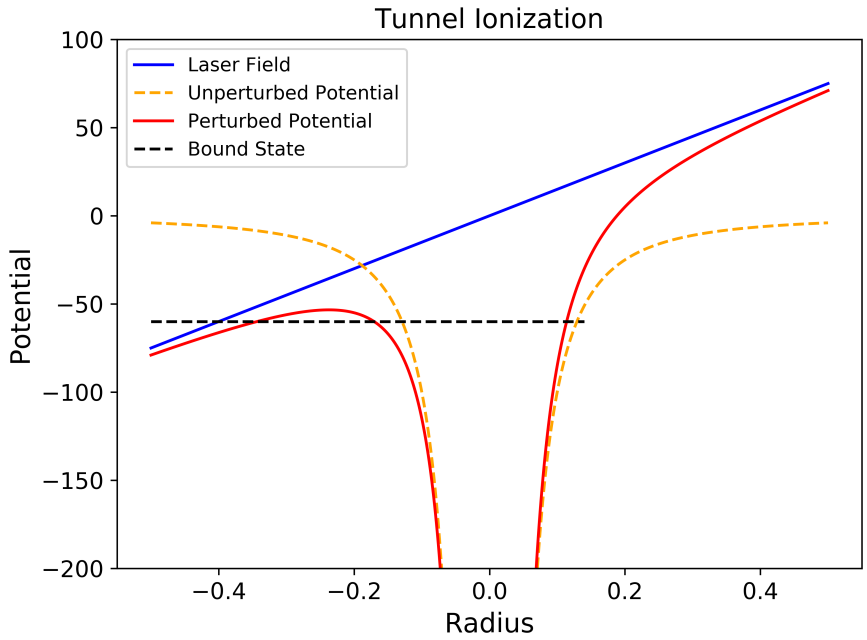

Figure 2.6: Diagram of tunnel ionization.

The transition point at which the laser intensity is high to cause a significant chance of tunneling ionization is given by the Keldysh parameter [84],

$$\gamma = \omega_0 \frac{\sqrt{2m_e\Phi}}{eE_0} \tag{2.69}$$

where Φ is the ionization potential and E_0 is the electric field of the laser. Keldysh found that multiphoton and tunneling ionization are the two limiting cases of nonlinear ionization mechanisms [85]. Tunnel ionization becomes dominant over multi-photon ionization when $\gamma \gg 1$.

Eventually, the laser field becomes so strong that the entire Coulomb potential barrier is below the electronic energy state; the electron is no longer bound. This is known as barrier suppression ionization (BSI) and occurs at very specific intensities, when the laser intensity induces a field equal to the ionization level of the electronic state. This intensity, known as

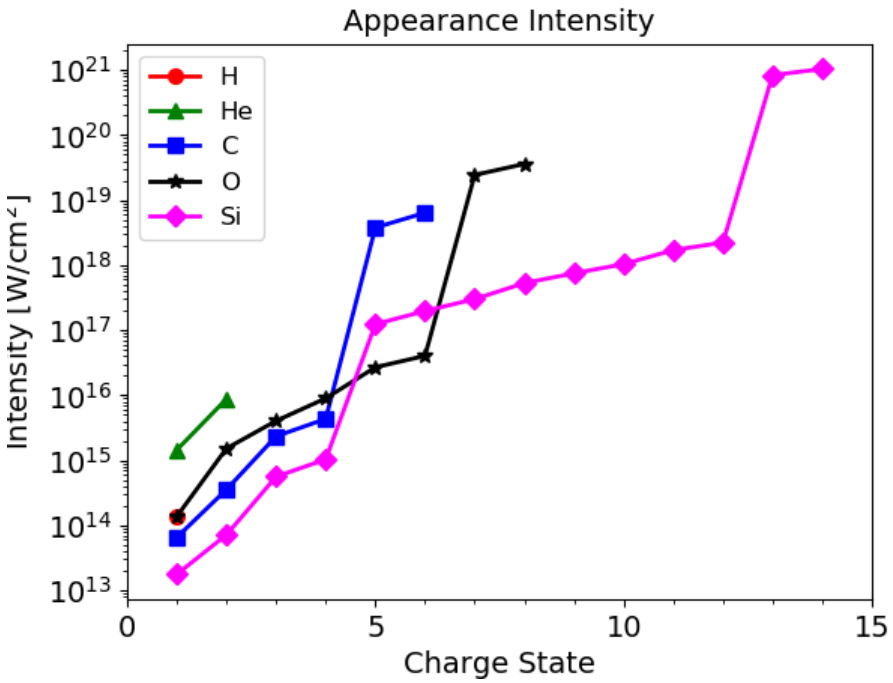

Figure 2.7: Appearance intensities of various elements. Note the significant jump that occurs when the ionization of a new electronic shell begins, e.g. the observation of O^{7+} indicates an intensity above 10^{19}W/cm^2.

the appearance intensity is given by

$$I_{\text{appearance}} = \frac{c\Phi}{128\pi Z^2 e^6} = 4 \times 10^9 E[\text{eV}]^4 Z^{-2}[\text{W/cm}^2] \tag{2.70}$$

where E and Z are the ionization energy and ionization state. The appearance intensity is when ionization occurs with one-hundred percent probability, the tunneling rate equals unity. The appearance intensities of a select group of elements can be found in Fig 2.7. The presence of a specific charge state can be an indication of a specific intensity threshold.

2.3.2 Electromagnetic Waves in Plasma

The interaction of an electromagnetic field propagating through a plasma is highly dependent upon the plasma density. As an example, consider a quasi-neutral, unmagnetized, cold

plasma in equilibrium. The index of refection of a cold, unmagnetized plasma is given by

$$n(\omega) = \sqrt{1 - \frac{\omega_p^2}{\omega^2}}, \tag{2.71}$$

where $\omega_{p,e}$ is the electron plasma frequency. The plasma frequency determines the characteristic time-scales of the plasma and is defined as:

$$\omega_{p,s} = \sqrt{\frac{n_s q_s^2}{\epsilon_0 m_s}}. \tag{2.72}$$

For non-relativistic ($\gamma \approx 1$) laser-plasma interactions, the plasma frequency depends exclusively on the plasma density. The plasma frequency is the natural oscillation rate of free particles within the plasma caused by Coulombic restoring forces acting on displaced particles, which for an electron in practical units can be expressed as

$$\omega_p = 5.64 \times 10^4 \sqrt{n_e[\mathrm{cm}^{-3}]}. \tag{2.73}$$

Since ions are much heavier than electrons, their motion is orders of magnitude smaller during the high frequency oscillations of a laser electric field.

From the index of refraction, it is possible to determine the electromagnetic dispersion relation by calculating the phase velocity of the wave in a material, or $v_p = \omega/k = c/n$. The dispersion relation of an electromagnetic field is given by:

$$\omega^2 = \omega_{p,e}^2 + k^2 c^2. \tag{2.74}$$

At high frequencies or low densities ($\omega \gg \omega_{p,e}$) we recover the usual vacuum dispersion relation of light $\omega = kc$. Conversely, electromagnetic waves in plasma densities corresponding to $\omega_{p,e} > \omega_0$ have imaginary wavenumbers, which mean they are evanescent. An electro-

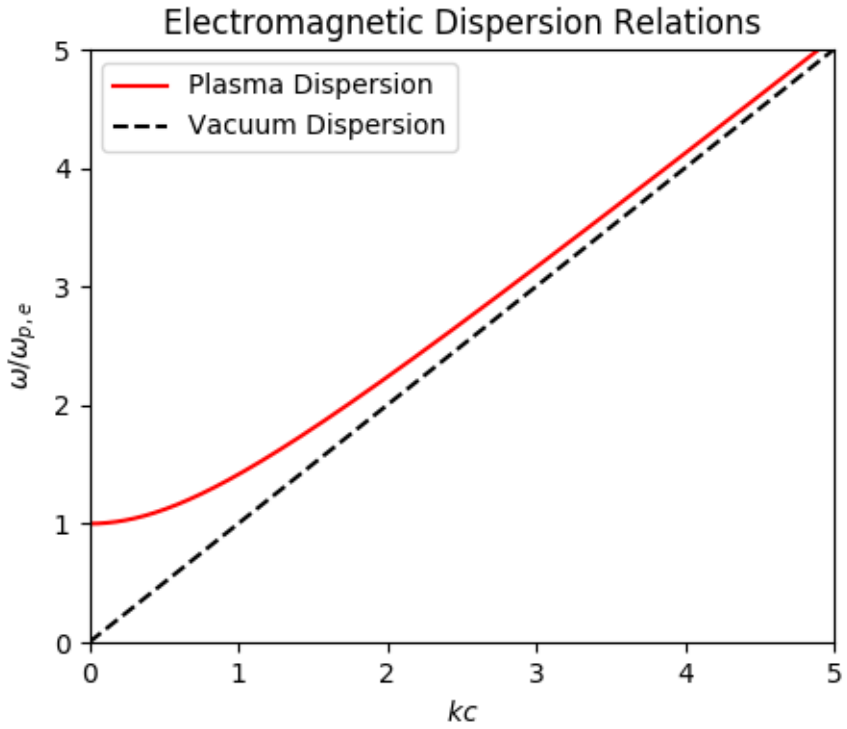

Figure 2.8: Electromagnetic dispersion relation in plasma (red) and vacuum (black dashed). Electromagnetic waves with frequencies $\omega < \omega_{p,e}$ have an imaginary wavenumber.

magnetic wave propagating through the pre-plasma of an overdense plasma produced by a solid target that begins near zero density and monotonically rising to near solid-density will experience an increasing plasma density as a function of distance. Once the laser reaches the plasma density corresponding to the cutoff frequency $\omega = \omega_{p,e}$ or $k^2 = 0$ the light wave will reflect in the backward direction and have an evanescent component in the forward direction. The length over which the evanescent wave decays to $1/e^2$ of the peak intensity is known as the skin depth $\delta = c/\omega_p$.

This point in the plasma - where the plasma becomes opaque and reflective - is known as the critical density. This can be understood in a microscopic sense by considering how a single electron will respond to two different laser frequencies. For low frequency light, a free electron at the critical density will naturally oscillate fast enough to re-radiate the incident laser. This re-radiation acts as the reflection point for the laser. However, electrons will not be able to oscillate at the necessary rate to respond to and re-radiate higher frequency light.

The critical density of light with frequency ω_0 can easily be found by setting $\omega_0 = \omega_p$, and in practical units can be expressed as

$$n_c = \frac{\epsilon_0 m_e \omega_0^2}{e^2} = 1.12 \times 10^{21} [\mathrm{cm}^{-3}] \frac{1}{\lambda_0 [\mu\mathrm{m}]^2}. \tag{2.75}$$

A plasma that is below the critical density is known as underdense, while a plasma that is above the critical density is known as overdense. For lasers with central frequencies in the visible or NIR, underdense plasmas are typically produced in laser-gas interactions, while overdense plasmas are typically produced in laser-solid interactions.

2.3.3 Relativistic Effects

The above plasma parameters were derived assuming non-relativistic motion. Since an electron is a massive particle, it obeys the relativistic momentum formulation, $p = \gamma m_e v$, so as it gains velocity its momentum increases towards infinity. In the lab frame, this is generally viewed as an effective increase to the electron mass. In many cases it is possible to convert between a non-relativistic and relativistic interaction by simply replacing the electron mass m_e with γm_e, where $\gamma = \sqrt{\frac{1}{1-\beta^2}}$ is the Lorentz factor.

Relativistic effects have profound consequences in laser-plasma interactions. The plasma frequency,

$$\omega^2 = \frac{n_e e^2}{\epsilon_0 \gamma m_e}, \tag{2.76}$$

decreases as the electrons gain more inertia. This prevents electrons from oscillating fast enough to re-radiate frequencies previously possible, which modifies the plasma critical den-

sity

$$n_c = 1.12 \times 10^{21}[\mathrm{cm}^{-3}]\frac{\gamma}{\lambda_0[\mu\mathrm{m}]^2}. \tag{2.77}$$

Thus it is possible for an opaque plasma to become transparent in what is known as relativistically-induced transparent. The plasma skin depth also needs to be adjusted. A relativistically-intense laser can penetrate much deeper into an opaque plasma.

Gaining a dynamic understanding of how these parameters vary during a relativistic interaction is non-trivial. A laser pulse with a non-uniform focal spot results in a critical surface that varies across the focal plane of the interaction. Further complicating the issue the that laser pulse durations are typically Gaussian and plasma profiles are not step-like. As a relativistically intense laser propagates into a pre-formed plasma, different densities will experiences different intensities.

2.3.4 Pre-plasma Scale Length

One of the most important characterizations of a plasma interface is its density profile at the time of arrival of the main laser pulse. Once the ionization of a solid-density target occurs, the plasma will begin to hydrodynamically expand into the vacuum in front of the target [86]. The density evolution will begin once the laser field strength is sufficient to cause ionization, which for many materials are intensities on the order of 10^{13} W/cm^2 or lower depending on the ionization mechanism. At relativistic intensities the laser contrast and the presense of pre-pulses can cause target ionization picoseconds-to-nanoseconds prior to the arrival of the main pulse. For ionization occurring on these time-scales, the speed of plasma expansion may be approximated as the ion-acoustic speed expressed as

$$c_s = \sqrt{\frac{ZT_e}{m_i}}, \tag{2.78}$$

where Z and m_i are the charge and mass of the ions in question [86, 87]. By assuming the expansion occurs from the time of ionization to the arrival of the high-intensity, short-pulse, $\tau_{\mathrm{pre-pulse}}$ the expansion length can be calculated as $L \approx= c_s \tau_{\mathrm{pre-pulse}}$. For example, a laser pre-pulse could cause a silicon target to singly-ionize at $\tau_{\mathrm{pre-pulse}} = 10$ ps, and produces an average electron temperature $T_e = 100$ eV. This would lead to an ion-acoustic speed of $c_s \approx 18.5$ nm/ps, and a plasma expansion length of 185 nm before the arrival of the main pulse. Of course, ionization and electron heating do not occur at a single point in time, and more accurate estimates of the plasma expansion can be performed by using hydrodynamic simulation codes.

In short-pulse, laser-solid interactions the density profile is assumed to have a simple profile (e.g. linear or exponential) with some characteristic scale length defined as

$$L_s = n(z)(\frac{dn(z)}{dz})^{-1} \tag{2.79}$$

For an exponential profile, $n(z) = n_0 e^{\alpha z}$, this gives the convenient result of

$$L_s = n_0 e^{\alpha z}(n_0 \alpha e^{\alpha z})^{-1} = \alpha^{-1}. \tag{2.80}$$

Short scale lengths ($L_s < \lambda_0/2$) can be ideal for femtosecond laser-solid interactions. For example, relativistic harmonic generation requires a well-defined critical density surface to maintain phase-locking of the harmonic emission without driving plasma waves [88–90]. Experiments with long-pulse lasers ($\tau >$ 1ps) have shown that the ponderomotive force is able to steepen initially long scale length prior to the interaction [91]. However, femtosecond lasers are too short and low energy to produce significant profile steepening. Therefore, significant care must be taken to increase laser contrast to suitable levels to reduce the plasma scale-length. One benefit gained by studying laser-plasma interactions from light generated

through OPA is the inherently high contrast from the non-linear generation process. This contrast can be further increased when using light generated from a non-collinear OPA geometry.

2.4 Laser Heating Mechanisms

Laser energy from high-intensity, ultrafast pulses can couple into solid-density plasmas through a variety of mechanisms depending on intensity, density profile, incidence angle, and polarization. These plasma heating mechanisms can be separated into collisional and collisionless processes. Collisional processes, generally referred to as inverse-Bremsstrahlung heating, involves discreet electron-ion collisions. However, when the pulse intensity exceeds $10^{16}\mathrm{W/cm}^2$, the electrons become to energetic to efficiently couple their energy into the plasma ions, reducing the importance of inverse-Bremsstrahlung heating. At relativistic intensites with solid-density targets, the inverse-Bremsstrahlung heating is entirely dominated by collisionless mechanisms such as resonance absorption, Brunel heating and $\mathbf{J} \times \mathbf{B}$. However, for low-contrast systems, collisional heating is important for pre-heating of the plasma by the nanosecond pre-pulse. This heating can substantially alter the plasma density profile, and influence the main pulse interaction.

2.4.1 Resonance Absorption

Resonance absorption occurs when moderate intensity pulses, $I \sim 10^{15}\mathrm{W/cm}^2$, with P-polarized reflect at an oblique incidence off a plasma surface with varying density profile [92, 93]. Consider an electromagnetic wave with frequency ω_0 propagating in a cold plasma

with dielectric function

$$\epsilon(x) = 1 - \frac{\omega_{p,e}^2(x)}{\omega_0^2}(1 + \frac{i\nu}{\omega_0}), \tag{2.81}$$

where $\omega_{p,e}(x)$ is the electron plasma frequency at different locations in the plasma and ν is a collisional frequency. For P-polarization, the electric field has a component parallel to the surface, and at the laser reflection point, Gauss's Law states $\nabla \cdot (\epsilon \mathbf{E}) = 0$. In the limit of a collisionless plasma, $\nu/\omega_0 \ll 1$, we have

$$\nabla \cdot [(1 - \frac{\omega_{p,e}^2}{\omega_0^2}\mathbf{E}] = \nabla \cdot [(1 - \frac{n_e}{n_c}\mathbf{E}] = 0, \tag{2.82}$$

where a resonance condition occurs at the critical density n_c, whereby the laser field is able to efficiently drive plasma waves near the critical density surface. For an oblique incidence θ, the laser field never reaches the critical density surface, instead the wave becomes evanescent at a density $n_e = n_c \cos^2\theta$. However, the evanescent component may reach the critical density surface to drive a plasma wave [94]. The coupling of laser energy into driving this plasma wave depends both on the angle of incidence and plasma scale length, L_s. For example, for $k_0 L_s = 10$, the optimum angle is given by $(k_0 L_s)^{2/3} \sin^2\theta \simeq 0.7$, or 23° with an absorption coefficient of nearly 40%. The minimum conditions for resonance absorption occur in the limit of grazing incidence or normal incidence, when the evanescent wave does not penetrate deeply into the plasma or there is no longitudinal electric field component. Resonance absorption can contribute to significant heating of the target for low-contrast laser pulses prior to the arrival of the main pulse.

2.4.2 Brunel Heating

Extremely short-density profiles found in high-contrast experiments remove the resonant conditions necessary for strong resonance absorption. Laser fields incident on these sharp

density gradients can interact directly at the critical density surface and pull electrons from inside the plasma into the vacuum before reaccelerating them deep into the plasma beyond the critical surface where the laser field is evanescent. The description of this absorption process is now termed Brunel[3] or vacuum heating [95].

For pulses approaching relativistic intensities, i.e. $I\lambda^2 \geq 10^{16}$ Wcm$^{-2}\mu$m^2, electrons move in a laser field distances of v_{osc}/ω_0. If the laser is interacting with an overdense plasma with P-polarization, the electron motion in and out of the critical surface will be a distance of $v_{osc}/\omega_0 \sin\theta$. For an 800 nm pulse with normalized vector potential $a_0 = 1$ incident at 45°, the electron quiver velocity is $v_{osc} = c/\sqrt{2}$ and the motion along target normal is $v_{osc}/\omega_0 \sin(45°) = 63$ nm. Conversely, the plasma skin depth of a solid density target is on the order of 10 nm. Electrons pulled into the vacuum by the relativistic pulse will be accelerated into the dense plasma. Because the laser is rapidly attenuated past the critical surface, the electrons do not experience the field reversing signs, and will continue into the target as energetic particles.

A similar mechanism to Brunel heating exists for relativistically intense pulses at normal incidence. At the surface of steep gradients, normal incidence lasers can drive electrons into the overdense plasma through the $\mathbf{v} \times \mathbf{B}$ components of the Lorentz force. This is known as relativistic $\mathbf{j} \times \mathbf{B}$ heating or Wilk's heating [32]. Wilk's found through numerical methods that the accelerated electrons will have a Maxwellian distribution function with temperatures given by

$$U_p = mc^2(\sqrt{1 + a_0^2} - 1), \tag{2.83}$$

where U_p is the ponderomotive potential [32].

[3]In fact, Brunel's initial paper is called "not-so-resonant, resonant absorption."

2.5 Radiation Generation

Short-pulse lasers interacting with solid-density targets are capable of generating short wavelength radiation through various mechanisms. Some of these methods include hard x-rays from atomic processes such as Bremsstrahlung radiation and atomic x-ray emission as well as extreme ultraviolet radiation through high harmonic generation.

2.5.1 Hard X-ray Sources

When an intense laser interacts with an overdense plasma, the surface electrons are heated through various heating mechanisms discussed in Section 2.4. The hot electrons heated from relativistically-intense interactions will have energies in the hundreds of keV - MeV range, which enable the electrons to ionize inner-shell electrons from neutrals and ions in the plasma. Electronic transitions from the outer shells results in either the emission of a high energy photon or an Auger electron with characteristic energy. The energy level difference is emitted as a photon during the transition. If the electron is emitted from the innermost shell ($n = 1$ state), then the radiation produced from an electron transitioning from the next outer shell ($n = 2$ state) is known as $K\alpha$ emission. These emission lines are characteristic signatures of the constituent ions in the plasma. For plasmas with temperatures exceeding 1 keV the ion species can become highly-ionized with only a few bound electrons. This can substantially shift the atomic energy level potentials and resulting emission line intensity and energy. The analysis of atomic spectral lines gives useful information about the ionization states found in the plasma as well as conditions such as electron temperature and density, making plasma spectroscopy a valuable plasma diagnostic [62, 96].

Bremsstrahlung radiation[4] occurs when a high energy electron is decelerated by a nearby positively-charged nucleus due to the Coulomb force. The energy lost by the decelerating

[4]German for "Breaking Radiation"

electron will be emitted as a high energy photon. The magnitude of the deceleration, and the radiated energy, is proportional to the proximity of the electron trajectory and the charge of nucleus charge. The highest possible energy emitted by an electron is equal to the incident kinetic energy of the electron in the case where it comes to a complete stop.

2.5.2 High Harmonic Generation

High harmonic generation (HHG) was first observed using a nanosecond CO_2 laser incident on a solid density target. The terminology of "harmonic generation" is mainly use for convenience and tradition. When discussing the generation of higher energy radiation by some perturbative interaction in a material, the generation of harmonics is easily understood. Multiple photons of a single wavelength (two for second harmonic generation, three for third harmonic generation) are converted in to one higher energy photon through some energy level excitation and relaxation. These processes are very well explained through a quantum mechanical process.

Fundamentally, harmonic generation from solids is a very different process. While the conservation laws of momentum and energy are still preserved, the harmonic nature of the emitted radiation is instead due to the periodicity of the driving laser. The radiation generation processes are repeated periodically locked to the laser cycle. Fourier theory enforces that a periodic signal must comprise of the harmonics of the fundamental driver, in this case the fundamental frequency of the laser. When a harmonic generation process occurs only once, e.g. with a single-cycle laser, the radiation will not be harmonic in nature.

At the highest peak powers available through Petawatt-class ($P_{\max} \approx 10^{15}$ W) laser systems, overdense laser-plasma interactions have the potential to generate the coherent short-wavelength light producing bright, sub-fs pulse durations. Lasers with normalized vector potentials $a_0 \gg 1$ driving overdense interactions can produce harmonics extending deep into

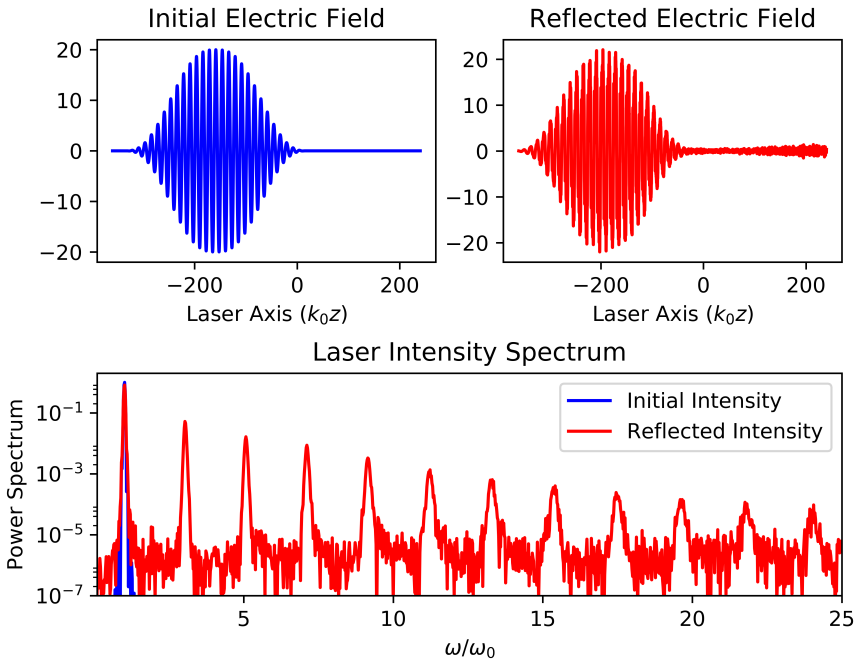

Figure 2.9: Electric field of a laser before (blue) and after (red) reflection from an overdense plasma surface. Laser harmonics are observed in the reflected intensity spectrum.

the EUV [24]. The short pulse durations of such EUV sources enable the study of attosecond science [74–77] while achieving spatial resolutions required for nanometer-scale imaging. These pulses could be used to drive laser wakefield accelerators in solid density targets [97] which have been shown in simulations to provide extremely high acceleration gradients of up to TeV/cm [35, 36].

2.5.3 Harmonic Generation Mechanisms

Two mechanisms used to describe of high harmonic generation in laser-solid interactions are coherent wake emission (CWE) [98] and the relativistically oscillating mirror (ROM) model [23, 99, 100]. These two mechanism reside in entirely separate regimes delineated by the laser intensity and plasma density scale-length. Roughly, CWE dominates for lower intensities ($a_0 < 1$) and shorter scale lengths ($L_s < \lambda/10$) while ROM dominates for higher intensities ($a_0 > 1$) and longer scale lengths ($L_s > \lambda/10$). That being said, it is possible for

both mechanisms to exist in the transition regime, and so careful study must be taken to determine the dominant effect [101, 102].

2.5.4 Coherent Wake Emission

Coherent wake emission occurs through the excitation of plasma wakes by high energy electrons driven into an overdense plasma. These wakes are capable of exciting longitudinal plasma oscillations in the overdense region. These oscillations are capable of subsequently emitting an attosecond EUV burst through linear-mode conversion into transverse electromagnetic modes [98]. The limiting frequency in CWE is the maximum plasma frequency of the solid target, because the turning point of optical waves (where the amplification phase matching occurs) is near the corresponding critical densities. Because solid target plasmas do not possess step-like density-profiles, the frequencies emitted are generated at a different depth into the plasma (deeper for higher energy light) defined by $\omega = \omega_p(x) = \sqrt{\frac{n_e(x)e^2}{m_e\epsilon_0}}$. This leads to a positive chirp of the spectrum, i.e. lower frequency light travels in front of higher frequency components. Repeated over many laser cycles, this process leads to an attosecond pulse train that produces a harmonic spectrum.

2.5.5 Relativistically Oscillating Mirror Model

Relativistic harmonic generation driven by the reflection of light off an overdense plasma mirror, which can be described by the relativistically oscillating mirror (ROM) model [23, 39, 41, 99], offers a promising means of producing high-brightness, attosecond-duration light in the extreme ultraviolet (EUV) and soft x-ray regions that can extend hundreds of harmonic orders with high-single shot flux and inherent phase matching [24, 42, 43, 103].

When an intense laser is incident on a plasma surface, it will propagate into the plasma

until it reflects off the critical plasma density. The critical surface electrons electrons that are driven into the plasma by the laser field experience a restoring force from the nearly-immobile ions. When the electron motion becomes relativistic, i.e. when $a_0 \gtrsim 1$, electrons located at the critical density surface are driven to relativistic velocities within an optical cycle. The resulting driving force from the laser coupled with the plasma pressure from the ions leads to a nonlinear, oscillating reflection surface of the plasma which changes as a function of time [100]. Therefore, a nonlinear phase shift, $\phi(t)$, is imparted by the oscillating mirror onto the laser field. This phase shift is determined by the oscillation modes, ω_m, of the mirror surface:

$$\phi(t) = \sum \phi_0 \sin(\omega_m t). \tag{2.84}$$

The reflected electric field, E_r, of the laser field is then given by

$$E_r \propto \exp(-i\omega t) \exp i\phi(t) = \exp(-i\omega t) \sum_{n=-\infty}^{n=\infty} J_n \exp(-in\omega_m t), \tag{2.85}$$

where J_n are Bessel functions of the first kind [99]. When the driving laser is a multi-cycle pulse the oscillation modes of the plasma surface are at frequencies linked to the laser optical cycle, and the re-radiated field in the spectral domain contains the higher order harmonics of the incident laser.

The ROM mechanism has characteristic universal properties [42]. For example, the allowed harmonic orders and their individual polarization states are determined by the interaction geometry and critical surface oscillation modes [99]. A laser field reflecting off a surface at normal incidence produces a single mirror oscillation mode at frequency 2ω. The reflected field will contain the odd harmonics of the laser $\omega_n = (2n+1)\omega$. At oblique incidence, the symmetry of the interaction is broken and the surface can now oscillate at frequency ω. The

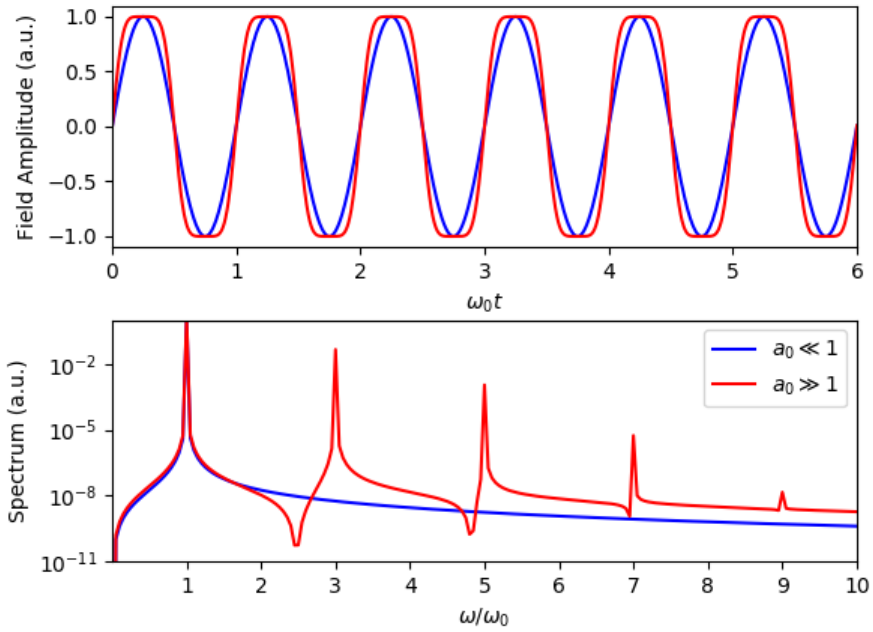

Figure 2.10: Spectral modulation of laser interacting with relativistically oscillating mirror at normal incidence. The reflected spectrum contains only odd multiples of the fundamental frequency.

reflected field will contain even harmonics polarized along the electric field direction, and odd harmonics polarized parallel or orthogonal to the electric field for p- and s-polarized interactions, respectively. The harmonic polarization selection rules for ROM HHG can be found in table 2.1:

	S-pol. Harmonics	P-pol. Harmonics
S-pol. Fundamental	odd	even
P-pol. Fundamental	forbidden	odd and even

Table 2.1: Oscillating Mirror Model harmonic polarization selection rules. Note that a p-polarized fundamental laser cannot produce s-polarized harmonic emission.

The ROM model of harmonic generation relies on the formation of a well-defined critical density surface. From an experimental perspective, this means that it is important to avoid significant formation of an underdense pre-plasma as this degrades the quality of a well-defined reflection point. Naively, this would imply that high-intensity lasers with high-contrast are ideal candidates to generate relativistic harmonics with good efficiency. However,

it has been experimentally observed that ultrahigh-contrast lasers have less efficiency than those with an added heating beam to introduce a short pre-plasma scale [89, 90, 104].

Relativistic HHG - Ultraintense, Attosecond X-ray Pulses

Relativistic harmonic generation occurs from the radiation at one oscillating surface, which means that ROM harmonics are not inherently chirped enabling the generation of sub-femtosecond pulses from the interaction [27, 42, 43]. Multi-cycle drivers emit a burst of radiation each optical cycle, which inhibits the generation of an isolated, x-ray pulse. However, if the driving laser field is a few-cycle pulse, the generating radiation would instead be an isolated pulse with broadband continuum. The recently proposed technique of Thin Film Compression (TFC) [44] has been proposed as one means to compress PW-class laser systems to the single-cycle limit ($\sim$ 3 fs). After TFC the optical pulse is then focused onto an overdense plasma to drive relativistic harmonic generation producing a single-cycle x-ray pulse with Joules of energy and pulse durations as low as attoseconds or zeptoseconds.

Since the conversion efficiency of the oscillating mirror model strongly depends on the electron acceleration at the critical surface, there is no upper limit to the intensity necessary for harmonic generation. Harmonics from the ROM mechanism has been observed from $a_0 \sim 1$ [6, 101] up to $a_0 \gg 1$ [24, 90]. Therefore, relativistic high harmonic generation has been proposed as one possible method to achieve intensities exceeding the Schwinger limit ($I > 4.6 \times 10^{29}$ W/cm^2), above which the electric field is sufficiently strong such that pair production from the vacuum can occur [105]. While directly achieving the Schwinger limit is currently well beyond the highest intensity with current PW-class lasers. However, it has been suggested that a substantial enhancement of the initial laser focal intensity can be achieved by the focusing of relativistic harmonics [106]. An initial laser intensity of $I \sim 5 \times 10^{22}$ W/cm^2 is predicted to achieve the Schwinger limit in the harmonic focus.

Chapter 3

Methods

The experiments discussed in this thesis were conducted at a variety of laser facilities, including the Ultrafast Laser-Plasma Interaction Lab at the University of California, Irvine (UCI), the Relativistic Lambda-Cubed Laser at the Gérard Mourou Center for Ultrafast Optical Science (CUOS) at the University of Michigan, and the Laboratory for Advanced Lasers and Extreme Photonics Laser at Colorado State University. This chapter describes the laser systems, experimental configurations, and relevant diagnostics. The design and implementation of a high-intensity, laser-solid interaction platform for high repetition rate laser-solid experiments at UCI is discussed in detail. A suite of diagnostics for characterizing the laser prior to the interaction as well as capturing the resulting radiation was employed to gain as many simultaneous measurements as possible.

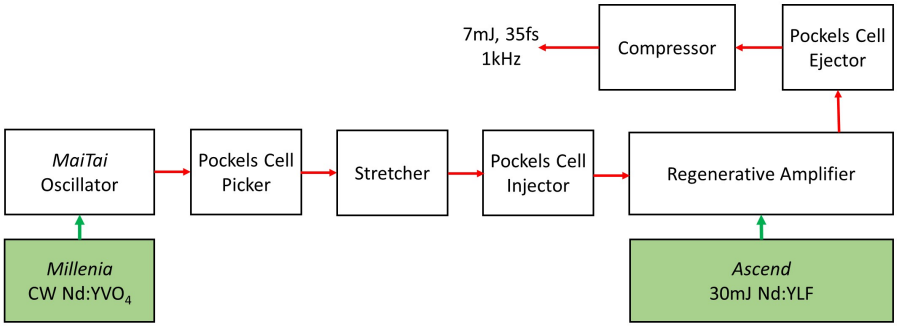

Figure 3.1: Schematic of Solstice laser.

3.1 Laser Systems

3.1.1 University of California, Irvine Laser

The UCI laser system is a commercial, high repetition rate mJ-class Ti:Sapphire laser (Spectra-Physics Solstice ACE) with a peak output power of 200 GW. The CPA system consists of an oscillator, stretcher, regenerative amplifier, and finally the compressor. The oscillator (Spectra-Physics Mai Tai SP) is a Kerr-lens mode-locked, pulsed Ti:Sapphire laser pumped at 532 nm by a frequency-doubled, diode-pumped, CW Nd:YVO_4 laser producing femtosecond 6 nJ seed pulses with a bandwidth of 60nm at a repetition rate of 42 MHz. In order to decrease the repetition rate to 1 kHz, a Pockel's cell and polarizer are placed at the output of the oscillator. Pockel's cells use an electro-optic effect which produces a birefringence in the optical medium due to an induced electric field. This rotates the laser polarization and enables it to be used as a temporal switch when combined with a polarizer. Then, the pulses are stretched for amplification below the damage threshold of the optics. A regenerative amplifier pumped at 527 nm by a frequency-doubled, diode-pumped, Q-switched Nd:YLF laser (Spectra-Physics Ascend 60) amplifies the pulses to 10 mJ of energy. Finally, the pulses are compressed with a single gold-coated holographic grating aligned in the Treacy geometry using roof mirrors to conserve space. The output pulse energy of the pulses are 7 mJ with 35 fs temporal FWHM. The output of the laser can be down-converted to 1.1 mJ

of $\lambda_0 = 1.3\,\mu m$ and 0.6mJ of $\lambda_0 = 2.1\,\mu m$ through a two-stage, collinear OPA.

3.1.2 Lambda-Cubed, University of Michigan

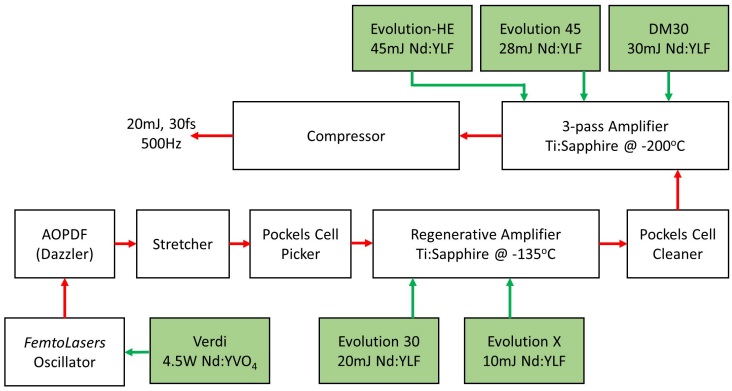

Figure 3.2: Schematic of Lambda Cubed laser.

The Relativistic Lambda-Cubed Laser system is a home-built high repetition rate mJ-class Ti:Sapphire laser. The system is seeded by a FemtoLasers Ti:Sapphire oscillator that produces 12 fs pulses with an accompanying carrier envelope phase (CEP) locking system. A radio frequency addressable acousto-optic programmable dispersive filter (AOPDF) called a "Dazzler" controls the spectral amplitude and phase of these seed pulses. Selected pulses from the Dazzler are stretched to ~200 ps and amplified to 7 mJ in a cryogenically cooled regenerative amplifier. The output pulse are then sent through a 3-pass amplifier that produces 28 mJ pulses prior to compression. The total efficiency of the compressor is 71% after four reflections and the output 20 mJ laser pulses have a 30 fs temporal FWHM duration at a 500 Hz repetition rate. Throughout the system, pump light is provided by a variety of frequency-doubled Nd-doped YAG, YLF and vanadate lasers.

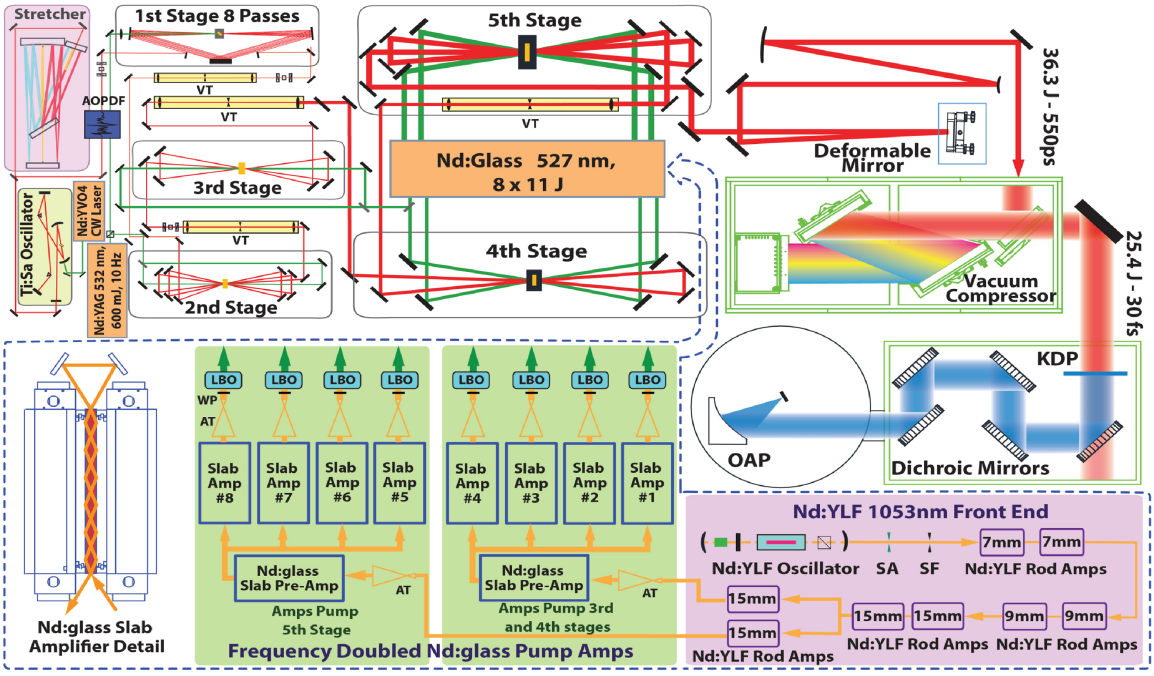

Figure 3.3: Schematic of ALEPH. Image credit: [3]

3.1.3 ALEPH Laser

The Colorado State University Advanced Laser for Extreme Photonics (ALEPH) is a Petawatt-class, short-pulse Ti:Sapphire laser system. A detailed description of the laser system can be found in [3] and Figure 3.3. The system consists of a conventional Ti:Sapphire front end that delivers pulses to a three-stage, high-power amplification chain pumped by Nd:YAG slab amplifiers bringing the laser pulses up to 250 mJ. The output is further amplified by three multi-pass amplifiers pumped by Nd:glass slab amplifiers. The slab geometry allows operation of the fully-amplified beam at a repetition-rate of up to 3.3 Hz. The eight slab amplifiers generate pulses with a total of $\sim$ 88 J of second harmonic light at 527 nm. A gold grating compression compresses the 37 J fundamental to up to 26 J with pulse duration as short as 30 fs. The compressed pulses can then be frequency-doubled using a Potassium dihydrogen phosphate (KDP) crystal to produce ultrahigh-contrast $\lambda = 400$ nm pulses up to 10 J with 45 fs FWHM pulse duration. The use of the laser second harmonic suppresses laser pre-pulse producing ultrahigh contrasts ($> 10^{11}$) that lead to hot, solid-density plasma [63].

3.2 UCI Laser-Solid Experiments

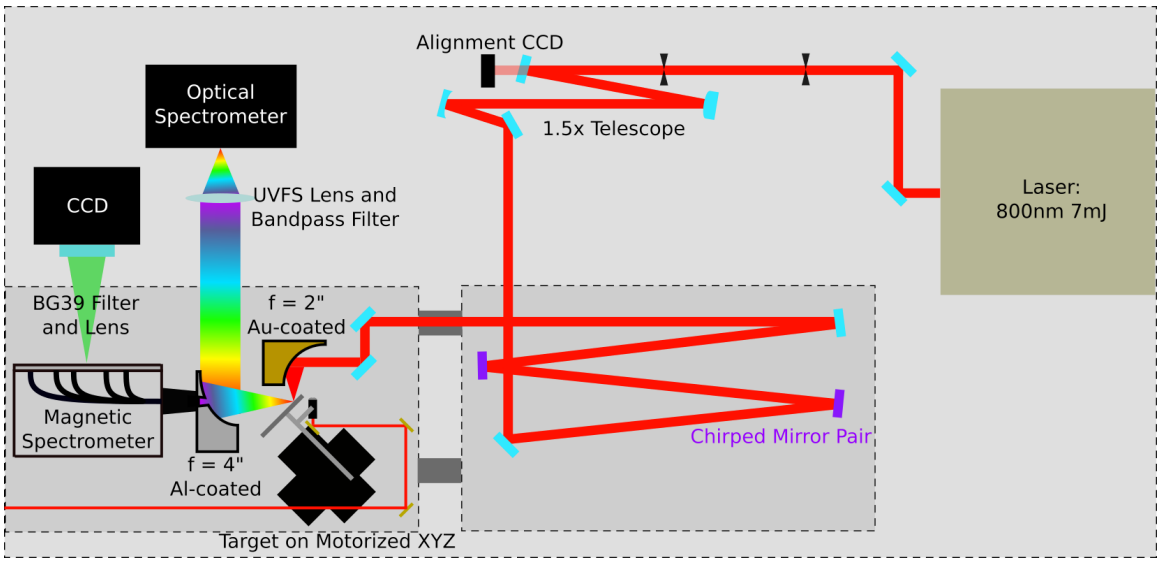

Figure 3.4: Laser-solid platform developed at UCI.

UCI has a modular experimental area which can accommodate a wide array of laser-matter interaction experiments. A typical laser-solid experiment will be described in the following section.

After compression, the Solstice output beam diameter is ~ 13 mm $1/e^2$. The output pulse is propagates through ~ 2 m of air. Presently, among the steering mirrors in air is an optional upcollimation telescope that can increase the beam size to 20 mm. This telescope helps in both reducing the B-integral during propagation into the vacuum system and decreasing the f/# of the focal geometry. The beam then is transmitted through an anti-reflection-coated UV-grade fused silica vacuum window (Thorlabs VPW42-B) At transport intensities ($I = 300\,\mathrm{GW/cm^2}$) the combination of self-phase modulation and dispersion introduced by the propagation through air and the vacuum window prior to entering the vacuum system increased the pulse duration from $\tau \sim 35$ fs to $\tau > 60$ fs. Therefore, a second vacuum chamber was introduced that contains a chirped mirror pair (-250 $\mathrm{fs^2}$) to compensate for the positive GDD from material dispersion and SPM. This enabled compression to slightly shorter pulse durations than initially output by the laser at $\tau \sim 30$fs. All other optics

employed in high intensity experiments are reflective optics. These include a combination of high-reflectivity dielectric ($R > 99.5\%$) and metallic coatings to reduce the total laser absorption during propagation through the system. Laser-solid experiments are conducted using a protected gold-coated $f = 2$" off-axis parabolic mirror. Typical experiments are conducted using an $f/2$ geometry, but $f/1$ capabilities have been used in experiments when higher intensities are required.

Laser Temporal Characterization

For experiments conducted at UCI, a custom built [4] Second Harmonic Generation Frequency Resolved Optical Gating (SHG-FROG) [107] measured the temporal profile of the laser. FROG is a technique commonly used to measure ultrafast pulse durations. The input pulse is split into two identical beams using a coated pellicle; one beam travels along a fixed reference path while the other travels along a delay line. Both beams are then focused onto a nonlinear crystal (BBO), which produces a second harmonic signal when the beams are spatio-temporally overlapped. The signal strength of the SHG is gated by changing the path length of one pulse with respect to the other. When the pulses no longer overlap, the SHG response disappears. If only the intensity of SHG signal was recorded, then this would be known as an intensity autocorrelation, which can be used to infer the pulse duration by assuming a pulse shape. FROG measurements acquire more information by recording the spectrum of the second harmonoic at each delay position. The additional information gained from the spectral data allows FROG to determine both the pulse spectrum and phase, thereby allowing a full reconstruction of the pulse. The intensity of the SHG FROG used commonly in the lab is given by

$$I(\omega, \tau) = | \int^{-} \infty_{\infty} E(t)E(t-\tau)e^{-i\omega t}dt|^2, \tag{3.1}$$

where τ is the delay between the two beams at each step. An iterative algorithm can then be used to reconstruct the time-dependent electric field from the FROG trace [107].

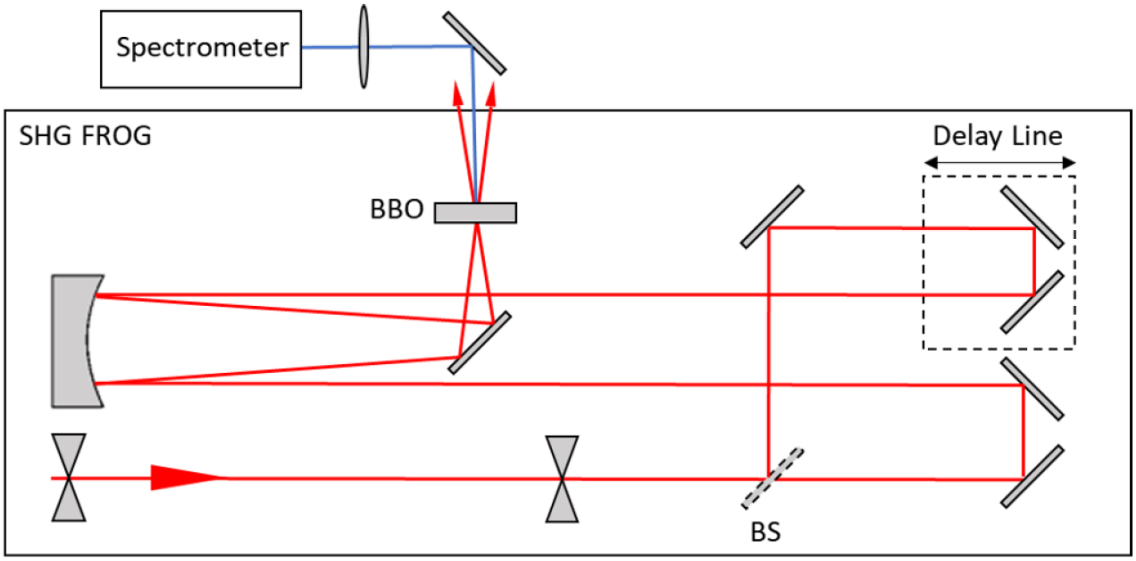

Figure 3.5: Schematic of home-built FROG. Image courtesy of [4]

Laser Focus Characterization

The output wavefront of the laser system has been measured with a Shack-Hartmann wavefront sensor. The Strehl ratio, or the ratio of the measured peak focal intensity of the input beam compared to a perfect wavefront, has been measured to be > 0.9. After beam expansion through the use of spherical mirrors, the Strehl ratio is lowered, but high quality focal spots are still routinely measured during experiments. *In situ* monitoring of the focal spot is achieved by imaging with an infinity-corrected microscope objective and BK-7 plano-convex lens coupled to a CMOS camera (Basler ace). The energy of the laser was reduced before the objective lens in order to avoid damage. Three methods were employed: using glass wedges positioned near Brewster's angle, by operating the laser in "shuttered mode," or by de-timing the first Pockel's cell before the stretcher. The shuttered method closes a mechanical shutter after the oscillator output but before the pulse stretcher, which prevents seed pulses from entering the regenerative cavity. Only ASE signal is output from the regen

and could be used for safe alignment. By de-timing the triggering signal sent to the first the Pockel's cell the seed pulse will not experience the Kerr-rotation needed to pass through the pulse picker. A small amount of seed light makes it through the polarization optics and into the regenerative amplifier, so extra care is required to not prevent damage during alignment now. Comparison measurements between fully-amplified shots imaged with wedged reflections and the ASE signal from the shuttered mode or de-timing mode showed no difference in focal spot quality.

A limiting factor for reaching the highest intensities is the optical flatness and the surface roughness of the OAP, which can introduce wavefront aberrations and optically scatter a significant amount of light. For example, the optics used at UCI from Edmund Optics have a quoted optical flatness of $\lambda/4$ and a surface roughness of ~ 50Å. Flat mirrors made by Edmund can have a quoted surface flatness of up to $\lambda/20$. To help estimate the peak laser intensity, the on-target energy was measured at low amplification. This process used a combination of pinhole, fast photo-diode, filter stack, and CMOS camera. The energy loss due to scattering by a fresh OAP was measured to be $\sim 1\%$ using a 50 μm pinhole and a fast (nanosecond response time) photodiode. Afterwards, the focal spot was imaged using a microscope objective and CMOS camera with neutral density filter stack to increase the dynamic range of the detector. This measurement showed that 45-50% of the incident laser energy reaches the FWHM of the laser focus. The OAP was manually aligned using this imaging system in air by correcting for astigmatism. The focal spot was monitored during pumpdown to enables minor corrections under vacuum by adjusting the final steering mirror before the vacuum chamber. Figure 3.6 shows an example of the laser focus under vacuum, the measured focal spots after correction is typically $1.9\mu\text{m} \pm 0.1\mu\text{m}$ for $f/2$ experiments and $1.4\mu\text{m} \pm 0.1\mu\text{m} \times\ 1.1\mu\text{m} \pm 0.1\mu\text{m}$ for $f/1$ experiments.

At kilohertz repetition rates, the plasma deposition from the interaction is sufficiently high that only a few minutes of shooting can be performed before the energy deposited is reduced

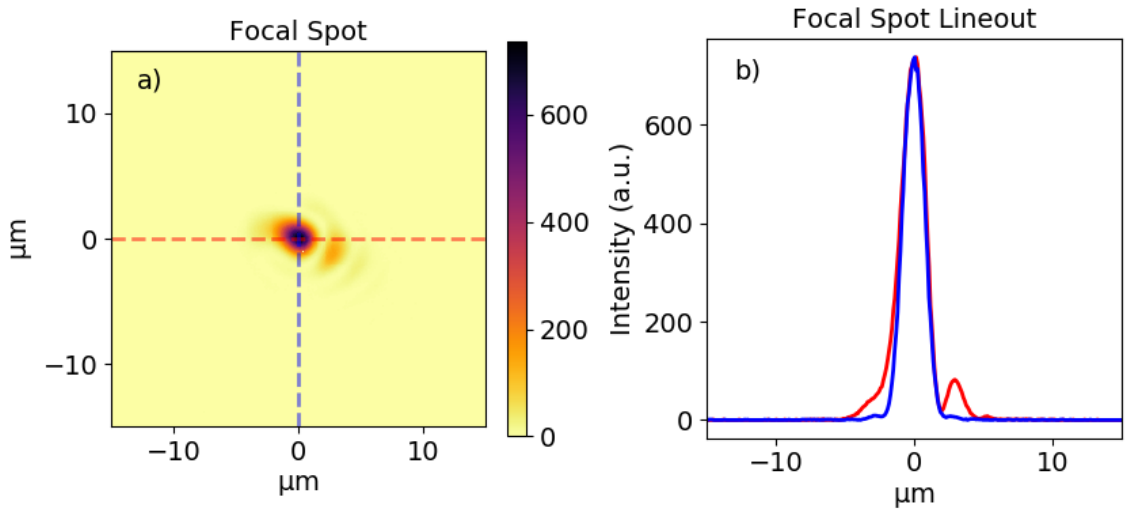

Figure 3.6: Measured *in situ* laser focus during laser-solid experiment.

by a factor of two. Therefore, Mylar pellicles are placed in between the focusing optic and solid target to protect the optic during shooting. When glass targets are used, the deposition rate on the Mylar is low enough that a single pellicle can be used for multiple targets. A silicon target produces significantly higher deposition, and therefore the Mylar needs replacement at much higher rates to prevent a popping of the pellicle due to increased laser absorption.

3.3 Radiation Diagnostics

Relativistic laser-solid interactions generate a variety of radiation, including optical light, higher-order harmonics, relativistic electrons, and hard x-rays associated with atomic emission and bremsstrahlung. In order to gain a better understanding of the laser-plasma interaction, it is important to field multiple diagnostics that measure some or all of these radiation sources during an experiment. The details of the optical diagnostics used to characterize the optical harmonics are discussed in Chapter 4. One common method for detecting hot electrons is through a scintillating screen paired with a dipole magnet. For experiments

conducted at UCI and ALEPH, permanent dipole magnets were fielded, the details of which are discussed in [108].

The following section focuses on the details and design of the crystal x-ray diagnostics fielded at Colorado State University for a LaserNetUS experiment. The experiment focused on measuring the characteristic x-ray emission generated from solid-density plasmas of copper targets. The x-ray spectrometers fielded are comprised of bent crystals which combine the focusing properties of a spherical mirror with the diffraction properties of a grating. These bent crystals can therefore image along one axis and spectrally disperse along the other axis with high spatial and spectral resolution.

3.4 X-ray Diagnostics

When an electron that is in a higher atomic energy level transitions to a lower energy state the energy difference is emitted as an energetic photon, whose wavelength is characteristic to the element. The characteristic wavelengths correspond to the energy differences between the energy shells of the atom. These characteristic transition lines can span from below one to thousands of eV. For example, the $n = 2$ to $n = 1$ atomic transition in copper, known as Cu Kα has a photon energy of 8.04 keV or a wavelength of 1.5406Å.

Spectroscopic analysis of x-rays requires spectrally dispersing the x-ray source onto a detector. At short wavelengths, mirrors and diffraction gratings do not work well[1]. For x-ray radiation the complex index of refraction n^*, deviates only slightly from unity and is given by:

$$n^* = 1 - \delta + i\beta, \tag{3.2}$$

[1]This is perhaps an understatement.

where δ represents the small deviation from unity, and β represents the attenuation of the x-ray radiation through material. For example, a commonly used material for optical mirrors is gold. The values of δ for gold are $\delta \approx 0.17$ at 50 eV, and quickly drops to $\delta \approx 0.005$ at 500 eV[2]. From Snell's law, the angle of incidence, θ_i, is related to the angle of reflection, θ_r, by:

$$\cos\theta_i = n\cos\theta_r. \tag{3.3}$$

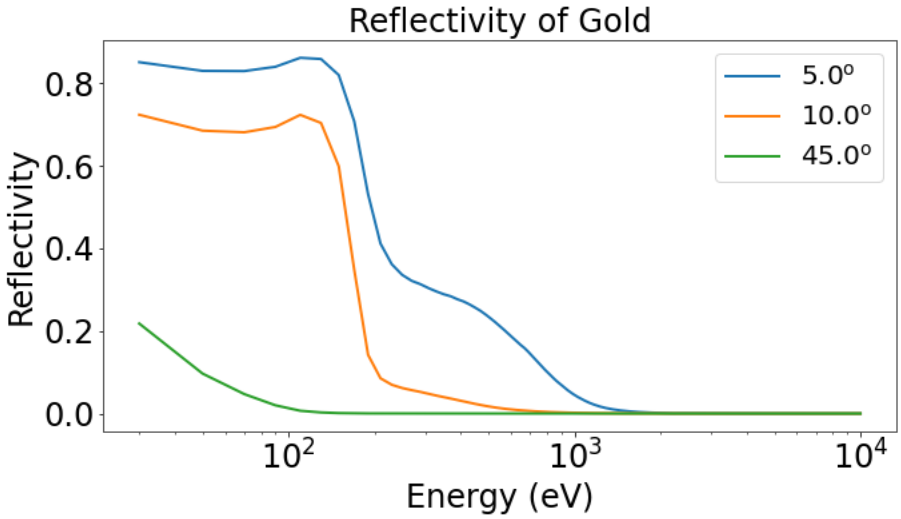

Figure 3.7: Reflection from a solid gold mirror for three angles of incidence. As the angle of incidence becomes closer to grazing, the mirror becomes more efficienct at higher energies. Note, that by photon energies of 10 keV the reflectivity is nearly zero for all cases. Values obtained from the Center for X-ray Optics X-ray database [5]

Total external reflection, i.e. the maximum angle of incidence such that reflection can occur $\cos\theta_r = 1$. The angle of incidence is given by $\theta_i \leq \theta_c$, where θ_c is the total external reflection angle. The limiting condition for external reflection is given by $\cos\theta_c = n$. By assuming that this angle occurs for small values of θ_c, the expression can be Taylor expanded such that

$$\cos\theta_c \approx 1 - \frac{\theta_c^2}{2} = 1 - \delta. \tag{3.4}$$

Therefore, the critical angle is given by $\theta_c = \sqrt{2\delta}$. As a result, the reflectivity of all materials

[2]Values obtained from the Center for X-ray Optics X-ray database [5]

become close to zero at energies higher than 100 eV for large angles of incidence. For gold at 50 eV, the critical angle $\theta_c \approx 33°$, and $\theta_c \approx 5.7°$ at 500 eV. As the angle of incidence becomes closer to grazing incidence, the reflectivity is maintained up to much higher energies, but the efficiency remains low. A plot of reflectivity of a gold mirror at different angles of incidence is shown in Figure 3.7. For soft x-ray sources such as those generated through high harmonic generation, the use of a grazing incidence diffraction grating is sufficient for spectral analysis. However, higher energy photons require another technique which is enabled through the constructive interference generated from Bragg's law from a crystalline structure.

3.4.1 Bragg Diffraction Crystals

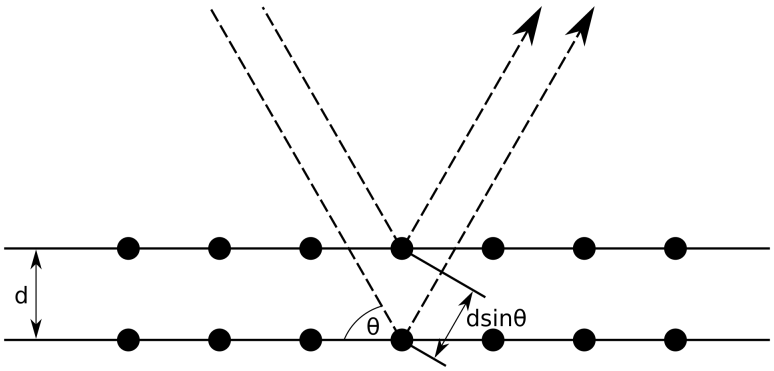

Figure 3.8: Bragg diffraction from a crystalline solid. Image credit: Wikipedia

When electromagnetic radiation is incident on an atom, it causes the electrons to begin oscillating. The oscillation of these charges re-radiates the light through Rayleigh scattering. The re-emitted fields interfere through constructive and destructive interference producing a diffraction pattern in the far field. This phenomenon is observable in thin film reflections, dielectric laser mirrors, and electron diffraction. Bragg diffraction occurs when the radiation has a wavelength comparable to the atomic spacing of a crystal is diffracted and constructively interfere. A crystalline solid can be modeled as having lattice planes separated by a distance, d. Constructive interference occurs when the path difference between the two

scattering planes, $2d\sin\theta$, equals an integer multiple of the wavelength, λ,

$$2d\sin\theta = n\lambda. \tag{3.5}$$

For single crystals, this effect occurs over multiple planes of the crystal, which intensifies the constructive and destructive interference from the scattering. The points where the scattering angles satisfy the Bragg condition (Equation 3.5) are known as Bragg peaks. The wavelength of X-rays (1-100Å) is typically the same order of magnitude as the spacing between planes of a crystalline material, so Bragg crystals are ideal for X-ray optics applications.

3.4.2 Spherical Crystal Imagers

We can use the property of Bragg diffraction to image high energy x-rays as a diagnostic of high energy density physics. The presence of Kα emission can be indicative of hot electron transport: electrons which have sufficient energy to create K-shell, $n = 1$, vacancies allowing for $n = 2 \rightarrow n = 1$ transitions [109]. We can image a narrow band of x-ray emission around the Kα lines using a spherically-bent Bragg crystal imager [110–112].

The imaging properties of a spherically-bent crystal are analogous to imaging off-axis with a spherical mirror; an additional constraint is imposed requiring the angle of incidence of the x-ray source satisfy the Bragg condition $2d\sin\theta = n\lambda$. In order to minimize the astigmatism introduced from spherical aberrations, the angle of incidence must be near normal, which restricts the operating wavelengths of crystals to a narrow range of wavelengths $\lambda \leq 2d$. Spherically-bent imagers have a specific radius of curvature, R. If an x-ray source and the crystal are placed on a circle whose diameter is half of the radius of curvature, all wavelengths will be focused along the circumference of the circle, known as the Rowland circle.

The behavior of incident and reflected rays occur in two orthogonal planes: the sagittal

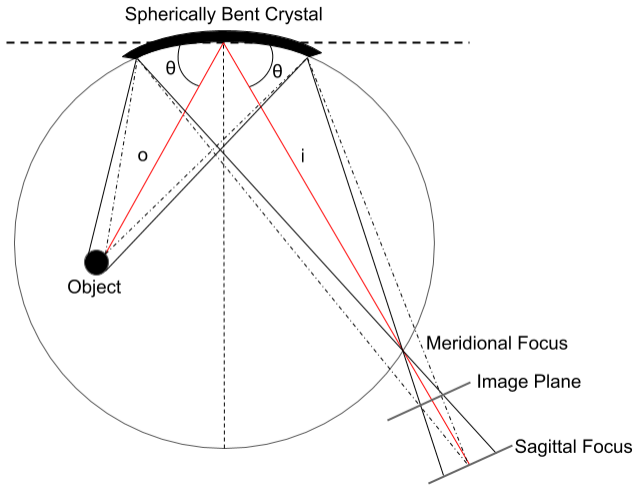

Figure 3.9: Layout of a spherically-bent crystal used as an imager. A detector placed between the meridonal and sagittal focal planes will produce an approximately round point spread function.

and meridional planes. The meridional plane contains the incident, reflected rays, and the Rowland circle for a single photon energy, while the sagittal plane is orthogonal to the meridional plane. In both planes, geometric focusing occurs, which results in a high resolution image. Astigmatism produced from a spherical mirror results in two focal planes, the meridional and sagittal plane i_m and i_s (Figure 3.9). If the source is placed within the Rowland circle at a distance o from the crystal, where o must satisfy $R\sin\theta > o > \frac{R}{2}\sin\theta$, we can use the thin lens equation for a spherical mirror to determine i_m and i_s:

$$\frac{1}{o} + \frac{1}{i_m} = \frac{2}{R\sin\theta} \tag{3.6}$$

$$\frac{1}{o} + \frac{1}{i_s} = \frac{2\sin\theta}{R} \tag{3.7}$$

where R is the radius of curvature of the crystal and θ is the Bragg angle [113]. The respective meridional and sagittal image planes are

$$i_m = \frac{oR\sin\theta}{2o - R\sin\theta} \tag{3.8}$$

$$i_s = \frac{oR}{2o\sin\theta - R}. \tag{3.9}$$

Placing the detector at image plane $i = oR/(2o - R)$, approximately midway between i_m and i_s, so as to produce a round point-spread function [111].

Spatial Resolution

The effective spatial resolution depends on a combination of crystal quality, source size, and detector. However, since the optics of a Bragg spherical crystal is analogous to imaging off-axis with a spherical mirror, largest contributor to image resolution is astigmatism, which is linked to the Bragg angle [110]. The astigmatism-limited object spatial resolution is given by

$$\sigma = \frac{D(M+1)}{M}(1 - \sin\theta_B). \tag{3.10}$$

For a pinhole with $D = 2.2$ mm, $M = 10$, and $\theta_B = 88.7^o$ the spatial resolution is $\sigma = 0.283\,\mu$m. For $D = 8.8$ mm, $\sigma = 2.5\,\mu$m. If the resolution of the detector is $25 \times 25\,\mu\text{m}^2$, an image which would be $25 \times 25\,\mu\text{m}^2$ on the detector should come from an area of $2.5 \times 2.5\,\mu\text{m}^2$ in the object plane. This means that any pinhole smaller than 8.8mm would not improve the image resolution.

Spectral Resolution

Much like how the spatial resolution determines the smallest spatial features resolvable in an imaging system, the spectral resolution of a spectrometer is a measure of its ability to resolve features in the electromagnetic spectrum. The spectral resolution is usually defined in terms of wavelength ($\Delta\lambda$) or energy (ΔE). The spectral resolution is closely related to the resolving power of a spectrometer, R, defined as

$$R = \frac{\lambda}{\Delta\lambda} = \frac{E}{\Delta E}, \tag{3.11}$$

where $\Delta\lambda$ is the spectral resolution at the wavelength λ.

For a crystal that satisfies the Bragg condition from Equation 3.5, the resolving power R of a spectrometer at Bragg angle θ can be found by taking the derivative of the Bragg equation

$$\frac{d\lambda}{d\theta} = \frac{2d}{n}\cos\theta = \frac{\Delta\lambda}{\Delta\theta} \tag{3.12}$$

and then solving for $\lambda/\Delta\lambda$

$$\frac{\lambda}{\Delta\lambda} = \frac{1}{\Delta\theta}\tan\theta \tag{3.13}$$

where $\Delta\theta$ is the angular resolution of the detector determined by the spatial resolution of the detector and its distance from the crystal [114]. For image plate with a spatial resolution of ≈ 25 μm [115] at a distance of 825 cm from the crystal with Bragg angle of 88.7° the resolving power is 3.5×10^6, or $\Delta\lambda = 4.30 \times 10^{-7}$Å at the Cu K$\alpha$ line.

3.4.3 High Resolution Spectrometers

The previous crystal imager setup is designed to collect and image a narrow energy band centered around an atomic emission line. However, if we remove the restriction of being near normal incidence, we can also utilize spherical Bragg crystals for spectroscopy. Because x-ray focusing occurs in both the meridional and sagittal planes of a spherical crystal, higher image brightness is possible compared to single plane focusing like von Hamos spectrometers. Dispersion of different x-ray energies occurs in the meridional plane due to the variation of the incident angles required to satisfy Bragg's law over the crystal surface (see Figure 3.10). Placing the detector at either the meridional or sagittal focus would provide spatial resolution. However, the sagittal focus yields the best spatial resolution, because there is no

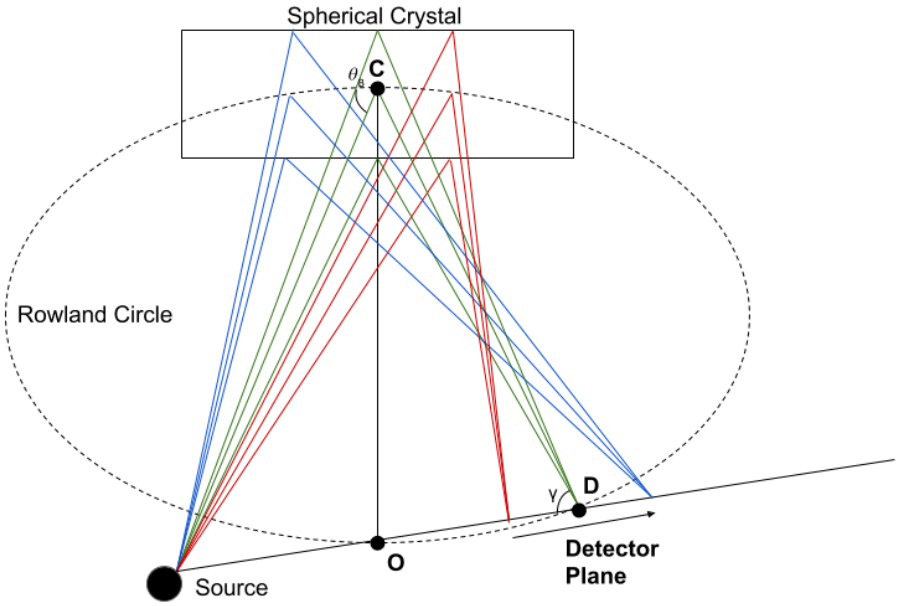

Figure 3.10: A spherically-bent crystal oriented to achieve high spectral resolution along the dispersion plane.

energy dispersion in the sagittal plane to cause image blurring. At the sagittal focus, the reflected rays are focused onto a line that connects the source (point **S**) and the center of the crystal curvature on the Rowland circle (point **O**).

Spectral Dispersion

In order to use the spherical crystal as a spectrometer, the energy dispersion of the system needs to be calculated [116, 117]. In this analysis, a point source is assumed and only the dispersion around the central ray is determined. In the sagittal plane, the central ray from the source follows path (**SCD**) from the source to the detector plane as seen in Figure 3.11. The positions of the source, crystal, and detector are determined by the thin lens equation for the sagittal focal length(Equation 3.7). In the dispersion plane, the x-ray source is placed at a distance p from the center of the crystal surface (**C**) at an angle of incidence ϕ (with respect to surface normal), corresponding to the Bragg angle $\theta_B = \pi/2 - \phi$ for wavelength λ.

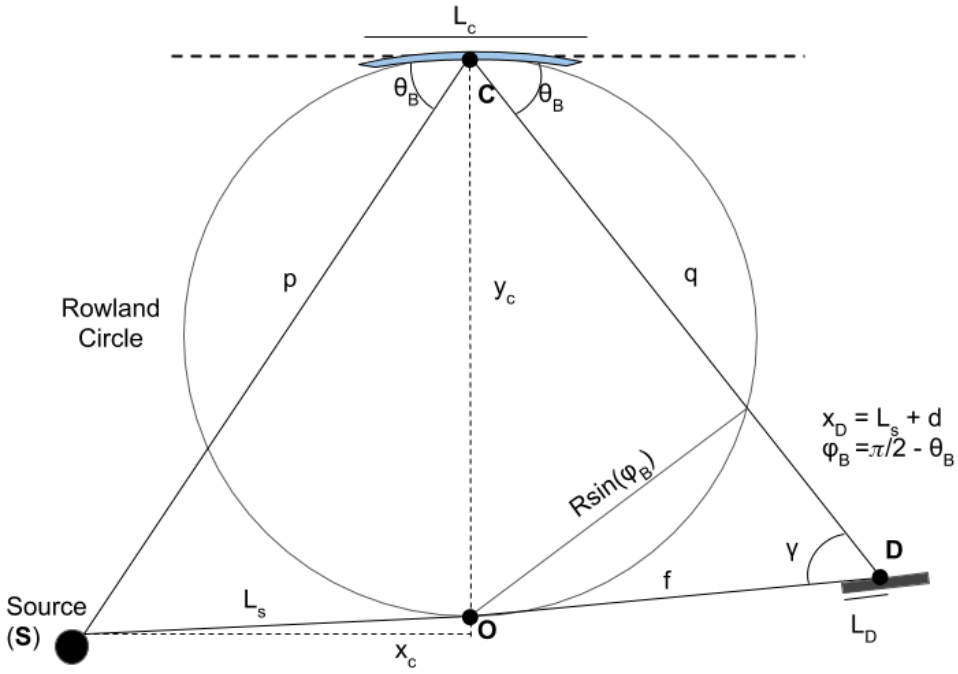

Figure 3.11: Geometric diagram of high-resolution spherical crystal spectrometer.

The position of the spectral line relative to the center of the sphere (point **O**) is given by

$$f = \frac{R \sin \phi}{\sin \gamma} \tag{3.14}$$

where R is the crystal radius of curvature. γ is the angle between the center of the emission source to the detector and the reflected ray given by

$$\gamma = \pi - 2\phi - \sin^{-1} \frac{R \sin \phi}{L_s} \tag{3.15}$$

where $L_s = \sqrt{R^2 + p^2 - 2Rp \cos \phi}$ is the distance from the source to point **O**. Calculating the dispersion D along the detector involves determining the variation of f with respect to the angle ϕ while holding L_s constant

$$D[\text{mm/eV}] = (\frac{df}{dE})_{L_s} = (\frac{df}{d\phi}\frac{d\phi}{dE})_{L_s}. \tag{3.16}$$

The second term $d\phi/dE$ can be found using the Bragg equation in terms of energy and ϕ:

$$n\lambda = 2d\sin\theta_B \tag{3.17}$$

$$\frac{nhc}{E} = 2d\sin\theta_B \tag{3.18}$$

$$E = \frac{nhc}{2d\cos\phi}. \tag{3.19}$$

Then by taking the derivative:

$$\frac{dE}{d\phi}[\text{eV}] = \frac{nhc}{(2d)}\frac{\tan\phi}{\cos\phi} \tag{3.20}$$

where $hc = 12.398$ÅkeV is the product of the speed of light and Planck's constant, 2d is twice the atomic spacing in units of Å, and n is the diffraction order. We can calculate the derivative of f by using Equation 3.14:

$$(\frac{df}{d\phi})_{L_s} = \frac{R}{\sin\gamma}[\cos\phi - \sin\phi\cot\gamma(\frac{d\gamma}{d\phi})_{L_s}]. \tag{3.21}$$

Then, by taking the derivative of Equation 3.15

$$(\frac{d\gamma}{d\phi})_{L_s} = -\frac{R\cos\phi}{\sqrt{L_s^2 - R^2\sin^2\phi}} - 2. \tag{3.22}$$

The spectral range of the crystal can be calculated by determining how the local angle of crystal changes with varying angle of incidence. For a point (**P**) on the crystal off-center, that makes an angle α between **PO** and **OC**, the local incidence angle is given by

$$\phi(\alpha) = \frac{\pi}{2} - \theta_B - (\frac{p - R\sin\theta_B}{p})\alpha. \tag{3.23}$$

The spectral range (ΔE) is then given by

$$\Delta E = \frac{nhc}{2d}[\frac{1}{\cos\phi_{\max}} - \frac{1}{\cos\phi_{\min}}], \tag{3.24}$$

where $\phi_{\min}$ and $\phi_{\max}$ are the incident angles at the edges of the crystal. A Python code was written to calculate the spectral range and dispersion of two Ge-220 Bragg crystals designed to operate in the range of the Cu K-shell, i.e 8-9 keV.

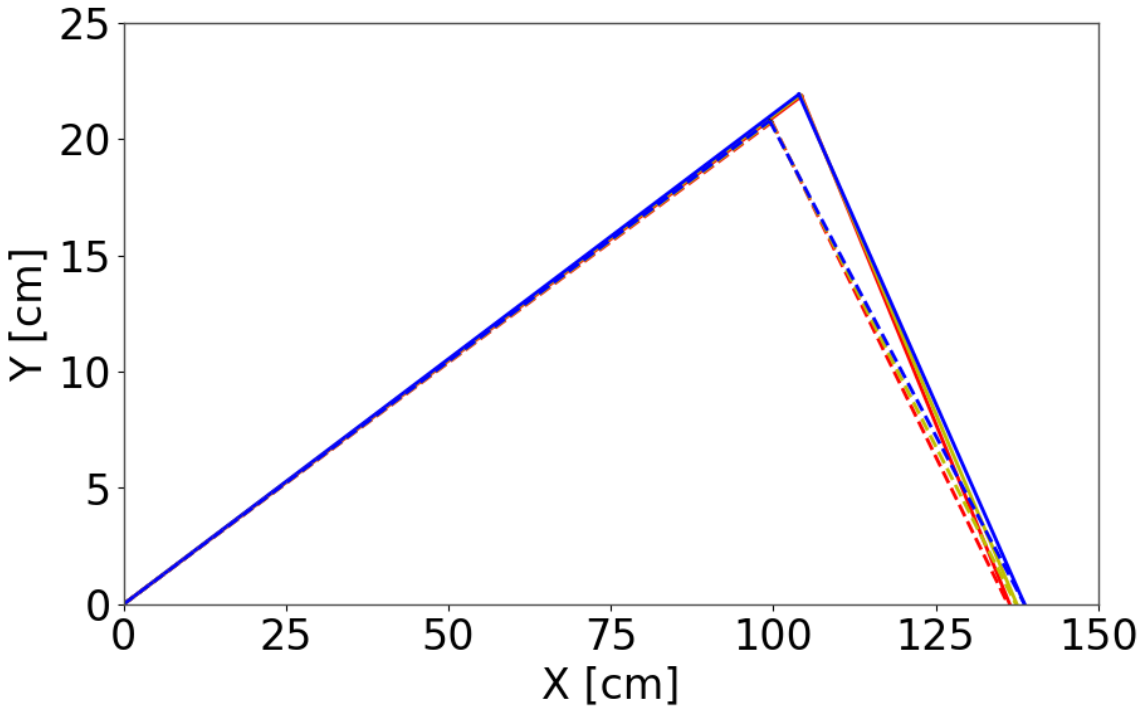

Figure 3.12: Ray tracing calculations of the Kα (solid lines) and Kβ (dashed lines) spectral ranges.

The geometry of the ray tracing code is as follows. A point-source object is located at the origin. The two crystals are initialized in space such that their individual object distances, reflection angles, and image distances result in the image plane forming on the x-axis. The position of the object and image are chosen such that the direct line between them is along the horizontal axis. Due to the different radii of curvature and spectral ranges, the crystals need to sit at different x,y coordinates, and have different tilts with respect to the horizontal axis.

3.5 Particle-in-cell Simulations

High-intensity, laser-plasma interactions involve $> 10^{21}$ particles that move relativistically according to the electromagnetic fields of the laser and plasma. A complete, microscopic, many-body simulation or theoretical calculation is simply not possible. However, numerical modeling is a powerful tool for both designing experimental campaigns and elucidating the results. One popular algorithm is known as the particle-in-cell (PIC) simulation. Instead of solving for the phase space of 10^{21} particles, which is a typical number of electrons found in solid density interactions, PIC codes organize particles into "macro-particles." Density and current values are averaged over many particles and are mapped onto a simulation grid which is used to calculate the electromagnetic fields inside of the simulation window. Once calculated, the macro-particles are pushed at each time step by the summation of forces in accordance with the Lorentz force law.

In conjunction with experiments, 1D and 2D particle-in-cell (PIC) simulations were carried out to investigate the physics of the high-intensity interactions. The simulations were performed using the fully-relativistic, particle-in-cell code OSIRIS 4.0 [118]. OSIRIS is a nD3V (where n=1,2,3) PIC-solver which self-consistently solves Maxwell's equations describing the interaction between electromagnetic radiation and plasma. The number of spatial dimensions chosen restricts particle movement, but at each time step the full 3D momenta and fields are solved. This enables vectorial forces such as the magnetic component of the Lorentz force ($\mathbf{v} \times \mathbf{B}$) to impact 1D3V simulation runs.

3.5.1 Equation Normalization

OSIRIS is one of many PIC codes that uses a normalized system of units. From a computational perspective it is convenient to convert everything to a normalized units scheme

such that the physics of the simulation is a scalable phenomenon. This allows us to ignore physical constants of widely varying numerical values (e.g. m_e, e and c) thereby allowing computational simulations to run without carrying around large floating point precision. For example, the normalized vector potential, a_0, is a normalized quantity for the electric field amplitude. At field strengths $a_0 \sim 1$ the interaction is defined to be relativistic, regardless of the driving laser frequency. Since we are interested in laser-matter interactions, we can choose a convenient normalization scheme in terms of fundamental laser parameters.

The real components of a laser pulse linearly polarized in $\hat{x}$ and propagating in $\hat{z}$ as described above in Equations 2.28 and 2.29, can be written as:

$$\mathbf{E}_{wave} = E_0 \cos(\xi)\ \hat{x} \tag{3.25}$$

$$\mathbf{B}_{wave} = B_0 \cos(\xi)\ \hat{y} \tag{3.26}$$

where $\xi = \omega_0(t - x/v_{ph})$, v_{ph} is the phase velocity, $\omega_0 = 2\pi c/\lambda_0$ is the laser frequency and $B_0 = \frac{c}{v_{ph}} E_0$. In vacuum $v_{ph} = c$, the magnitude of the electric and magnetic fields are equal. We can now choose to normalize our equations of motion to dimensionless quantities in terms of the characteristic particle and laser field values:

Physical Quantity	Normalization
Time	$t' = \omega_0 t$
Frequency	$\omega' = \omega/\omega_0$
Position	$\mathbf{x}' = k_0 \mathbf{x}$
Momenta	$\mathbf{p}' = \mathbf{p}/m_e c$
Electric Field	$\mathbf{E}' = e\mathbf{E}/m_e \omega_0 c$
Magnetic Field	$\mathbf{B}' = e\mathbf{B}/m_e \omega_0 c$

Table 3.1: Summary of normalized parameters defined in the OSIRIS PIC simulations.

The associated normalized equations of motion:

$$\boxed{\begin{aligned} \frac{d\mathbf{p}}{dt} &= -\mathbf{E} - [\mathbf{v} \times \mathbf{B}] && (3.27)\\ \frac{d\mathbf{x}}{dt} &= \frac{1}{\gamma}\mathbf{p} && (3.28)\\ \frac{d\gamma}{dt} &= \quad -\mathbf{v} \cdot \mathbf{E}. && (3.29) \end{aligned}}$$

Note: the magnitudes of the electric and magnetic fields, E_0 and B_0 from Equations 2.28 and 2.29, are now equal to the normalized vector potential, a_0. The equations of motions are in general coupled, nonlinear differential equations that require numerical solutions.

Chapter 4

Mid-infrared Relativistic High Harmonic Generation

This chapter is adapted, with permission, from: N. Beier et al., 2019 New J. Phys. 21 043052 [6]. In this chapter, the experimental investigation of relativistic laser-solid interactions driven by 1300nm and 2100nm ultrafast pulses is presented. Nearly all investigations of relativistic high harmonic generation have taken place using NIR drivers at 800nm or 1053nm. In this study, we investigated the scaling of relativistic harmonic generation at the threshold of the relativistic regime, $a_0 \sim 1$. The advantage of using longer wavelength drivers is that higher order harmonics, namely $4\omega_0$ and greater, which are exclusively generated through the high intensity interaction lie within the optical spectrum. This enables us to capture and study the harmonic emission using traditional optical techniques. The experiments were carried out with a variety of laser and plasma parameters to determine the optimal conditions available during the experiment. The complete capture of harmonic emission enables more accurate discrimination of mechanisms present with validation through particle-in-cell simulations. Experiments were performed at two facilities through OPA driven by CPA-based Ti:Sapphire ($\lambda_0 = 800$nm) lasers: the University of California, Irvine and the

Relativistic Lambda-Cubed Laser at the Gérard Mourou Center for Ultrafast Optical Science, University of Michigan.

4.1 Lambda Cubed 2100nm Experimental Setup

During the experimental run in question the Lambda Cubed laser routinely output 16 mJ of compressed pulse light. The experiment at CUOS was performed after down-converting the laser light to 1.6 mJ of $\lambda_0 = 2.1\,\mu$m through a two-stage, custom-built OPA. The output polarization of the 2.1μm light from the OPA was controlled with a half waveplate to select s- and p-polarized driving of the laser-plasma interaction. Residual lower wavelength light from the OPA process was filtered using a 1.65μm longpass filter (Andover 1.65ILP-25). After filtering, the pulse duration increased from $\tau_0 = 67$fs to $\tau_0 = 100$fs temporal FWHM measured via autocorrelation due to dispersion through the filter. The MIR beam was then directed through a silver-coated reflective telescope to up-collimate to a 50mm beam diameter. Prior to entering the experimental chamber the wavefront is corrected by a 47mm diameter deformable mirror with 37 actuators (Xinetics). The beam was sent into a vacuum chamber through an uncoated fused silica window at normal incidence. A gold-coated, fast-focusing, off-axis parabolic (OAP) mirror (f/1.3) focused the beam onto the target at angle of incidence near 45° producing a maximum focal intensity of 8.7×10^{16} W/cm^2, $a_0 = 0.5$. While the beam profile could not be measured directly due to a lack of MIR detectors, the 2μm focal spot was optimized through a genetic algorithm measuring the second harmonic produced from plasma formation in low level atmosphere, $\sim$ 1 Torr [29]. Silicon wafers and fused silica glass targets were mounted on an automated spindle to keep the target within the Rayleigh range of the laser focus and to continually refresh the target during the experiment at high repetition rate. A dial indicator with ±2μm accuracy was used during target alignment to ensure target flatness within the Rayleigh range $\sim$ 10μm. The different targets were

selected due to their difference in damage threshold and resulting plasma scale lengths. The vacuum chambers were evacuated to below 10 mTorr levels to avoid plasma formation before the target surface and to allow UV propagation from the target to the diagnostics. *In situ* control of the target focal positioning was performed to maximize harmonic intensities.

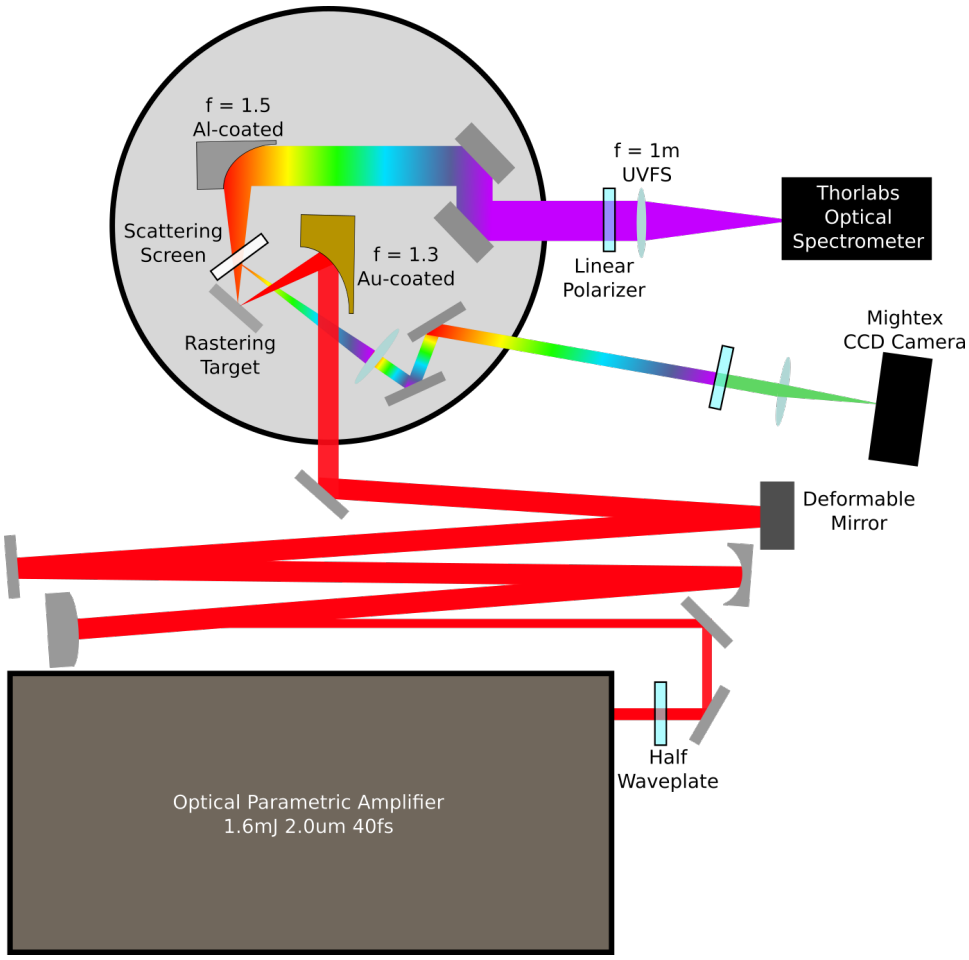

Figure 4.1: Experimental Setup at Lambda-cubed.

Two separate diagnostics were used to measure the harmonic polarization and divergence at CUOS. For polarization measurements, the harmonics generated from the interaction were collected using an aluminum OAP (f/1.5), directed out of the chamber, and focused with a UV fused silica lens (f = 1000 mm) into an optical spectrometer (Thorlabs CCS200). The harmonics passed through a Zinc Calcite polarizer to control polarization-dependent throughput. For divergence measurements, a diffusing screen was placed 2 cm in the specular direction from the target to intercept the harmonics. Two fused silica lenses (f = 1000 mm

and f = 150 mm) imaged the screen onto a charge-coupled device camera (Mightex CGE-B013-U) enabling the measurement of the harmonic near field. Bandpass filters (Edmund Optics S/N 65-694, 65-717, and 65-741) were used to isolate each harmonic separately. Each bandpass filter was selected to center on the harmonic of choice for 2μm with a FWHM window of 10nm, e.g. the 4th harmonic was imaged using a bandpass filter at 500 ± 5nm. The 5th harmonic bandpass filter had a 50nm FWHM; however, only broadband plasma recombination emission was detected during the divergence measurements at that harmonic. Divergence measurements are integrated from 5 - 500 shots. Shot to shot fluctuations of $\sim 15\%$ intensity were present in the divergence measurements due to stage instability.

4.1.1 UCI 1300nm Experimental Setup

The experiments at UCI were similar to those performed at CUOS. The output polarization from the OPA was controlled with a silver-coated reflective periscope system and passed through a 1.0μm longpass filter (Thorlabs FGL1000). After filtering, the pulse remained near the transform limit of $\tau_0 = 35$fs measured via second harmonic generation frequency resolved optical gating (SHG FROG). A deformable mirror was not used to correct the wavefront prior to entering the vacuum chamber through an anti-reflection coated fused silica window. A two-inch diameter, gold-coated OAP (f/1) focused the beam onto the target at angle of incidence near 45^o producing a maximum focal intensity of 5×10^{17} W/cm^2, $a_0 = 0.78$. Silicon wafers and silica glass targets were mounted on an automated translation stage for high repetition rates and *in situ* control of target positioning. For experiments at UCI, the laser repetition rate was reduced to 250Hz to prevent focal spot overlap from consecutive shots (see Fig 4.2 for examples of focal spot overlap).

Similar to the experiment at CUOS, the harmonics generated from the interaction at UCI were collected using an aluminum-coated OAP (f/4), directed out of the chamber, and fo-

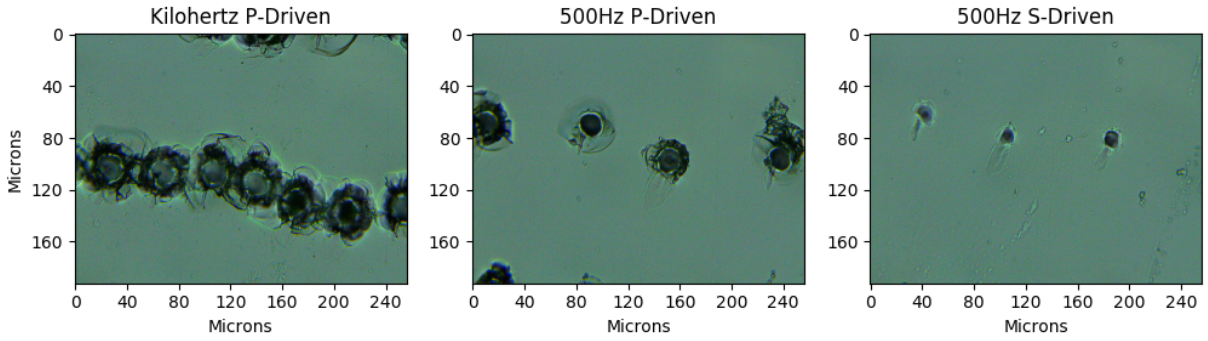

Figure 4.2: Example of soda lime glass target damage after 1300nm interaction. a) Focal spot overlap present when running laser system at 1kHz repetition rate. b) Focal spots no longer overlap when running system at 0.5kHz. c) Apparent damage decreases when driving wavelength is S-polarized due to weaker absorption.

cused with a UV grade fused silica lens (f = 350 mm) into an optical spectrometer (Ocean Optics Flame-S). The signal was integrated over five shots to produce the measured spectrum. Harmonic polarization was measured by inserting a linear polarizer in front of the spectrometer. The polarizer was on a BK-7 substrate which removed all signal beyond the 4th harmonic due to its poor transmission of UV light. No divergence measurements were taken at UCI. This is because the harmonics of interest, namely $4\omega_0$ and above, that are exclusively generated through the high-intensity interaction lie within the near ultraviolet. Unfortunately, we did not have access to bandpass filters which transmit in this spectral region.

In summary, the experiments discussed in this chapter comprised the investigation of mid-infrared laser-solid interactions at the edge of the relativistic regime with parameters listed in Table 4.1. The targets used were bulk silicon and silica mounted on motion controlled stages to enable high repetition rates. The reflected harmonic emission was collected for analysis through spectral and divergence diagnostics in the optical region of the electromagnetic spectrum.

Wavelength (μm)	1.3	2.1
Energy (mJ)	0.6	1.2
Pulse Duration (fs)	35	100
Peak Intensity (W/cm^2)	5×10^{17}	8.7×10^{16}
Normalized Vector Potential (a_0)	0.78	0.5

Table 4.1: Summary of laser parameters used during experimental study.

4.2 Optical Harmonic Wavelength Scaling

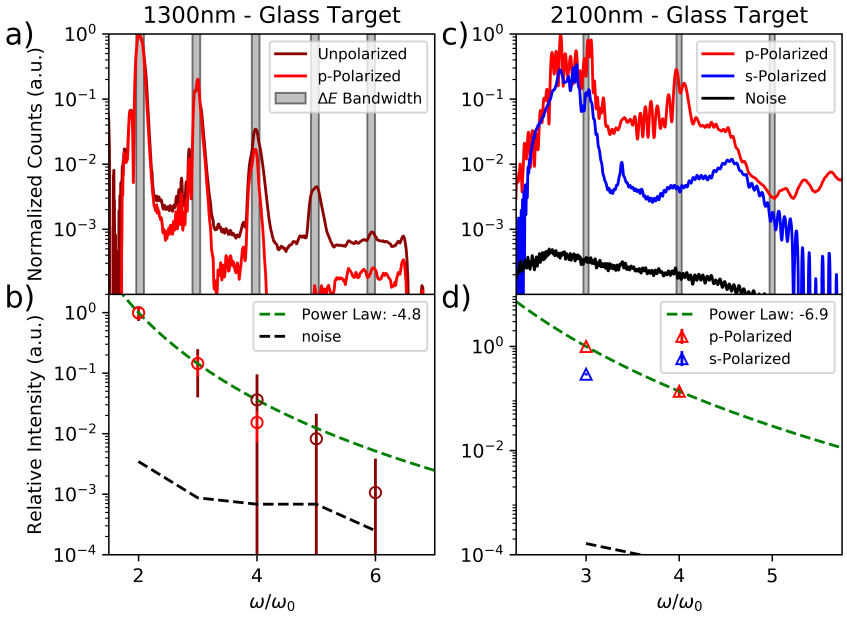

Figure 4.3: 1.3μm and 2μm harmonics from a silica target. a) Unpolarized (dark red) and p-polarized (red) emission spectra from p-polarized 1.3μm interaction. Initial pulse energy bandwidths centered on the peak of each harmonic shown in gray. b) Corresponding harmonic intensity values: (circles) experiment, (green dashed line) best fit line. c) Emission spectra of p-polarized (red) and s-polarized (blue) harmonics from 2μm interaction. d) Corresponding harmonic intensity values: (triangles) experiment, (green dashed line) best fit line. [6]

The captured optical order harmonics of the 1.3μm and 2μm interactions with silica targets can be seen in Figure 4.3. Each spectrometer exposure integrates between five and ten shots at a time. Continuous motion of the targets while collecting spectra enables each successive pulse to interact with fresh target. The spectra are then corrected for the optical response of the optics, vacuum windows, and spectrometer efficiency. Relative intensities are calculated by integrating each harmonic over their full-width at half-maximum (FWHM)

bandwidths. Figure 4.3 a) shows the efficiency-corrected harmonic spectra from a p-polarized 1.3μm interaction with soda lime glass with (dark red) and without (red) a linear polarizer inserted to transmit only p-polarized light. The apparent lack of polarized harmonics beyond $4\omega_0$ (325nm) is due to the poor transmission of ultraviolet light through BK-7 glass inside the polarization optic. There was no detectable s-polarized harmonic signal from the p-polarized incident which was significantly above the noise. Harmonics from an s-polarized 1.3μm interaction were never observed.

The normalized individual harmonic intensity values are shown in Figure 4.3 b). Overlain is a power law fit (dashed green line) showing a relative intensity scaling of $I_n \propto n^{-p}$ where I_n is the intensity of the nth harmonic and $p = 4.8$. The choice of a power law fit is due to the well-known power law scaling of ROM HHG [103]. Figure 4.3 c) shows normalized spectra from s- and p-polarized 2μm interactions with a fused silica target. Note the significant structural differences between the 1.3μm and 2μm harmonics as well as the much larger energy FWHM than the transform limit of the incident 2μm laser (shown in gray). This is not the case with the 1.3μm harmonics which have much narrower bandwidths. There appear to be strong modulations in the third harmonic spectrum of the 2μm interaction, which would indicate multiple sources of harmonic emisison. Figure 4.3 d) shows the integrated intensity values for the 2μm interaction with a power law fit with $p = 6.9$. No detectable fifth harmonic or above were measured with silica targets at CUOS.

4.3 Polarization-Dependent Harmonic Generation

The polarization dependence of optical order harmonics generated with two separate target materials using a 2μm driver can be seen in Figure 4.4. S- and p-polarized harmonics from a silicon wafer are fused silica target are shown in Figures 4.4 a) and 4.4 b), respectively. The structure of the harmonics is significantly different between the two cases. In both

cases, there exists harmonic bandwidth beyond the initial energy bandwidth defined by the fundamental (shown in gray). The strong modulations from the silica targets, as noted above, were less apparent in the harmonics from the silicon wafers targets. There exists notable secondary, lower-energy peaks at $4\omega_0$ and $5\omega_0$ in the silicon target spectra. The integrated intensity measurements from the two targets can be compared in Figure 4.4 c). The silicon target has a shallower power law decay compared with the glass target. In addition, the fifth harmonic is resolved with a silicon wafer target but not during the fused silica interaction.

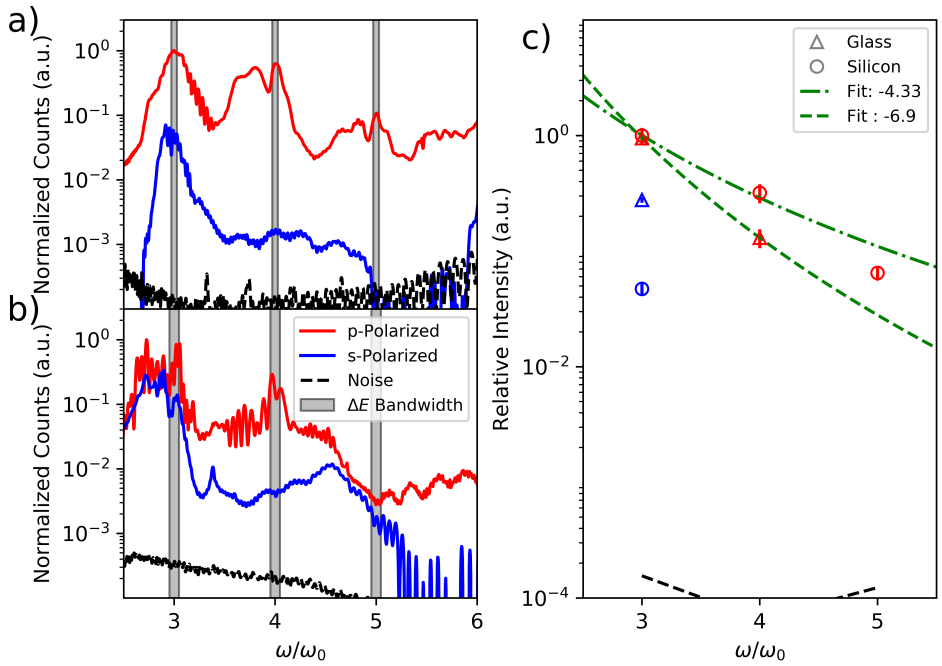

Figure 4.4: a) P-driven (red) and S-driven (blue) harmonics from silicon wafer targets. b) P-driven (red) and S-driven (blue) harmonics from fused silica targets. Significant structure seen outside of initial energy bandwidth (grey). c) Harmonic intensity values for silicon (circle) and glass (triangle) targets. [6]

4.4 Divergence Measurements

Finally, we are interested in the profile of the individual harmonics. The harmonic profiles and divergence measurements from p-polarized 2μm interactions can be seen in Figure 4.5. The red dashed circle corresponds to the divergence angle of the fundamental defined by the

f/1.3 focusing geometry. Since we could not image the fundamental, a HeNe laser collinear with the OPA beam was used to define the divergence angle. The light imaged from the diffusing screen through the bandpass filters contains structure for lower order harmonics. As seen in Figures 4.5 a), 4.5 b), and 4.5 c), it appears as though the low order harmonics are generated in beamlets, which are not along the specular direction. The image of glass 5th harmonic, Figure 4.5 d), is most likely diffuse plasma discharge from the target, which is consistent with $5\omega_0$ never being observed from glass targets.

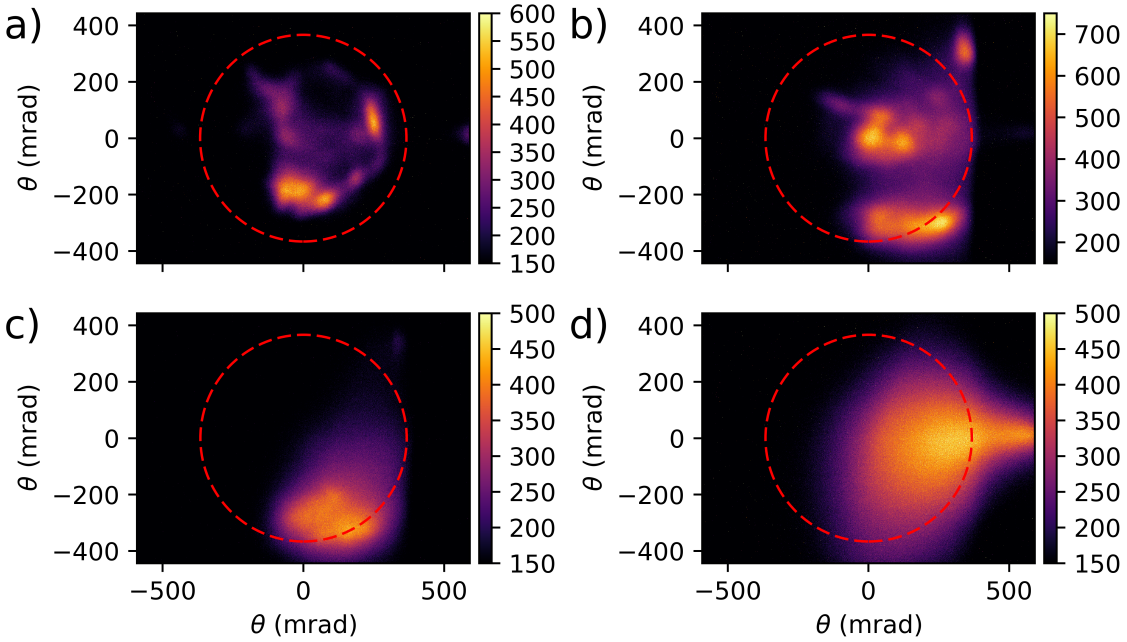

Figure 4.5: Divergence of 2µm driven harmonics imaged from diffuse reflector through bandpass filters. The fundamental divergence angle (dashed red) is overlain for convenience. a) $3\omega_0$ from silicon wafer target. b) $3\omega_0$ from fused silica target. c) $4\omega_0$ from fused silica target. d) $5\omega_0$ from fused silica target. [6]

4.5 Discussion of Experimental Results

From the ROM HHG selection rules (Table 2.1), we expect p-polarized odd and even harmonics from p-polarized interactions, while s-polarized interactions generate s-polarized odd and p-polarized even harmonics [23]. Figures 4.3 and 4.4 show that up to fifth order both

odd and even harmonics from p-polarized interactions are also p-polarized with s-polarized emission remaining at the noise level. It can be assumed that the observed 5th and 6th harmonics in Figure 4.3(a) would also follow this trend and could be confirmed using a polarizer that transmit UV light. It was possible to resolve the 3rd harmonic from the s-polarized interaction, and we can confirm that it is also s-polarized. The weaker signal of the S-polarized harmonics in Figures 4.4 a) and 4.4 b) is due to the inherently weaker coupling of s-polarized light into the plasma. If the experiments were conducted at higher intensities ($a_0 > 1$) then the s-polarized interaction would most likely produce emission above the 3rd harmonic. The theoretical ultra-relativistic ($a_0 \gg 1$) harmonic relative intensity scaling is given by p=8/3 [100]. While our experimentally measured intensity scaling did not match the theoretical prediction, our measured p-values ($4.33 < p < 6.9$) do lie between this limiting case and other experimental values of $5.2 < p < 10$ [88, 90, 104, 119] that vary between comparable and significantly higher intensities. Because the experiments were carried out near the threshold of the relativistic regime and not in the ultra-relativistic limit, it is unsurprising that the measured relative intensity decay is faster than the theoretical value.

The significant structural differences between the silicon and silica targets requires further consideration. The strong spectral modulations in the 2μm fused silica harmonics as seen in Figure 4.4 a) coupled with evidence of two separate beamlets in the 3rd harmonic, Figure 4.5 b), suggests multiple harmonic sources from fused silica targets which is lacking in the silicon wafer interaction. If we assume that the modulations are produced from an interference between two pulses we find something surprising. The modulations have a frequency spacing of 8THz which corresponds to a secondary harmonic pulse separated by a 125fs delay or by a source spatially separated by ~ 40μm. A pulse delay of 125fs is too short to be from either the next laser pulse (2ms) or any type of double pulsing of the oscillator which runs at MHz repetition rates, and 40μm is much larger than the laser focal spot, ~ 5μm. The source of these modulations is not immediately obvious.

Given this information, it is unclear whether the produced harmonics are from the coherent wake emission or relativistic harmonic generation mechanism. There are three main distinguishing features between CWE and ROM HHG. First, CWE has only been detected in p-polarized geometries. While the second and third harmonic can be produced from a multitude of mechanisms, the detection of the 4th and higher harmonics from an s-polarized interaction would be a strong indicator for ROM HHG [98]. Unfortunately, the interaction intensity wasn't such that the 4th harmonic could be resolved from s-polarized interactions. The second distinguishing feature between ROM and CWE in p-polarized interactions is the sharp cutoff for CWE HHG occurring at the plasma frequency, ω_p [98]. The cutoff contrasts with the universal ROM harmonic spectrum defined by a power law decay, $I_n = I_0\, n^{-p}$, up to some maximal cutoff frequency $\omega_0 = 4\gamma^2$, where $\gamma = \sqrt{1 + a_0^2}$ is the maximum electron relativistic factor at the critical surface [42,100]. For solid density targets the plasma frequency is tens of times greater than the laser frequency which lies well outside the visible spectrum. The third method compares the intensity dependence of the harmonics to determine the driving mechanism. The strong dependence of ROM on a_0 contrasts significantly with the weaker intensity scaling of CWE. This method requires the complete capture of harmonic spectra which is not necessarily possible with traditional experiments at 800nm, because x-ray spectrometers typically capture a very small solid angle of the emission. The measurement of the optical harmonics from midinfrared laser systems allows for the discrimination of ROM and CWE harmonics using traditional optical techniques.

The dependence of ROM HHG production on a_0, where slight variations in a_0 can dramatically alter the spectrum, is significantly stronger than for CWE. Notably, CWE has been detected down to intensities as low as $I\lambda^2 = 4 \times 10^{15}\,\mathrm{W/cm^2\mu m^2}$ or $a_0 \ll 1$ and has been shown to have harmonic conversion efficiencies that vary weakly with the incident laser intensity ($I_n \propto I_0^{0.4}$) [98]. The intensity dependence of the generated harmonics was measured by moving the automated target stages by less than two Rayleigh lengths from optimal focus. The resulting harmonic spectrum (blue) can be seen in Figure 4.6 a) with a direct comparison

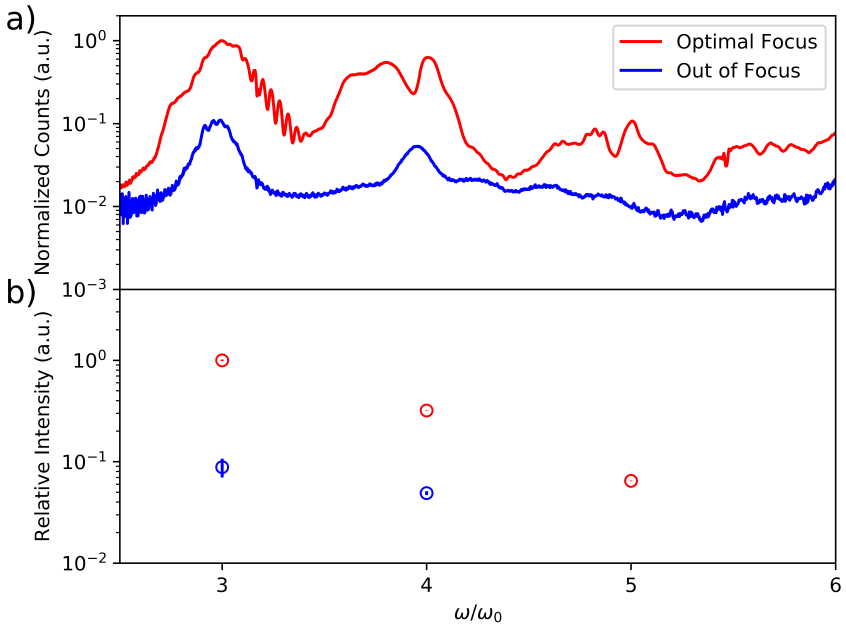

Figure 4.6: Stage motion effect on p-polarized harmonic intensity. Note the logarithmic scale of the y-axis. a) Harmonic spectra from silicon wafer target positioned at ideal focal position (red) versus positioned roughly two Rayleigh lengths out of focus (blue). Third and fourth harmonic are both clearly visible in both cases, however there is no fifth harmonic detected in the out of focus case. b) Relative harmonic intensity measurements. The significant drop in measured intensity values suggests a strong dependence on incident laser intensity for harmonic generation. [6]

of optimal focal position (red). The integrated harmonic intensities are shown in Figure 4.6 b). It should be noted that the relative intensity of the 3rd harmonic decreases by a factor of ten two Rayleigh lengths from optimal position. If we assume that the interaction is CWE dominant then relative harmonic intensity scales according to $I^{0.4}$. Therefore, the measured relative $3\omega_0$ intensity values would require the initial laser intensity to drop by a factor of 300. This corresponds to a motion of 18 Rayleigh lengths away from best focus, which is well outside of the measured range of the stage instability as measured by a dial indicator to be within a Rayleigh length during the experiment as described above. Coupling this with the consistent harmonic polarization selection rules suggests that the dominate mechanism in these interactions is from the ROM model.

4.6 2D Simulations with Experimental Parameters

Simulations were run using a $133.7 \times 133.7 \mu m^2$ square box with 5000×5000 cells resulting in a spatial resolution of $\lambda/87$. The spatial resolution was chosen to resolve lower-order harmonic frequencies. The number of macroparticles per cell was held fixed at 128 particles per cell across the simulation box. The solid-density plasma was initialized as a slab of electrons with plasma density $100n_c$ and thickness 534nm angled at 45^o with respect to the input laser. An exponential density ramp of the form $\exp(-x/L_s)$ was placed before the front surface of the target to represent the pre-plasma formed by the laser pre-pulse. The plasma scale length, L_s, was varied over a range $\lambda/10 \leq L_s \leq 10\lambda$ to determine effects of the pre-plasma on harmonic generation. In order to match the experimental conditions at CUOS the laser pulse had a central wavelength $\lambda_0 = 2.1 \mu m$, temporal FWHM duration $\tau_0 = 100fs$, and was p-polarized. The pulse was focused to a $2.5 \mu m$ FWHM Gaussian focal spot on the front surface of the target producing a normalized vector potential $a_0 = 1$. After the interaction, the light reflected away from the target into free space; there, the reflected light was analyzed using two-dimensional fast Fourier transforms (FFT) to determine the harmonic spectra and divergence. The validation of experimental results through simulation is extremely relevant to the recent experimental campaign as we have demonstrated the complete capture of harmonic emission. We need not worry about matching the correct solid angle of harmonic emission to simulation results. This absolute measurement of the harmonic spectra combined with 2D3V PIC simulations enables the determination of experimental conditions.

Example harmonic spectra produced from various scale lengths are shown in Figure 4.8 a) with harmonics resolved up to the 9th order, 233nm. The spectra are extracted from the 2D FFT through radially summing along constant $k = \sqrt{k_x^2 + k_y^2}$ values to capture the full spectral content. Integrated intensity curves calculated using the energy FWHM bandwidths are shown in Figure 4.8 b) with associated power law fits shown as dashed lines. The experimentally measured relative intensity values are plotted in black for comparison.

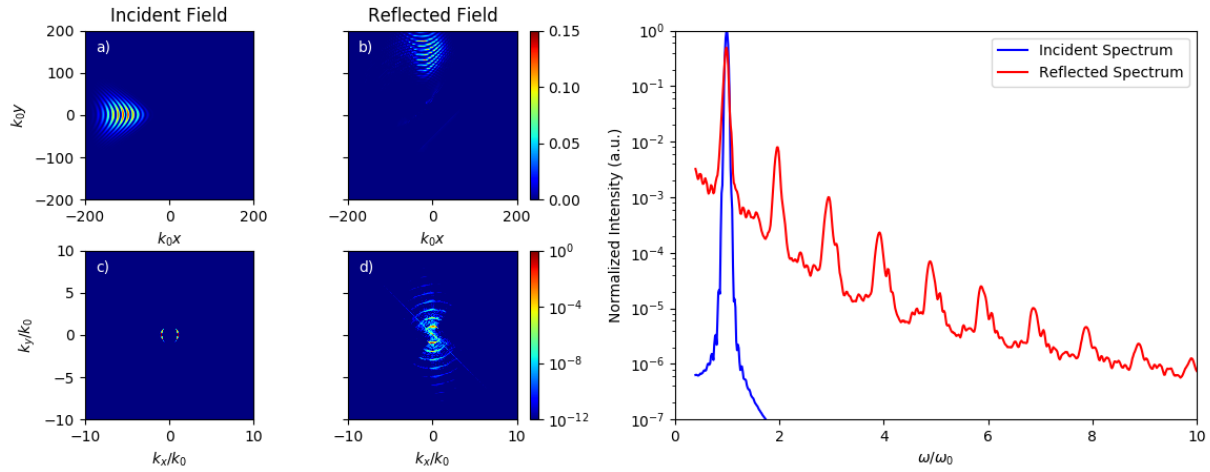

Figure 4.7: (Left) Example 2D simulation results for a plasma scale length $L_s = c/\omega_0$ a) Incident electric field intensity. b) Reflected electric field intensity. c) Incident 2D Fourier Transform. A single frequency centered at $k/k_0 = 1$ is present. d) Reflected 2D Fourier Transform. (Right) Radially integrated incident spectrum (blue) only contains the fundamental frequency, $\omega/\omega_0 = 1$, while the reflected spectrum (red) contains both even and odd p-polarized harmonics.

Figure 4.8 c) shows how the scale length of the solid density plasma dramatically alters the harmonic production. With varying scale length, the simulated harmonic intensity efficiency ($I_n = I_0\, n^{-p}$) varies from $4.1 < p < 6.0$ with a peak in harmonic efficiency occurring around $L_s = \lambda/2\pi = c/\omega_0$. This optimal scale length is consistent with previous length scale studies using an ultra-relativistic 800nm laser [90].

The measured divergence angles (black) of the optical harmonics falls within the range of angles from the simulation seen in Figure 4.8 d). Under ideal circumstances, i.e. spatially constant intensity and a plane wave source, the harmonic angular divergence should follow the diffraction-limited divergence for a given order, $\theta_n = \theta_0/n$, where θ_0 is the divergence of the incident laser [106, 120]. In practice, the laser-plasma interaction is not constant in intensity across the Gaussian focal spot. The 3rd harmonic appears to fall closer to the diffraction limited case, which is not consistent with simulated divergences of any length scale (colored lines). The discrepancy of the 3rd harmonic divergence could be due to a non-relativistic harmonic generation mechanism. The 4th harmonic falls almost identically

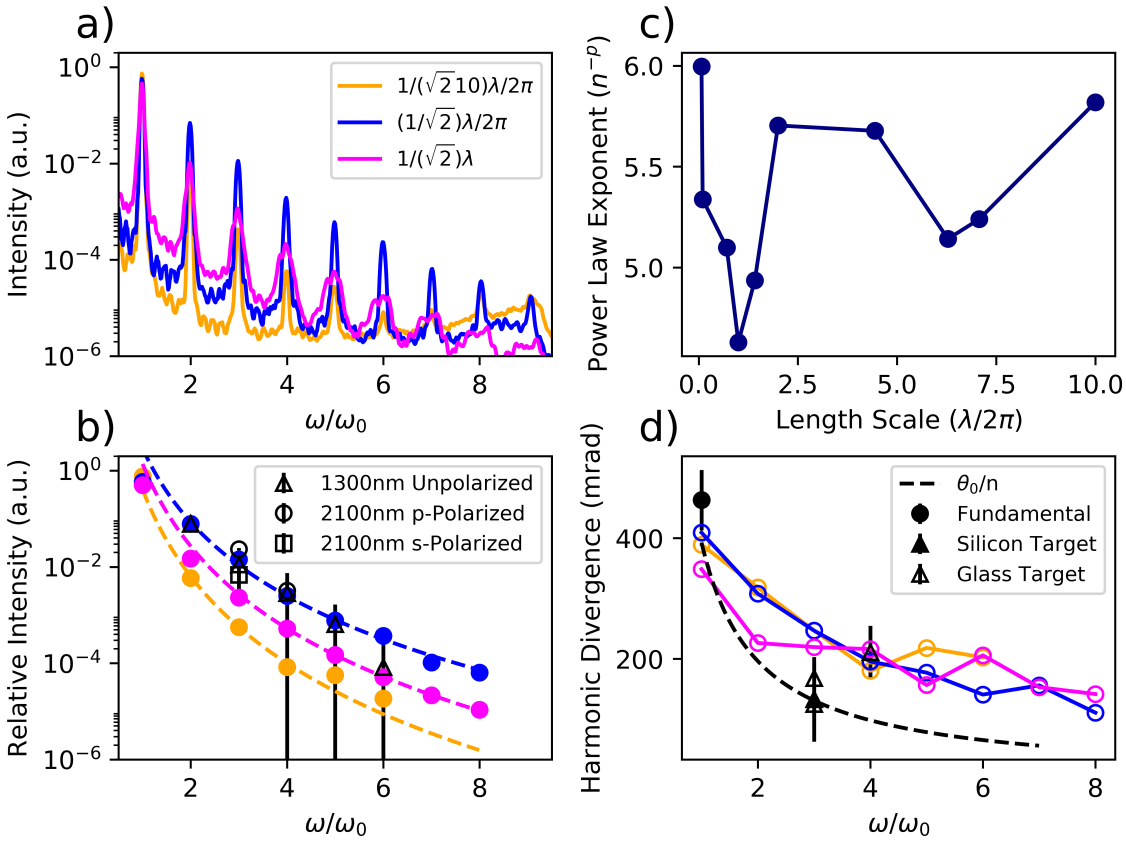

Figure 4.8: a) Example spectra for $L_s < c/\omega_0$ (yellow), $L_s \approx c/\omega_0$ (blue), and $L_s > c/\omega_0$ (pink). b) Example integrated intensity measurements comparing simulation (color) versus experiment (black) harmonic emission. Dashed lines are power law fits ($I_n = I_0\, n^{-p}$) to simulated results. c) Power law fit coefficient as a function of length scale. Increase in efficiency near $L_s = c/\omega_0$. d) Example divergence measurements for simulated (color) versus experimental (black) harmonic emission. [6]

along the trend lines of the simulated harmonics, which indicates a higher likelihood that it is produced through the high-intensity laser-plasma interaction.

4.7 Conclusion

In this chapter, the optical ROM harmonics generated from relativistic laser-solid interactions at mid-infrared wavelengths are demonstrated. Using 1300nm and 2100nm light sources at intensities $a_0 \sim 1$, harmonics were observed up to the sixth order with accompanying polarization and divergence measurements. The presented harmonic measurements in

conjunction with the PIC simulations suggests that the laser-plasma interactions are occurring with very short plasma scale lengths. This can be inferred from the difference in the harmonic intensity power law decay for the silica target compared to the silicon wafer and through comparison with the simulated length scale study. Silica has a higher ionization potential than silicon, so we can infer that silica must have a shorter plasma scale length. The measured power law decay for glass targets is given by $I(n) \propto n^{-6.9}$ compared to silicon with a power law decay of $I(n) \propto n^{-4.33}$. In order for silica to have a faster power law decay than silicon, the interactions must be occurring for length scales shorter than the ideal $L_s = c/\omega_0$. Therefore, the OPA-driven laser-plasma interactions most likely occur with near perfect step-function-like density profiles due to improved pulse contrast from the OPA process. However, due to the lack of detectable CWE harmonics, the scale length cannot be much shorter than $L_s < \lambda/15$, which is the requirement for the generation of CWE harmonics [98]. The prepulse contrast of the CUOS Lambda Cubed laser has been shown to achieve $\lambda/10$ scale lengths in previous experiments with comparable contrasts expected after the OPA process used during this experiment [121].

The next steps for the investigation of MIR ROM HHG would constitute concurrent measurement of the hot electron temperatures and optical order harmonics as a function of preplasma scale length. Previous studies suggest that the pre-plasma scale length is critical to the optimization of ROM harmonics [89, 90]. The lasers generated through the OPA process have high quality contrast ratios, which results in near-perfect step-like function plasmas. It is expected that the introduction of a heater beam, which introduces a pre-plasma before the MIR beam interacts with the target, would improve the HHG conversion efficiency. The high quality pulse contrast can be confirmed by pre-ionizing the target with a heater beam to determine if the ROM harmonic efficiency increases with additional plasma scale length.

Chapter 5

Two-beam High Harmonic Generation from Plasma Mirrors

This chapter is adapted, with permission, from a version of an article before peer review or editing, as submitted to New Journal of Physics. IOP Publishing Ltd is not responsible for any errors or omissions in this version of the manuscript or any version derived from it.

Recently, there has been increased interest in investigating the relativistic harmonic generation process through multi-beam interactions. Table-top laser technology has enabled high repetition rate systems with smaller beam diameters to produce relativistically-intense interactions. As discussed in Chapter 4, wavelength-tunable relativistic harmonic generation experiments are now possible through the manipulation of the fundamental laser wavelength through nonlinear optical processes such second harmonic generation or OPA.

Adding the laser second harmonic to the interaction has been shown to provide benefits to relativistic harmonic generation including the enhancement of conversion efficiency and attosecond burst isolation [122–126]. Recent theoretical and computational work [127, 128] has shown that high-brightness, circularly-polarized harmonics can be generated from the ROM

mechanism in an analogous manner to circularly-polarized harmonics of order $\omega_n = (3n+1)\omega$ generated in the tunnel ionization regime from counter-rotating, circular fields in collinear [129, 130] and non-collinear [131] geometries. The studies on two-beams interactions with plasma mirrors have up to this point been separated into focuses on linear or circular polarization. However, the overarching framework of the interaction is one process: the relativistic critical surface oscillations during the laser reflection generate the emitted harmonics. In order to utilize the two-color harmonics, it is important to develop a more complete picture of the two-color interaction.

In this chapter, two-color relativistic harmonic generation is investigated through the use of particle-in-cell simulations. Using non-commensurate frequencies, i.e. fields with frequency ratio $\omega_2/\omega_1 \neq \mathbb{Z}$, where ω_2 and ω_1 are the central frequencies of the fundamental fields, enables a robust examination of the laser-plasma coupling that results in two-color HHG. We show that the harmonic properties and intensity optimization are governed by the relativistic critical surface oscillations during the laser reflection. The generated two-color harmonic spectrum and polarization states are determined by the frequency ratio and polarization states of the fundamental fields, respectively. Additionally, we show that the intensity optimization of the two-color harmonic generation process occurs at equal intensities of the fundamental fields, independent of frequency ratio or polarization state.

5.1 Particle-in-Cell Simulations

Numerical 1D3V simulations were performed using the fully-relativistic, particle-in-cell code OSIRIS 4.0 [118]. For these two-color simulations, the physical quantities were normalized to the central frequency of the lower frequency laser, ω_1. The simulation region was $Z = 800\ c/\omega_1$ units long with 128 particles per cell, using a grid size of 40,000 points. This results in a spatial resolution of $\Delta z = 0.02\ c/\omega_1$. The simulations were run for a total time

of $T = 300/\omega_1$ with a time step of $\Delta t = 0.025/\omega_1$. The plasma was a slab with bulk density $n_e = 100 n_c$ and thickness 50 c/ω_1. A variable scale length exponential density ramp of the form $n_e = 100 n_c \exp(-x/L_s)$ was placed before the front surface of the target to represent pre-plasma formed by a laser pre-pulse before the high intensity interaction. The optimal pre-plasma scale length L_s was determined to be $L_s \approx \lambda_1/2\pi$, which is in agreement with previous experimental studies [89, 90, 104].

Two flat-top laser fields were initialized, each with durations of $\tau = 56.5/\omega_1$. Flat-top temporal profiles were used to simplify the plasma dynamics. The laser fields were initialized with two fundamental frequencies ω_1 and ω_2 and either linear or circular polarization. Unless otherwise specified, the presented frequency ratio was $\omega_2/\omega_1 = 1.65$ and the total normalized vector potential was held constant at $a_0 = a_{0,1} + a_{0,2} = 10$, where $a_{0,i} = eE_i/m_e c\omega_i$ is the normalized vector potential of the individual laser fields. The optimal harmonic generation was found to occur for the individual normalized vector potential values of $a_{0,1} = 6.2$ and $a_{0,2} = 3.8$. After the interaction, the light reflected back into free space; there, the reflected field was spatially filtered to remove any electric field contribution due to the plasma slab, and analyzed using fast Fourier-transforms (FFT). During the reflection, the relativistic critical surface, $\gamma n_c(x,t)$, was also tracked by taking into account the local Lorentz factor of the plasma electrons every ten simulation time steps. The resulting motion was then Fourier-transformed to extract the oscillation frequencies of the plasma.

5.2 Results

The reflected spectrum of two LP laser fields with frequencies ω_1 and ω_2 can be seen in Fig 5.1 a). The polarization angle of the higher frequency field is rotated between 0^o and 90^o such that the field polarizations are parallel (red) and orthogonal (blue). When the polarizations are orthogonal, the peak field strength is reduced to $\sqrt{a_{0,1}^2 + a_{0,2}^2} = 7.3$. Therefore, to

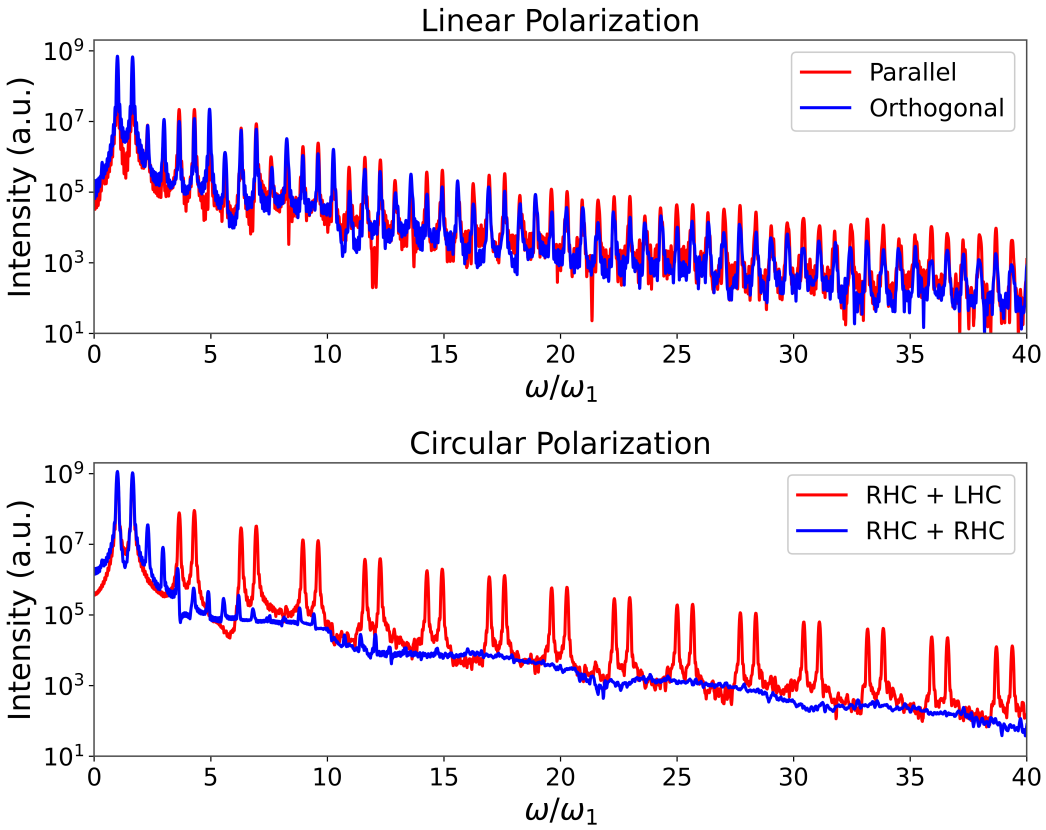

Figure 5.1: Harmonic spectra of two-color fields at normal incidence. 5.1 a) Reflected spectrum of linearly-polarized pulses. The two-color parallel (red) and orthogonal (blue) fields contain additional harmonic orders beyond the odd harmonic orders expected from a single frequency interaction. 5.1 b). Reflected spectrum of CP pulses at normal incidence. The two-color counter-rotating (red) and co-rotating (blue) fields.

produce the same peak field strength of the parallel polarization case, the normalized vector potentials of the individual fields were increased by a factor of 1.37. To account for the difference in total energy between the two interactions, the reflected spectra are normalized to the initial energy of the laser fields. Both parallel and orthogonal cases contain multiple harmonic channels that are separate from the odd harmonics produced from a single frequency at either $\omega_1 = 1$ or $\omega_2 = 1.65$. In general the two-color HHG harmonics are given by:

$$\Omega = n_1\omega_1 + n_2\omega_2, \tag{5.1}$$

where $n_1 + n_2 = 2k - 1$, and n_1, n_2, and $k \in \mathbb{Z}$.

The reflected spectra of two CP laser fields with frequencies ω_1 and ω_2 can be seen in Fig 5.1 b). The polarization of the second field at frequency ω_2 is rotated such that the fields are counter-rotating (red) and co-rotating (blue). As a reminder, single-color CP fields do not produce harmonics at normal incidence. However, two-color CP fields are capable of harmonic generation at normal incidence. Two harmonic channels in the form of doublets are present in the counter-rotating case:

$$\Omega_+ = n\omega_2 + (n-1)\omega_1 \tag{5.2}$$

$$\Omega_- = (n-1)\omega_2 + n\omega_1. \tag{5.3}$$

Harmonics are also observed when the two fields are co-rotating with selection rules:

$$\Omega = n\omega_2 - (n-1)\omega_1 \tag{5.4}$$

The co-rotating harmonics have a much faster decay when compared to either the counter-rotating fields or linearly-polarized fields.

5.2.1 Optimization of Circularly-Polarized Harmonics

As shown in Figure 5.2 a), counter-rotating fields can produce CP harmonics with high efficiency. The optimization of CP harmonics depends strongly on the ratio of two-color field strengths. The magnitudes of the individual vector potentials were varied to find the optimal ratio to produce two-color CP harmonics. Figure 5.2 b) shows an analysis of the polarization states of the harmonics $6\omega_1+5\omega_2 = 14.25\omega_1$ and $5\omega_1+6\omega_2 = 14.9\omega_1$ as functions of $a_{0,1}/a_0$. The field polarization can be measured through the polarization ellipticity $\epsilon = \min(E_x, E_y)/\max(E_x, E_y)$ and phase delay $\Delta\theta$. An LP field has no phase delay $\Delta\theta = 0$

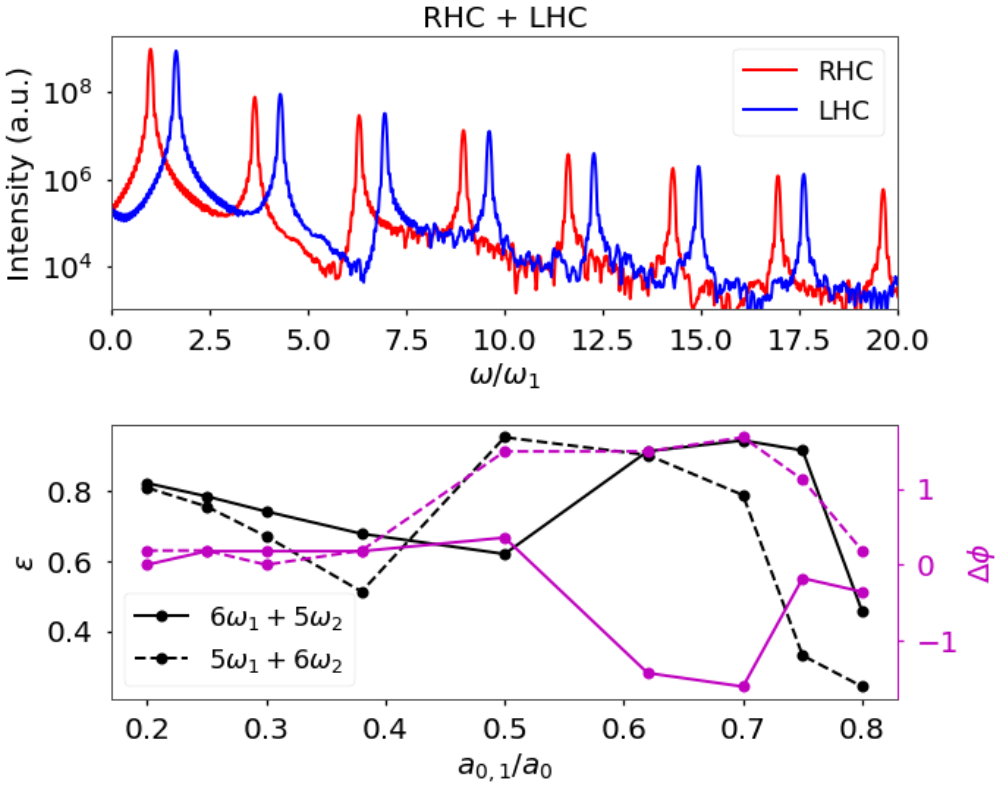

Figure 5.2: Optimization of CP harmonics. 5.2 a) Harmonic spectrum of counter-rotating fields with $a_{0,1}/a_0 = 0.62$. The harmonics produced are counter-rotating doublets. 5.2 b) Ellipticity (black) and phase (magenta) of harmonics $6\omega_1 + 5\omega_2$ and $5\omega_1 + 6\omega_2$ as the field strength ratio $a_{0,1}/a_0$ is varied. The harmonics exhibit nearly-perfectly circular polarization near the optimal condition of $a_{0,1}/a_0 = 0.62$. 5.2

between the fields, and a CP field has an $\epsilon = 1$ and $\Delta\theta = \pm\pi/2$. When $\Delta\theta = \pi/2$ the field is left-circularly polarized, and when $\Delta\theta = -\pi/2$ the field is right-circularly polarized. The harmonics remain nearly linearly-polarized until the field strengths approach $a_{0,1}/a_0 = 0.62$ when the two harmonics become nearly perfectly circular with two counter-rotating harmonics constituting each harmonic doublet. Figure 5.2c shows a field map of the $6\omega_1+5\omega_2$ harmonic at $a_{0,1}/a_0 = 0.62$ showing the high degree of circularity in the electric field.

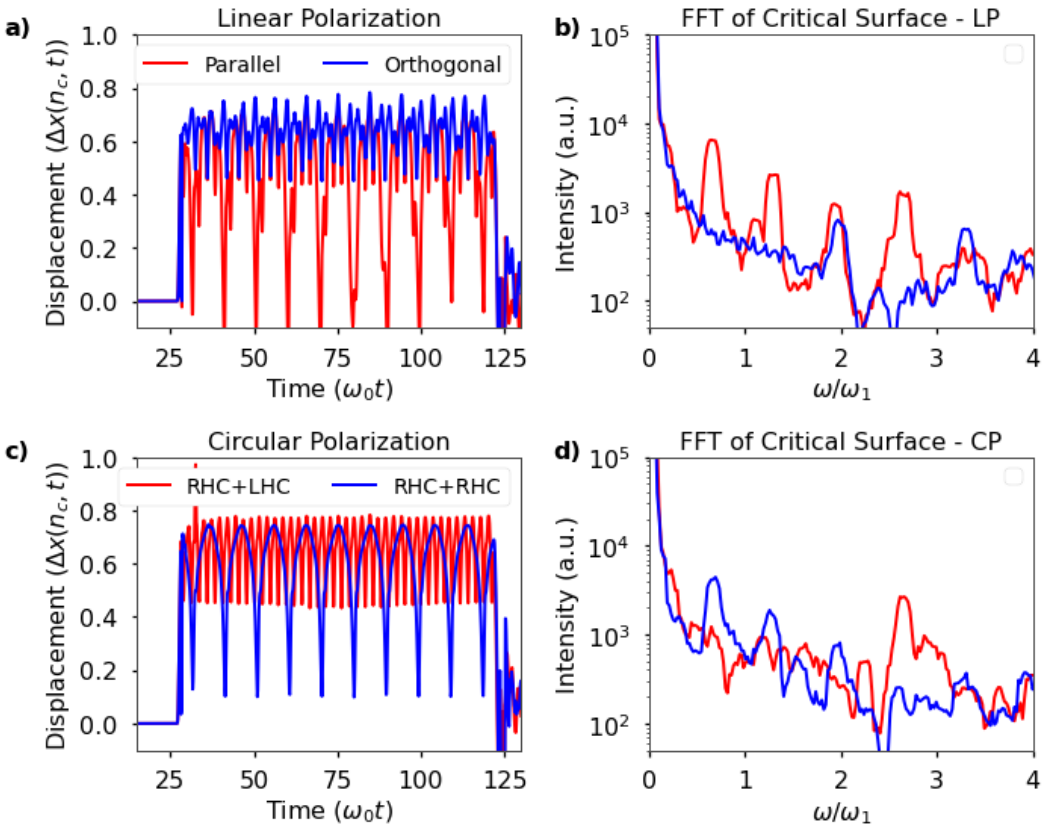

Figure 5.3: Relativistic Critical Surface Motion. 5.3 a) LP parallel (red) and orthogoal (blue) fields drive the electron surface with different magnitudes. 5.3 b) The oscillation frequencies of the linear cases are dominated by beat frequencies, $\omega_2 \pm \omega_1$, in the parallel case and twice the fundamental frequencies, $2\omega_2$ and $2\omega_1$, in the orthogonal case. 5.3 c) CP counter-rotating (red) and co-rotating (blue) fields produce oscillations in contrast with a single color interaction. 5.3 d) The CP fields produce oscillations dominated by the beat frequencies.

5.2.2 Relativistic Critical Surface Motion

The displacement of the plasma relativistic critical surface $\Delta x(\gamma n_c, t)$ for the different polarization cases presented above is plotted in Figure 5.3. Figure 5.3 a) Figure 5.3 b) show the displacement and associated Fourier transform of the electron critical surface during the refection of parallel (red) and orthogonal (blue) polarizations. Electron oscillations in the parallel case are much stronger compared to the orthogonal case. The parallel polarization contains frequency oscillations at the field beat frequencies $\omega_2 \pm \omega_1$ as well as at twice the fundamental frequencies, $2\omega_1$ and $2\omega_2$; the orthogonal polarization contains only the modes from twice the fundamental frequencies. Figure 5.3 c) Figure 5.3 d) show the displace-

ment and associated Fourier transform of the electron critical surface during the refection of counter-rotating (red) and co-rotating (blue) CP cases. The critical surface oscillations are dominated by a single beat frequency each. The counter-rotating fields produce critical surface oscillations at the sum frequency, $\omega_2 + \omega_1$, and the co-rotating fields produce oscillations at the difference frequency, $\omega_2 - \omega_1$.

5.3 Discussion

5.3.1 Harmonic Selection Rules

As discussed in Chapter 2 the harmonic frequencies generated during the reflection can be determined by the oscillation frequencies of the electron critical surface. The two-color produce more complex surface oscillations leading to emission which contains multiple harmonic channels that are separate from the odd harmonics produced from a single frequency at either ω_1 or ω_2. For parallel polarization, the electron surface oscillations as seen in 5.3 b) contain both the beat frequencies of $\omega_2 \pm \omega_1$, and twice the fundamental frequencies $2\omega_1$ and $2\omega_2$. The reflected field will therefore contain harmonic frequencies of the form $\Omega = \omega_{1,2} + 2n_1\omega_1 + 2n_2\omega_2 + n_3(\omega_1 + \omega_2) + n_4(\omega_1 - \omega_2)$ in agreement with the theoretical model of [122]. The generated harmonic frequencies can be rewritten in the form:

$$\Omega = (2n_1 + n_3 + n_4 + 1)\omega_1 + (2n_2 + n_3 - n_4)\omega_2 \tag{5.5}$$

$$\Omega = (2n_1 + n_3 + n_4)\omega_1 + (2n_2 + n_3 - n_4 + 1)\omega_2. \tag{5.6}$$

The individual terms of Equations 5.5 and 5.6 always have opposite parity, and it is possible to recast these selection rules for the parallel field polarization in the same form as Equation

5.1. For orthogonal fields, the electron surface are be dominated by twice the fundamental frequencies of the incident fields, $2\omega_1$ and $2\omega_2$. The reflected field in this case yields harmonic frequencies of the form:

$$\Omega = (2n_1 + 1)\omega_1 + 2n_2\omega_2 \tag{5.7}$$

$$\Omega = 2n_1\omega_1 + (2n_2 + 1)\omega_2, \tag{5.8}$$

which similarly can be written in the form of Equation 5.1.

The general form of Equation 5.1 suggests that the ROM harmonic generation process is consistent with the quantum mechanical description of harmonic generation processes, wherein individual photons are summed together to generate one higher order photon. A restriction imposed by the symmetry of the normal-incidence interactions is that the oscillations modes limit the generated harmonics to those composed of an odd number of photons. These selection rules also indicate why the parallel polarization produces brighter harmonics for similar field strengths. Equations 5.5 and 5.6 contains two additional channels, n_3 and n_4, due to the presence of beat frequency oscillations that are lacking in the orthogonal HHG case, which increases the likelihood of their generation and the apparent brightness when compared to orthogonally-polarized fields.

Two-color, CP fields are capable of driving electron surface oscillations due to having minima in the transverse electric field [100]. For the counter-rotating fields case, the mirror motion contains the single oscillation frequency at $\omega_2+\omega_1$. Therefore, the generated harmonics orders of the form $\Omega_+ = n\omega_2+(n-1)\omega_1$ and $\Omega_- = (n-1)\omega_2+n\omega_1$ are expected, which is consistent with the selection rules from Equations 5.2 and 5.3. In addition, because the two fields are different frequencies there exist electron oscillations that will produce CP harmonics from co-rotating fields. The co-rotating fields produce electron surface oscillations at frequency

$\omega_2 - \omega_1$, which generates harmonic orders of the form $\Omega = \omega_1 + n(\omega_2 - \omega_1) = n\omega_2 - (n-1)\omega_1$, in agreement with Equation 5.4.

The presence of harmonic doublets in the counter-rotating case and a single harmonic channel in the co-rotating case is consistent with the quantum model of the conservation of spin-angular momentum, where the final photon generated from the interaction must have photon spin $\sigma = \pm 1$. In this model, the harmonics are being generated from the linear addition of photons from each field such that each harmonic contains one extra photon from either field in order to preserve $\sigma = \pm 1$.

Field Types	ω_1 Pol.	ω_2 Pol.	Selection Rules	Harmonic Polarization
LP	E_x	E_x	$\Omega = n_1\omega_1 + n_2\omega_2$	E_x
LP	E_x	E_y	$\Omega = n_1\omega_1 + n_2\omega_2$	45° between E_x and E_y
CP	RHC	LHC	$\Omega_{+,-} = n\omega_{2,1} + (n-1)\omega_{1,2}$	LHC, RHC
CP	RHC	RHC	$\Omega = n\omega_2 - (n-1)\omega_1$	RHC

Table 5.1: Harmonic selection rules for linear and circularly polarized two-color fields.

The selection rules for two-color, LP and CP fields are summarized in Table 5.1. The harmonic polarization of linearly-polarized, parallel fields are along the same polarization axis as the fundamental fields. Orthogonally-polarized fields with one color polarized along E_x and the other polarized along E_y produced harmonics with polarization at 45° between the incidence fields. Counter-rotating, CP fields produce harmonic doublets with counter-rotating polarization and co-rotating, CP fields produce rapidly decaying harmonics that are the same helicity as the incident fields.

5.3.2 Optimization of Two-Color Harmonic Generation

A two-color laser pulse can be represented as a superposition of two single-color laser pulses defined by amplitudes $a_{0,1}$ and $a_{0,2}$ and central frequencies ω_1 and ω_2. An electromagnetic field with arbitrary polarization propagating in the $\hat{z}$-direction can be written in terms of

the vector potential:

$$\mathbf{A}_i = \delta_i a_{0,i} \cos\omega_i t\ \hat{x} + (1-\delta_i^2)^{1/2} a_{0,i} \sin\omega_i t\ \hat{y}, \tag{5.9}$$

where δ_i is a polarization parameter defined such that $\delta_i = \pm 1, 0$ for an LP laser and $\pm 1/\sqrt{2}$ for a CP laser. The total vector potential of a general two-color laser field is then simply the summation of the two fields

$$\begin{aligned} \mathbf{A} &= [\delta_1 a_{0,1} \cos\omega_1 t + \delta_2 a_{0,2} \cos\omega_2 t]\hat{x} \\ &+[(1-\delta_1^2)^{1/2} a_{0,1} \sin\omega_1 t + (1-\delta_2^2)^{1/2} a_{0,2} \sin\omega_2 t]\hat{y}. \end{aligned} \tag{5.10}$$

For LP fields with parallel polarizations along the $\hat{x}$-direction, the total vector potential corresponds to the case of $\delta_1 = \delta_2 = 1$

$$\mathbf{A} = [a_{0,1} \cos\omega_1 t + a_{0,2} \cos\omega_2 t]\hat{x}. \tag{5.11}$$

For an electron initially at rest in a normal incidence geometry, the canonical momentum in the transverse direction is a conserved quantity, $\mathbf{p}_\perp = \mathbf{A}$, where $\mathbf{p}_\perp$ and $\mathbf{A}$ are the transverse electron momentum and laser vector potential, respectively. The longitudinal momentum, p_z, of the electron can be shown [81] to equal $p_z = (1 - \mathbf{p}_\perp^2)/2$.

According to the theory of relativistic harmonic generation described by Baeva, *et al.* [100], the harmonic emission occurs when the transverse momentum of the critical surface electrons $\mathbf{p}_\perp$ reaches a minimum. The transverse electron momenta is $p_x = a_{0,1} \cos\omega_1 t + a_{0,2} \cos\omega_2 t$, which is minimized when $\frac{d}{dt} p_x = 0$ or $a_{0,1}\omega_1 \sin\omega_1 t = -a_{0,2}\omega_2 \sin\omega_2 t$. The oscillatory com-

ponents are simultaneously at their extrema positions when

$$t = \frac{(2\pi + 1)n}{\omega_1 \pm \omega_2}. \tag{5.12}$$

Therefore, we find that there is a ratio of the laser vector potentials that will lead to a minimization of $p_\perp$ at $a_{0,1}\omega_1 = a_{0,2}\omega_2$. Written in terms of laser intensity, the minimization occurs when the two fields are of equal intensity $I_1 = I_2$.

In contrast to a single color circularly-polarized pulse at normal incidence, this minimization can also occur for two-color circularly-polarized fields. Two circularly-polarized fields with opposite helicities corresponds to $\delta_1 = 1/\sqrt{2}$ and $\delta_2 = -1/\sqrt{2}$

$$\mathbf{A} = [\frac{a_{0,1}}{\sqrt{2}} \cos\omega_1 t - \frac{a_{0,2}}{\sqrt{2}} \cos\omega_2 t]\hat{x} + [\frac{a_{0,1}}{\sqrt{2}} \sin\omega_1 t + \frac{a_{0,2}}{\sqrt{2}} \sin\omega_2 t]\hat{y}. \tag{5.13}$$

The transverse momenta for an electron in a two-color CP field with opposite helicities are given by

$$p_x = \tfrac{a_{0,1}}{\sqrt{2}} \cos\omega_1 t - \tfrac{a_{0,2}}{\sqrt{2}} \cos\omega_2 t \tag{5.14}$$

$$p_y = \tfrac{a_{0,1}}{\sqrt{2}} \sin\omega_1 t + \tfrac{a_{0,2}}{\sqrt{2}} \sin\omega_2 t. \tag{5.15}$$

In order for harmonics to be emitted, the two momenta need to be simultaneously minimized. This results in the system of equations

$$a_{0,1}\omega_1 \sin\omega_1 t = a_{0,2}\omega_2 \sin\omega_2 t \tag{5.16}$$

$$a_{0,1}\omega_1 \cos\omega_1 t = -a_{0,2}\omega_2 \cos\omega_2 t. \tag{5.17}$$

These equations are simultaneously satisfied when

$$t = \frac{2\pi n}{\omega_1 + \omega_2}, \tag{5.18}$$

and again results in $a_{0,1}\omega_1 = a_{0,2}\omega_2$. In fact, these types of matching conditions are also satisfied for linearly-polarized fields with arbitrary polarizations and circularly-polarized fields of the same helicity. This type of optimization is most obviously seen in the circularly-polarized harmonic generation case shown in Figure 5.2. The optimal harmonic generation occurs in a narrow range around $a_{0,1}/a_0 = 0.62$, which for fields with frequency ratio $\omega_2/\omega_1 = 1.65$ is exactly the ratio needed for equal intensities. This optimization point can be easily understood in the context of quantum mechanism conservation of spin-angular momentum in the circularly-polarized case, which need on average an equal number of photons from each field for circularly-polarized harmonics to be generated efficiently.

5.3.3 2D Oblique Simulations

So far, we have demonstrated that the ROM mechanism is a robust process that can be used to control the spectral and polarization of generated EUV emission through collinear, two-beam interactions at normal incidence. However, normal incidence interactions are generally impractical for ultra-relativistic, petawatt-class experiments. A suitable alternative involves a two-beam, oblique-incidence geometry. 2D3V simulations were performed with a simulation region with size $300c/\omega_1 \times 350c/\omega_1$ with 16×16 particles per cell and a grid size of 5000×5000 points. This results in a spatial resolution of $\Delta z \times \Delta x = 0.06c/\omega_1 \times 0.07c/\omega_1$. The plasma slab was initialized at a 45° angle with respect to the laser axis with a thickness of $25c/\omega_1$.

Figure 5.4 a) shows the spectrum of p-polarized fields reflecting at a 45° angle of incidence. The fundamental fields for ω_1 (yellow) and ω_2 (red) are plotted with the optimized two-color case of $a_{0,1}/a_0 = 0.62$ (blue). At oblique angles the symmetry of a normal incidence

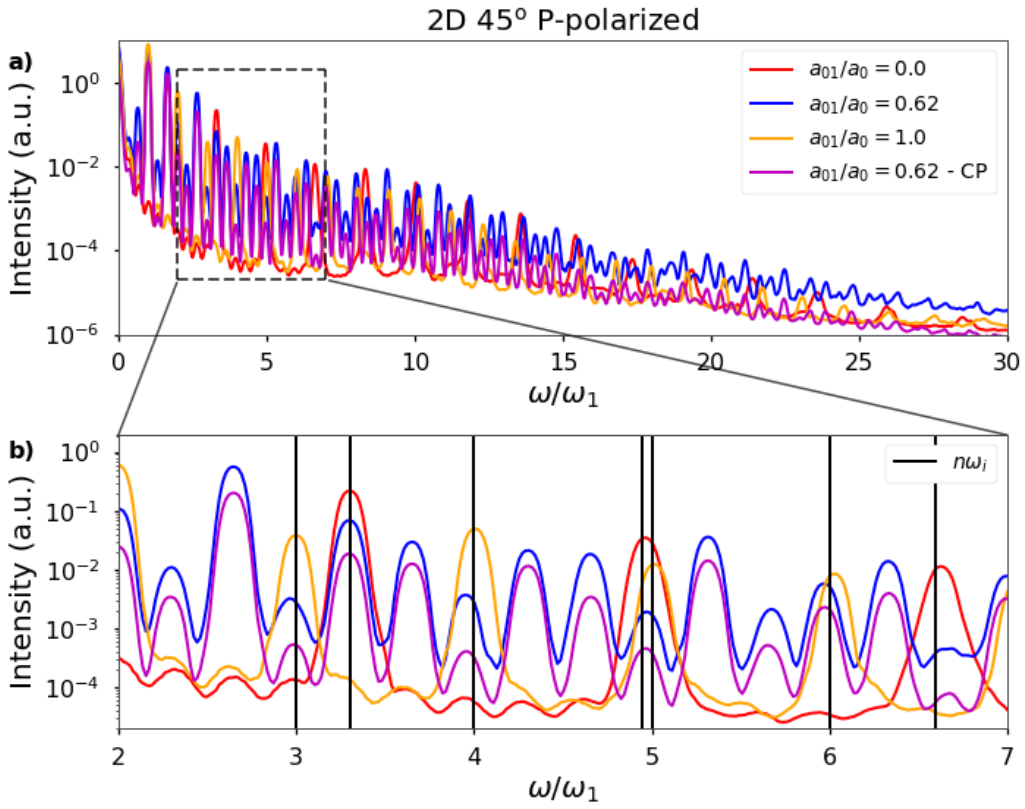

Figure 5.4: Oblique incidence harmonic spectra. 5.4a) Harmonic spectra of two color fields (blue) with comparison spectra from single color fields at ω_1 (yellow) and ω_2 (red). Additional harmonics are present due to additional harmonic channels available at oblique incidence. 5.4b) Harmonic spectra between $\omega/\omega_1 = 2$ and $\omega/\omega_1 = 7$. Harmonics of the two fundamental fields are overlain in black.

interaction is broken, and even order harmonics can now be generated. Figure 5.4 b) shows a zoom in of the spectra between $2\omega_1$ and $7\omega_1$ with vertical bars denoting the even and odd order harmonics of $\omega_1 = 1.0$ and $\omega_2 = 1.65$. While the two-color harmonic spectrum is more complex than the normal incidence case due to the increased number of oscillation modes of the mirror surface, it is still clear that there are harmonics that are being generated from the linear combination of the two fields.

5.4 Conclusion

In this chapter, the interaction of relativistically-intense, two-color laser fields with solid density plasmas is studied through particle-in-cell simulations. By combining non-commensurate fields with frequencies ω_1 and ω_2, we have shown that the relativistic harmonic generation process is a robust mechanism to control the polarization and frequency of emitted photons by tuning the incident field properties such as polarization. The benefit of driving two-color harmonic generation enables the possibility of generating frequency-tunable harmonics with controllable polarization states. We have found that the two-color harmonic generation optimization occurs for a similar intensity ratio of the two driving fields, regardless of the incident polarization states.

Future, two-color experiments can be designed to exploit optimizations and geometries discussed in this work. Experiments which have polarization and intensity control of their incident fields can optimize harmonic generation through varying the individual field intensities during linearly-polarized interactions, before rotating their individual polarizations to produce circularly-polarized harmonics. High-power OPA systems such as the L1 Allegra at ELI Beamlines and the proposed EP OPAL system at the Laboratory for Laser Energetics [132] are ideal systems to perform two-color, relativistic harmonic generation through tunable, non-commensurate wavelengths.

Chapter 6

Observation of Depth of Heating in Highly-Ionized Copper

In this chapter, discussion of the simultaneous front and rear side K-shell line emission from atoms ionized up to H-like Cu produced *via* laser-solid interactions at ultra-relativistic intensities ($I \simeq 10^{21}$ W/cm^2) obtained using the frequency-doubled ALEPH laser [3]. Measurements of the scaling of x-ray emission from Cu foil and buried-layer targets indicate that the solid-density plasma is volumetrically heated to keV temperatures at depths of $> 1\mu$m by the energetic electron population. The high-resolution x-ray data are compared with supporting collisional-radiative and particle-in-cell modeling to further constrain the experimental plasma parameters.

X-ray emission spectroscopy has been used extensively as a diagnostic of electron density, temperature, and hot electron dynamics in laser-produced plasmas [53–61], but there have been few studies of high-resolution spectroscopy of matter formed via ultra-relativistic ($I \simeq 10^{21}$ W/cm^2), laser-solid interactions [62, 64]. At these intensities, the radiation intensity dominate standard collisional atomic processes, creating HED states of matter. High

resolution x-ray spectroscopy enables the investigation of changes in K-shell x-ray emission of thin foil and buried layer targets to elucidate the generation and propagation of hot electrons [133–136]. In thin targets, these energetic electrons can be rapidly accelerated through refluxing [65], which is responsible for the dominate heating mechanism in solid targets [137, 138].

6.1 Experimental Setup

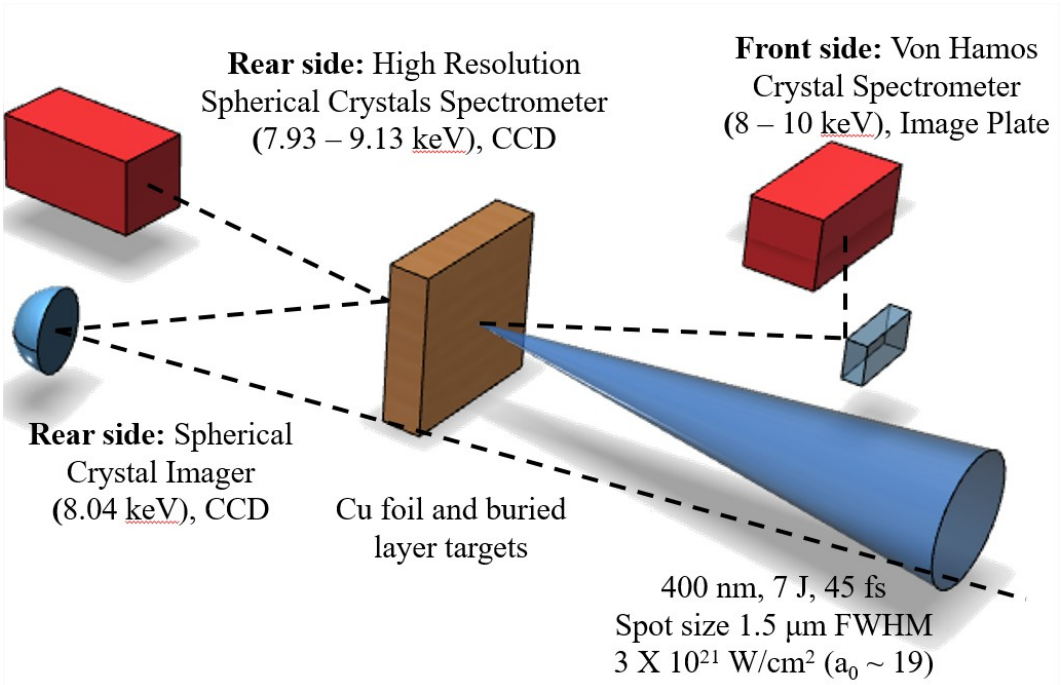

Figure 6.1: Simultaneous measurements of Cu K-shell fluorescence from front and rear-side diagnostics. A mica von Hamos spectrometer captures front-side K-shell emission from 8-10 keV. Two germanium-220 spherical crystals capture rear-side K-shell emission in the range of 8-9 keV while a quartz-2131 spherical crystal images rear-side Kα emission. Image credit: Amina Hussein

The experiments were conducted by irradiating copper foils and layered targets with the frequency-doubled Ti:Sapphire ALEPH laser at Colorado State University [3], which delivered pulses with 45 fs FWHM pulse duration, 400 nm central wavelength, and up to 7 J focused by an f/2 parabola on target. The use of the laser second harmonic suppresses laser pre-pulse producing ultrahigh contrasts ($> 10^{11}$) that lead to hot, solid-density plasma [63].

The s-polarized laser energy and the spot size was varied between 0.25 - 7 J and 1.5 - 10 μm, respectively, to obtain intensities ranging from 3×10^{18} and 3×10^{21} W/cm^2 . Copper foils of thickness varying from 0.5 to 15 μm and buried-layer target of 0.5 μm Cu layers between 1 and 5 μm of aluminum and polyethylene (CH) were irradiated at near normal incidence. The orientation of the buried-layered targets was varied to change the relative depth of the Cu layer with respect to the laser focus.

A quartz-2131 spherical crystal imager was fielded at ALEPH. The crystal has a $2d$ separation of 3.082Å, and a Bragg angle of 88.7^o for the 2$^{\text{nd}}$ order diffraction of the Cu Kα line. The crystal is spherically-bent with a radius of curvature $R = 150$mm. Due to the size of the ALEPH chamber, the crystal needed to image the source a minimum of 80cm from the crystal surface. The object distance is $o = 8.25$ cm and the image distance is $i = 82.5$ cm for a total magnification $i/o = 10$.

Simultaneous front- and rear-side K-shell emission of copper was captured by fielding a moderate-resolution ($E/\Delta E \sim 1000$) von Hamos mica crystal spectrometer [139] and a high-resolution ($E/\Delta E > 7500$) germanium-220 spherical-crystal spectrometer with viewing angles of 45° on the front side and target normal on rear side, respectively. The von Hamos spectrometer had an energy range of 8-10 keV, and was coupled to MS-type image plate (IP) read by a Fuji scanner with 100μm step-size, which was read after every shot. Emission was calculated taking into account sensitivity of the IP, transmission of beryllium and aluminum filters, and crystal reflectivity. The spherical-crystal spectrometer consisted of two Ge-220 crystals capturing the spectral ranges of $7.95 - 8.45$ keV and $8.7 - 9.1$ keV and was coupled to an Microline e2v 4240 vacuum CCD with a 13.5μm × 13.5μm pixel size. Emission was calculated taking into account CCD sensitivity, transmission of aluminum filters, and crystal reflectivity. It was assumed that the photons were emitted uniformly over 4π steradians and no attenuation by the target plasma was taken into account for both diagnostics.

Example front-side spectra at high and low intensity taken with the von Hamos spectrome-

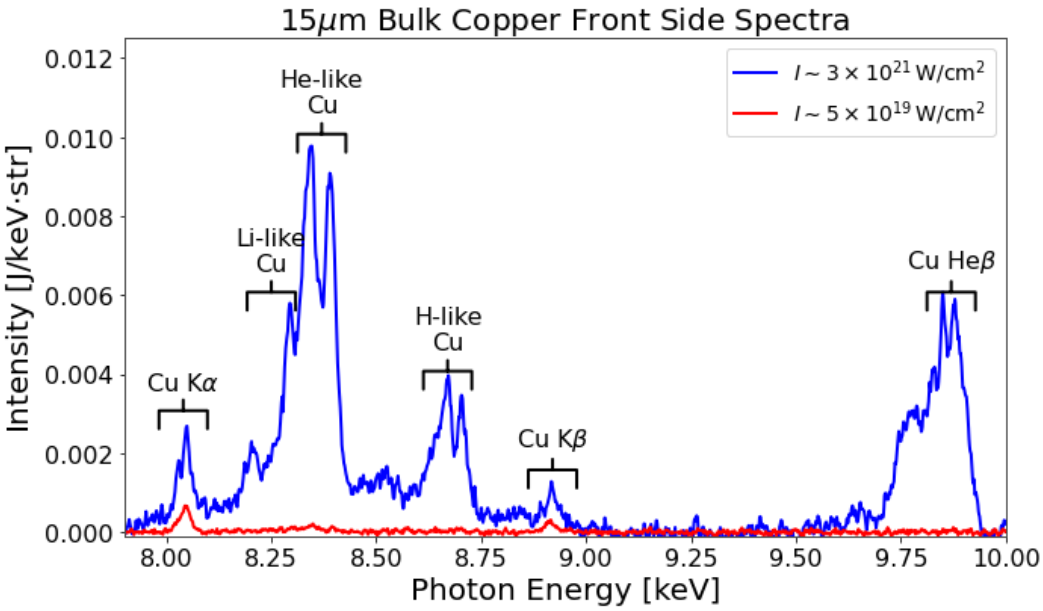

Figure 6.2: Example front-side von Hamos spectra at high (red) and low (intensity)

ter can be seen in Figure 6.2. Copper foils of with 15 μm thickness are illuminated by the high-contrast second harmonic. At "low" intensities $I \sim 5 \times 10^{19}$ W/cm^2 Cu Kα and Kβ are observed, which suggests a dominance of cold copper contribution to the emission spectrum. The emission of Kα and Kβ are dominated by energetic electrons knocking out inner-shell electrons of cold material, before the transition of an L or M-shell electron to fill the vacancy. When increasing the intensity to $I \sim 3 \times 10^{21}$ W/cm^2 highly-ionized copper emission dominates the spectrum. Copper Heα and Lyα are alongside Li-like satellites suggests significant emission is occurring in the central hot-spot of the laser focus. The ratio of He-like copper to the Li-like satelites and the Lyα doublet suggests that the average charge of the plasma hot-spot is $Z^* = 27$ with bulk temperatures $T > 1$ keV.

An example of simultaneous front and rear-side emission of 15 μm copper foils illuminated at $I \sim 3 \times 10^{21}$ W/cm^2 is shown in Figure 6.3. The rear-side spectrum contains a clear Kα doublet, with minimal Kβ or Heα . The significantly weaker Heα from the rear-side emission is an indication of a strongly absorbing layer between the hot-plasma surface and the rear-side spectrometer.

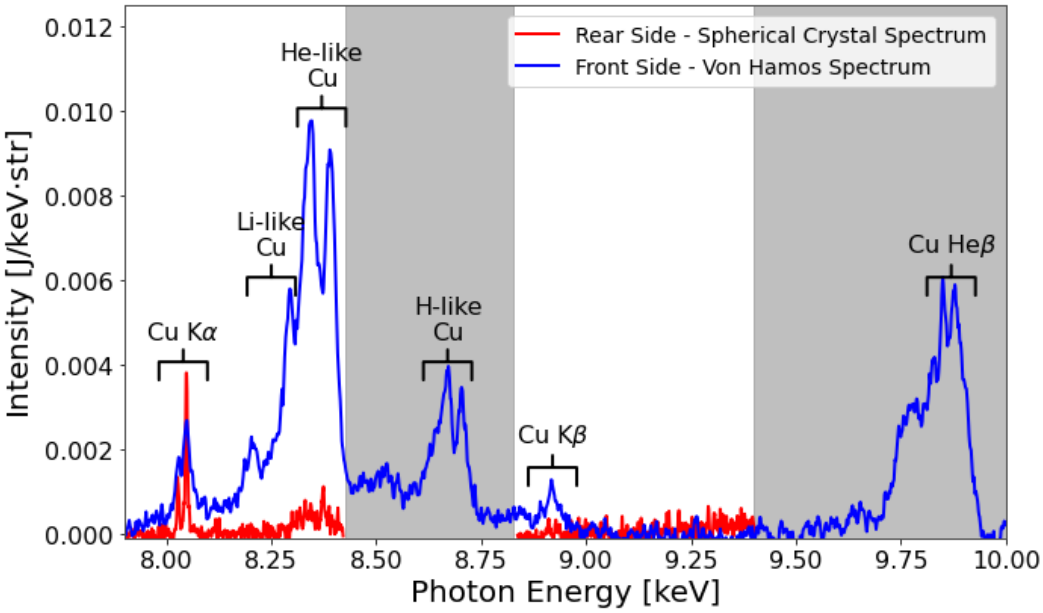

Figure 6.3: Example front-side (blue) and rear-side (red) spectra.

6.2 Results

Before alignment of high resolution spectrometer, initial measurements of the K-shell emission were taken by moving the von Hamos spectrometer to capture either front- or rear-side emission. The measurements were taken on different shot days, so fluctuations in laser energy[1] could impact the direct comparison. However, since the alignment of the von Hamos resulted in nearly identical parameters, the relative intensity of the plasma emission can be directly compared to estimate the difference in signal.

Figure 6.4 shows the differences between front- and rear-side emission of 1 μm and 5 μm thick copper foils illuminated at $I \sim 2 - 3 \times 10^{21}$ W/cm^2 . 1 μm thick foil spectra (Figure 6.4 a) contain no detectable Kα or Kβ , which indicates that the 1μm thick foils are being heated through their entire depth to high temperatures. Already at 1 μm thicknesses the Heα and Lyα lines on the rear-side are less intense than the front side emission, which indicates there is an opaque region contributing to line reabsorption. Conversely, 5 μm thick foils (Figure

[1]Fluctuations in ALEPH's energy is highly-dependent on the SHG process in the KDP crystal. Typically shot-to-shot fluctuations were $\Delta E \leq 1$ J.

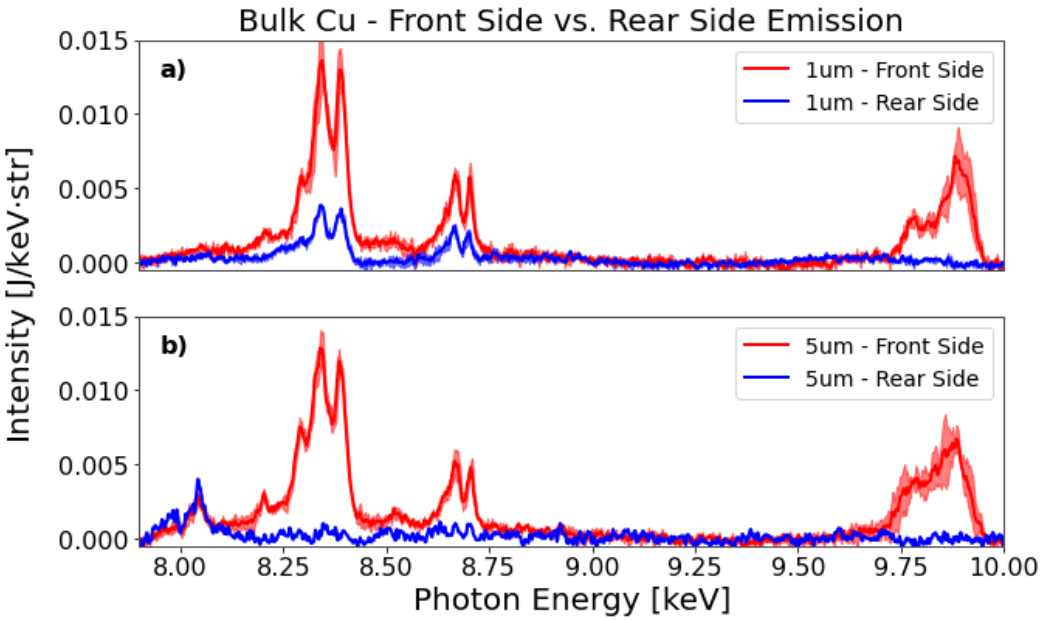

Figure 6.4: Front and rear side emission from high intensity shots. Shaded regions indicate standard deviation of three shots taken at each condition.

6.4 b) contain resolvable Kα emission, which indicates a region of cold plasma where hot electrons are causing K-shell vacancies. However, rear side Heα and Lyα emission is no longer resolvable above the noise.

A thickness scan of 0.5-15 μm thick copper foils was performed with simultaneous front- and rear-side emission captured by spectrometers is plotted in Figure 6.5. Figure 6.5 a) shows the front side emission from copper foils irradiated at high intensity. Highly-ionized copper is observed for all thicknesses with an increase Li-like copper and cold Kα for thicker targets. Figure 6.5 b) shows the rear side emission for the same targets. He-like copper emission is only observed for the 0.5 and 1 μm thick foils, while thicker targets have a strong Kα doublet. Dense, hot plasmas re-absorb resonant photons through photo-excitation. Given a similar charge distribution of the emitting plasma, as evidenced by front-side emission spectra, there must be a region of colder, dense plasma between the emission region and rear-side detector. This region must still be hot enough ($T_e \sim 1 - 2$ keV) to re-absorb He-like copper emission without contributing to the emission profile.

6.2.1 Copper Foil Thickness Scans

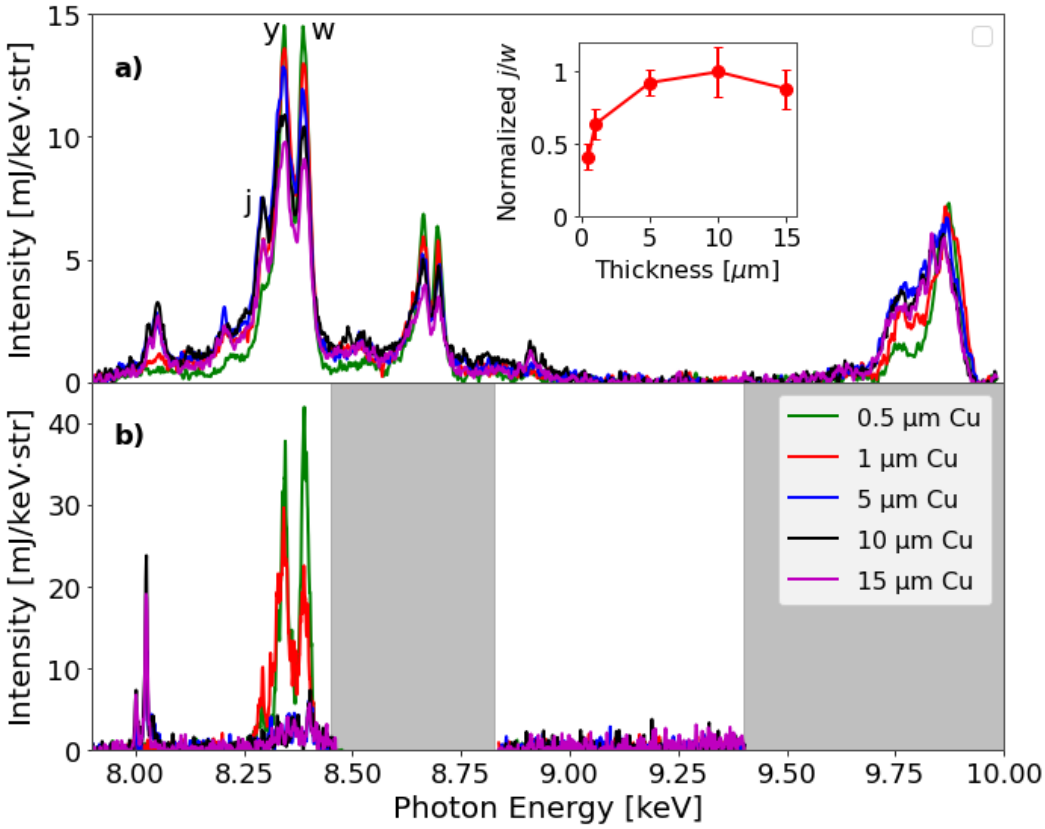

Figure 6.5: Simultaneous front and rear side emission from high intensity shots shows suppression of highly-ionized rear-side emission from targets thicker than 1 μm . The gray boxes indicate regions outside the spectral window of the spherical crystals. Inset: Calculated normalized ratio of the j Li-like satellite to w Heα resonance line.

Examination of the trends in plasma line emission provides a method to understand plasma conditions. In Figure 6.5 a) front-side emission lines of interest are marked using Gabriel's notation [140]. These lines are the 1s2p ^{1}P$_1$ $\rightarrow$ 1s^2 ^{1}S$_0$ resonance transition (w), the 1s2p ^{3}P$_1$ $\rightarrow$ 1s^2 ^{1}S$_0$ intercombination (y), and the Li-like satellite (j). Of particular interest is the ratio of the front-side j/w emission, which gives an indication of the populations of Li-like and He-like Cu [141]. The front-side j/w ratio for different Cu thicknesses is plotted in the inset of Figure 6.5. The ratio of j/w is increasing for the 0.5, 1 and 5 μm targets before flattening at 10 and 15 μm . This indicates that the x-ray-weighted electron temperature T_e is falling as the targets increase in thickness. Even if the Heα w line is lowering due to opacity effects,

the Li-like emission is increasing at the same time, which indicates a lower temperature. Further, the 15 μm spectrum (pink) is uniformly lower than the 10 μm spectrum (black), which could be from a smaller emitting volume due to increased heat dissipation in the thicker target.

6.2.2 Copper K-alpha Images

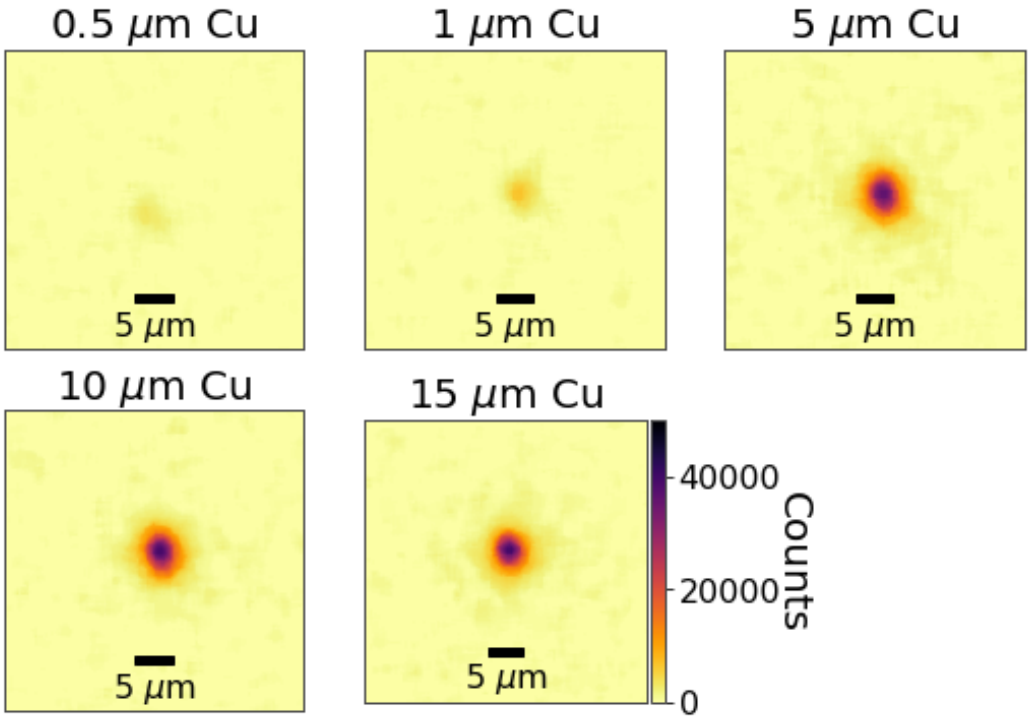

Figure 6.6: SCI images of copper foils. The Cu Kα spot size is full-width at half-maximum is on the order of ∼ 5μm for all target thicknesses. All images are displayed on the same scale.

As discussed previously, Kα x-ray emission can be indicative of fast electron transport. Fast electrons traveling through cold plasma with sufficient energy to create K-shell 1s vacancies allow for 2p→ 1s transitions. The emission region of Kα then corresponds to the fast electron transport range and divergence through the target, and can act as an upper bound on the size of significant heating in the plasma. SCI images of the rear-side Kα emission were recorded. Figure 6.6 shows single shot images of the Kα rear-side emission captured simulataneously with the x-ray spectra from Figure 6.5. The measured Kα spot size was ∼ 5μm for all targets,

and suggests that the hot electrons are generated and confined in the same way. Similar to the x-ray spectra, the Kα images of the thinnest targets, 0.5 and 1 μm foils, show very little Kα emission before quickly increasing in signal intensity for the 5 μm foils. This acts as a secondary check that the emitting plasma of the thinnest targets contains very little cold copper to emit Kα .

6.2.3 Buried Layer Targets

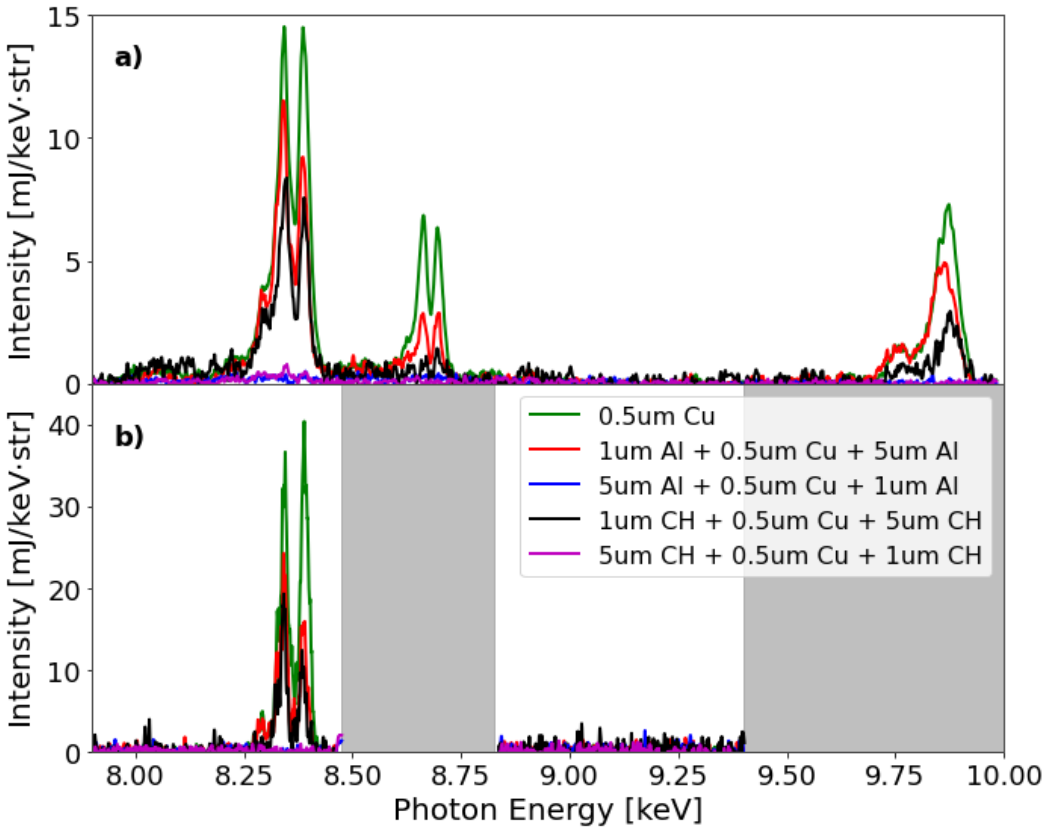

Figure 6.7: Simultaneous front- and rear-side K-shell emission from sandwich targets.

A further examination of the depth of heating was performed by using layered foil targets. Buried layer targets with thin tracer layer have been used extensively in order to determine depth of heating and to understand fast electron propagation in laser-plasma interactions [64, 142–145]. The use of a thin (0.5 μm) Cu layer is chosen to minimize temperature gradients of the emitting plasma. The x-ray emission of the layered targets irradiated on

both the thin (1 μm) or thick (5 μm) sides are seen in Figure 6.5. The intensity of the front- (Figure 6.5 c) and rear-side (Figure 6.5 d) emission is lower with respect to a 0.5 μm Cu foil, which suggests the emitting plasma is at a lower temperature. Temperatures sufficient to produce He-like and H-like Cu at a depth of 1 μm are observed for both the Al and CH sandwich targets, but the lack of any emission lines from the 0.5 μm Cu buried under 5 μm of Al or CH suggests minimal heating at depths of 5 μm into the sandwich targets.

6.3 Spectral Line Analysis

There are a number of effects that can affect the shape and relative strength of atomic emission lines. Even for isolated atoms, a spectral line corresponding to an electronic transition cannot be observed as a perfectly defined frequency ω_0. In other words, the line cannot be described by the function $I\delta(\omega - \omega_0)$. There are several mechanisms that can produce spectral broadening, and they may divided into broadening from local conditions and broadening due to conditions of an extended region. Broadening from local conditions is due to effects in a small region near the emitter. By making the assumption that this small region is in local thermodynamic equilibrium (LTE), it is possible to estimate the plasma conditions near the emitting region. Initial fits through LTE analysis of line broadening and spectral line ratio were used to estimate the plasma conditions.

A consequence of the limited lifetime of an excited state results in natural broadening. The uncertainty principle $\Delta E \Delta\tau = h$ relates the lifetime of the state $\Delta\tau$ with the energy uncertainty ΔE. For example, the radiative decay rates of Cu Heα ($1s2p \rightarrow 1s^2$) and Heβ ($1s3p \rightarrow 1s^2$) are given by $\nu = 72.2 \times 10^{13}$ and 19.3×10^{13} Hz, respectively [146]. This results in natural linewidths of 3 (Heα) and 0.8 eV (Heβ). The corresponding natural lineshape is a Lorentzian function [147]. A further broadening mechanism is from spectroscopic instruments having finite resolution. This instrument broadening is related to their resolving power $E/\Delta E$. The

crystal spectrometers used for these experiments have instrument broadening with Gaussian linewidths. The combination of Lorentzian and Gaussian broadening leads to lineshapes known as Voigt profiles, which is a convolution of the Lorentzian and Gaussian lineshape.

6.3.1 Stark Broadening

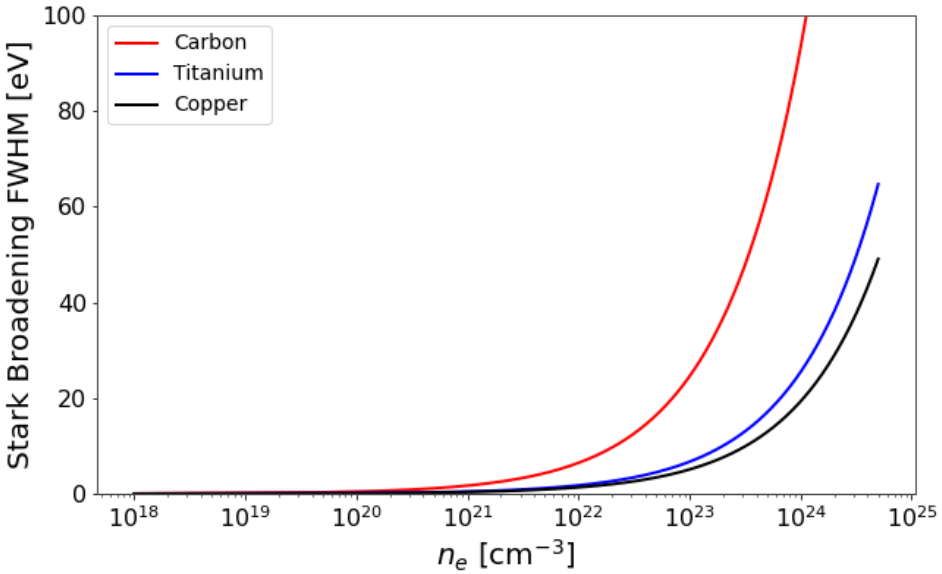

Figure 6.8: Calculated Stark broadening FWHM of the Heβ emission line ($1s3p \rightarrow 1s^2$) for helium-like carbon, titanium, and copper.

The local electric fields from free charges in near an emitting ion are capable of modifying the emission process. This effect, known as the Stark effect or Stark broadening [148], is determined by the local electric field intensity. When the emitters are in a dense plasma, this broadening mechanism also is known as pressure broadening. This broadening process strongly depends on the magnitude of the perturbation to the atomic Coulomb potential. This enables the determination of the density of charged particles in the plasma near the emitters. For Stark broadening of K-shell emission lines when the difference in energy levels

is even, e.g. $n = 3 \rightarrow n = 1$ or $n = 4 \rightarrow n = 2$, the Stark broadening FWHM is given by:

$$\delta\epsilon^S \approx 4.3\frac{n^2}{Z_{\text{nuc}}}(n_e[10^{22}\,\text{cm}^{-3}])^{0.58}, \tag{6.1}$$

where n is the upper energy level, Z_{nuc} is the atomic number, and n_e is the electron density. Calculated Stark broadening of the Heβ emission line for carbon ($Z_{\text{nuc}} = 6$), titanium ($Z_{\text{nuc}} = 22$), and copper ($Z_{\text{nuc}} = 29$) can be seen in Figure 6.8. There is a minimum density required for substantial Stark broadening to occur. For carbon this occurs around $n_e \approx 10^{21}$ cm^{-3}, whereas copper requires much higher density, $n_e \approx 10^{24}$ cm^{-3}.

6.3.2 Saha-Boltzmann Rate Balancing

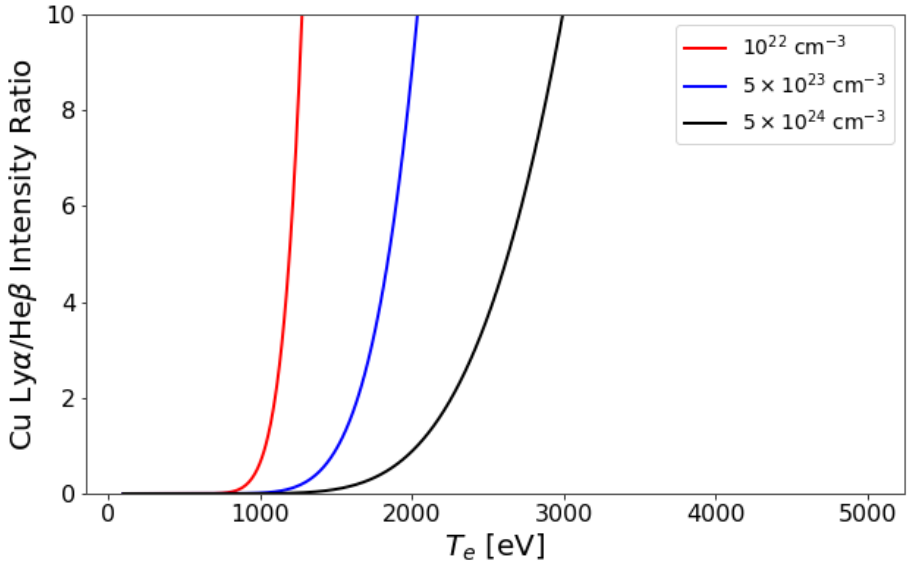

Figure 6.9: Calculated ratio of Cu Lyα to Heβ as a function of temperature for Cu plasma at various densities.

The populations of individual ionic species in the plasma directly effect the intensity of the species' emission lines. Ignoring any opacity effect, the largest populations will emit the strongest emission lines. When in LTE conditions, the populations of a species N in a

plasma are determined by the Saha Equation given by:.

$$\frac{N^{Z+1}}{N^{Z}} = \frac{g^{Z+1}}{g^{z}} \frac{6 \times 10^{21}}{n_e} T_e^{3/2} e^{-E_z^{\mathrm{ion}}/T_e}, \tag{6.2}$$

where N^Z and N^{Z+1} are the populations with ion charge Z and $Z+1$, g is their corresponding degeneracy factors, T_e is the electron temperature, and E_z^{ion} is the ionization potential required to ionize from state Z to $Z+1$. By assuming the intensity of line emission is directly proportional to the population of the species, the line intensity ratio can be used to determine the local electron temperature. Because different ionic species are present at different temperatures, the ratio of two individual lines depends strongly on both the temperature and density of the plasma as seen in Figure 6.9.

6.3.3 LTE Analysis of Experimental Data

Inital LTE analysis of 0.5 μm Cu targets are shown in Figure 6.10. Voigt profiles with the natural linewidths and instrument broadening ($\delta E \approx 8$ eV) are included with the fits to extract the Heβ FWHM and the ratio of Heβ to Lyα . The choice of Heβ over Heα is due to the increased opacity expected at these temperatures and densities. The individual fits of the single-shot spectra (red) are shown in blue with corresponding extracted temperatures and densities. The expected density of the 0.5 μm Cu foils is $n_e \approx 1-2\times10^{24}\,\mathrm{cm}^{-3}$ with electron temperatures of $T_e \approx 1.8$ keV. Assuming an average ionization state of He-like Cu due to the brightness of the He-like emission lines the calculated electron density is approximately the same as solid density $n_e = 2.3 \times 10^{24}\,\mathrm{cm}^{-3}$.

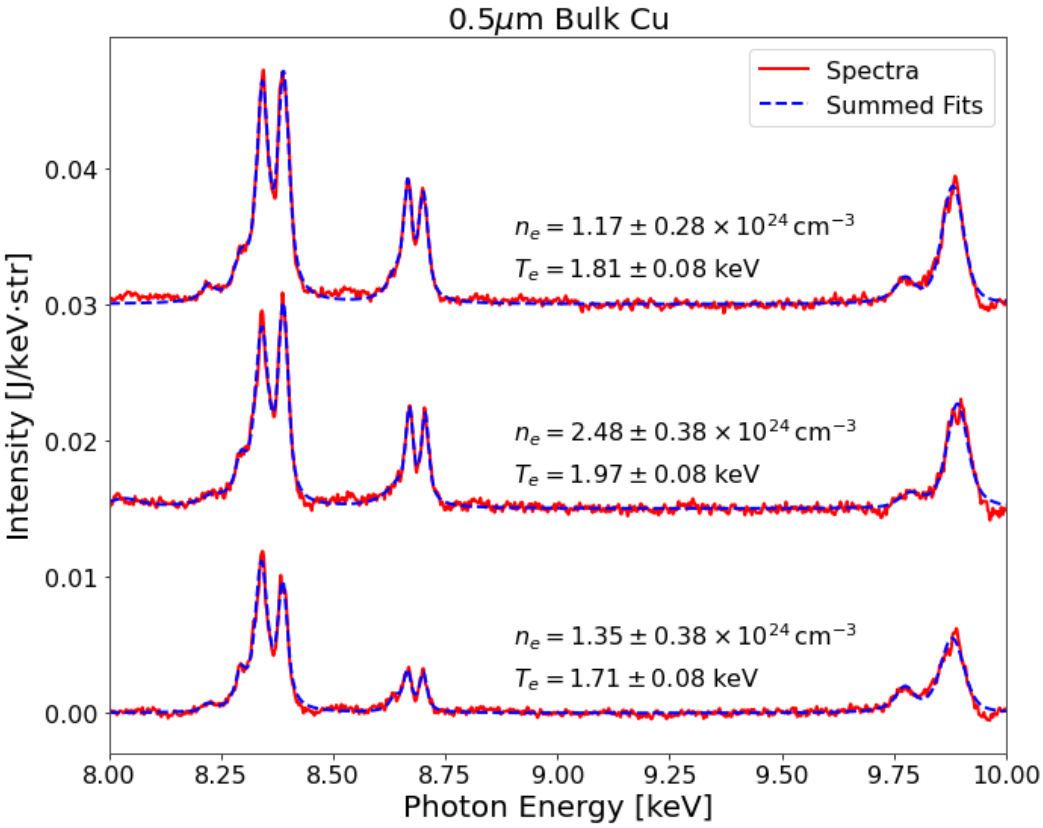

Figure 6.10: Calculated ratio of Cu Lyα to Heβ as a function of temperature for Cu plasma at various densities.

6.4 Simulation

Even with a large array of diagnostics capturing different aspects of the plasma emission, determining exact conditions inside the plasma remains a significant challenge. Therefore, simulations are required to help constrain the possible conditions. Therefore, simulations are required to help constrain the possible conditions. Collisional-radiative codes such as SCRAM [149] are a valuable resource for modeling plasmas in non-local thermodynamic equilibrium (non-LTE). Previously results have shown through comparisons with non-LTE collisional radiative codes that high-intensity, short-pulse lasers are capable of generating highly-ionized states of solid-density plasmas [61, 63, 64, 144, 150].

For the SCRAM modeling, solid density copper targets of thickness $dx = 0.1$ μm with an assumed equal electron and ion temperature $T_e = T_i = T$ from temperatures of 0.1 - 4 keV. The hot electron fraction in the solid target was estimated to be 10^{-4} informed from the conversion efficiency of Kα emission calculated from the x-ray spectra of 15 μm Cu foils, and is consistent with previous studies showing hot electron refluxing of longer pulse lasers at comparable intensities [65, 151]. Although the hot electrons dominate the production of cold Cu Kα , their number density is too small to have significant impact on ionization balance at solid densities and furthermore the SCRAM calculations are relatively insensitive to the hot electron temperature [152].

SCRAM simulations generated tables of emissivity (j) and absorptivity (κ) as a function of temperature and energy across 8 - 10 keV. These could then be used to calculate the optical depth, $\tau = -\kappa dx$, and self-emission intensity, $i = j/\kappa(1 - e^{-\tau})$ of the individual layers. With known lines-of-sight of the detectors, the transport of emission from the layers to detector can then be calculated. Figure 6.11 shows the calculated intensity, Figure 6.11a, and absorption, Figure 6.11b, of 0.5 μm thick copper foils with a constant temperature through the entire depth. The "simulated" detector is positioned on the front-side at an angle of 45° with

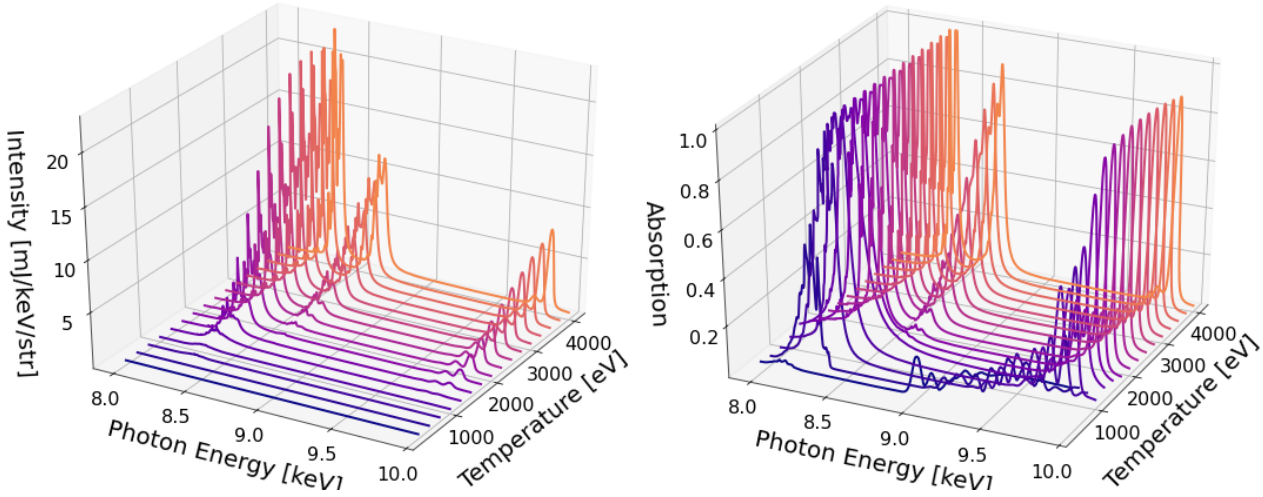

(a) Simulated Cu emission (b) Simulated Cu absorption

Figure 6.11: Simulated emission intensity (a) and absorption (b) from 0.5 μm thick Cu foil with constant ion density of 8.91 g/cm^3, i.e. solid-density copper. Temperatures ranged from 0.1 - 4 keV.

respect to target normal, which was the position of the von Hamos spectrometer during the experiment. An assumed emission time of 1 ps and emission spot size of 5 μm was used to convert to units of J/keV/str. In order for appreciable Lyα and Heβ emission to occur as observed in the experimental data, the bulk plasma temperature needs to exceed $T > 2$ keV. However, significant opacity can occur for much lower electron temperatures. Because He-like Cu can form a a closed electronic shell it is much harder to ionize He-like Cu immediately; the ionization energy required to produce Cu^{27+} (He-like Cu) is 2587 eV, whereas the ionization energy required to produce Cu^{28+} (H-like Cu) is 11062 eV [153]. By $T \simeq 1$ keV appreciable He-like copper is present in the plasma such that it has already become nearly opague to the Heα line.

A comparison between SCRAM modeling at various temperatures and experimental data can be seen in Figure 6.12, which shows experimental 0.5 and 1 μm foil front, Figure 6.12 a) and c), and rear, Figure 6.12 b) and d), spectra. To produce a better comparison, the SCRAM spectra for the front side emission has been convolved with instrument broadening of the von Hamos spectrometer ($E/\Delta E \sim 1000$). Since the high resolution spectrometer has

a much higher $E/\Delta E$ no convolution was performed to compare with the rear side data. The front and rear side Heα , Lyα , and Heβ emission can be simultaneously fit with constant temperatures through the entire plasma depth. The best temperature fit for the 0.5 µm foils is $T = 3.5$ keV, while the best fit for the 1 µm foils is lowered to $T = 3$ keV. This suggests that the thicker targets are being heated through the entire depth to temperatures $T_e \geq 3$ keV, and remain near solid density during the time of emission. The reduction in rear side emission compared to the front side spectra requires a region of hot, dense plasma with sufficient temperatures to produce He-like emission, without being hot enough for emission to occur.

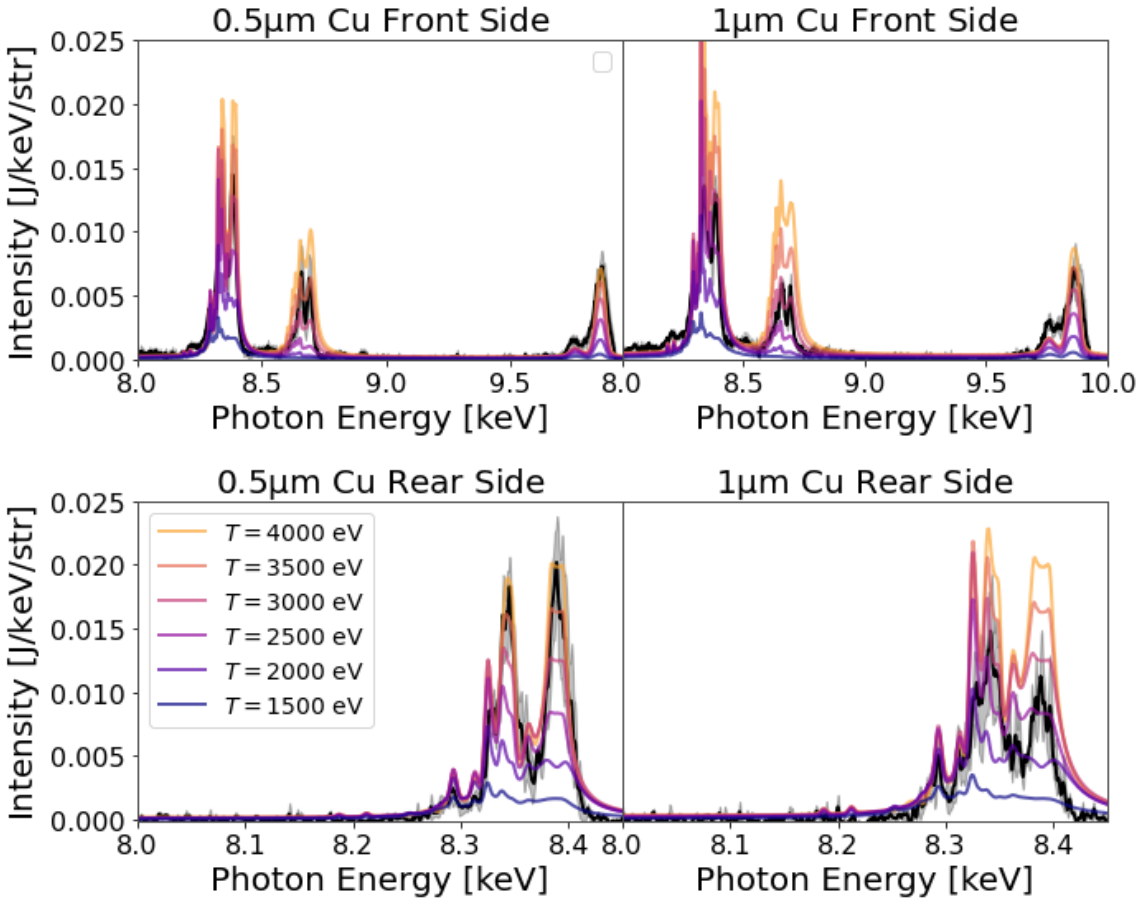

Figure 6.12: Experimental 0.5 µm and 1 µm Cu foil spectra (black) compared to SCRAM simulations with constant temperatures through the entire plasma depth. Shaded grey region indicates shot-to-shot standard deviation.

Fitting of thicker foil targets requires more complex temperature profiles. Figure 6.13 shows

experimental 2 μm and 5 μm Cu foil spectra compared to SCRAM simulations. Figure 6.13 a) has a reference 1 μm thick Cu spectrum, because no front side 2 μm data was acquired. 1 μm spectra is assumed to be comparable to 2 μm spectra by looking at differences in Figure 6.5 a). Various simulated electron temperature profiles, Figure 6.13 Inset, are plotted against the rear side emission spectra in Figure 6.13 b). In order to simultaneously fit front and rear-side emission, the temperature profile requires a region of high opacity for Heα and Lyα . Similarly, the front, 6.13 c), and rear side, 6.13 d), spectra for 5 μm Cu foils require variations in temperature as a function of depth.

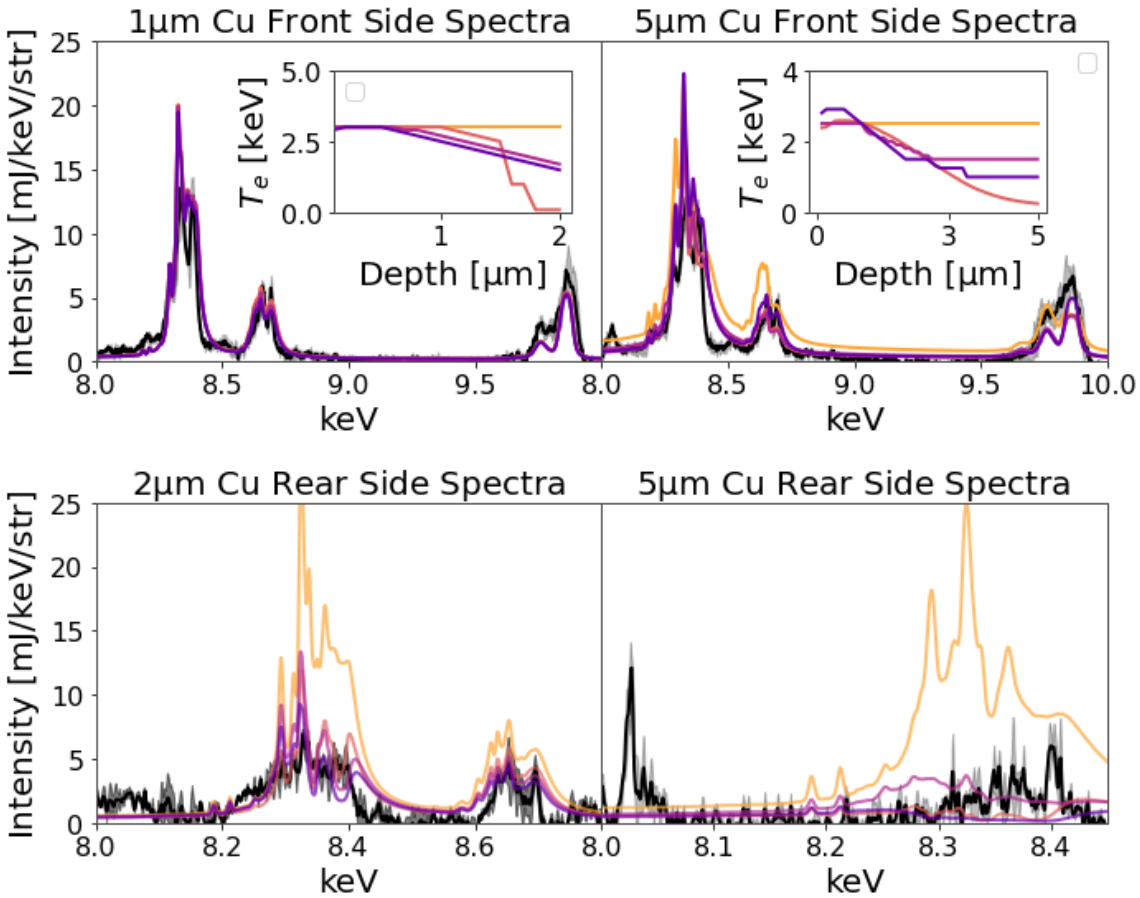

Figure 6.13: Experimental 2 μm and 5 μm Cu foil spectra (black) compared to SCRAM simulations. a) Reference 1 μm thick Cu spectrum. b) Rear side 2 μm thick Cu acquired by von Hamos spectrometer. Inset: Various simulated electron temperature T_e as a function of depth into the target.

Three-dimensional PIC simulations performed in VLPL for solid-density 5 μm thick Cu foil is presented in Figure 6.14. The simulations are initialized with singly ionized species of

solid-density Cu with a peak laser intensity of 5×10^{21} W/cm^2 . Due to the high-contrast of the ALEPH laser, no preplasma was assumed to form before the arrival of the main pulse. The laser focus is Gaussian with a 1.5 μm full-width at half-maximum. Ionization effects due to optical field ionization and electron-ion collisions are considered. Figure 6.14 presents an example of the plasma conditions at 430 fs after the peak of the laser pulse reaches the target. The calculated average electron temperatures (Figure 6.14 a) presents and electron density (Figure 6.14 b) in the center 2% of the target. The average electron temperature remains near 2.5 keV in the first 1 μm thickness of the target until dropping to below 0.5 keV at a depth of 5 μm . Figure 6.14 c) indicates that the ionization of highly-ionized charge states of Cu are predicted to propagates deep into the target. From the PIC simulations, the region of plasma with temperatures in the range of $1-2$ keV at a depth of 2-3 μm would have sufficiently high opacity to absorb the emission from the hotter from side as it propagates through the target, see Figure 6.11.

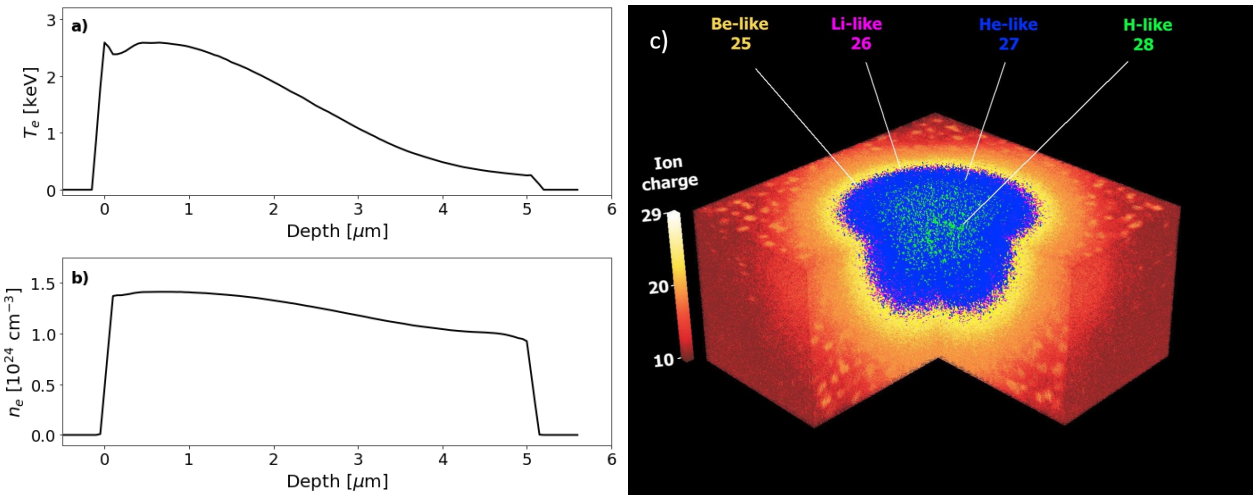

Figure 6.14: Three-dimensional PIC simulation for solid-density 5 μm Cu foil target. The target is irradiated at an intensity of 3×10^{21}W/cm^2 . The simulation snapshot is taken at time $t = 430$ fs after peak of the laser pulse reaches the target. a) Average values for electron temperature as a function of depth. b) Average charge state as a function of depth. c) 3D image of average ionization state. High degree of ionization observed to extend into the target. Simulations performed by Slava Shlyaptsev.

The heating observed in thinner targets appears to follow a different temperature profile.

Figure 6.15 shows the temperature, Figure 6.15 a), and density, Figure 6.15 b), as functions of depth for the different target thicknesses. It appears as though the 1 and 2 μm thick targets are uniformly heated to temperatures $T_e > 3$ keV and densities near solid density Cu. This contrasts with the 5 μm thick targets, which has a smoothly varying temperature profile from 2 keV near the surface that drops to $T_e < 500$ keV near the rear surface. This suggests that some transition in bulk heating is occurring between thin (≤ 2 μm) and thicker (≥ 5 μm) targets.

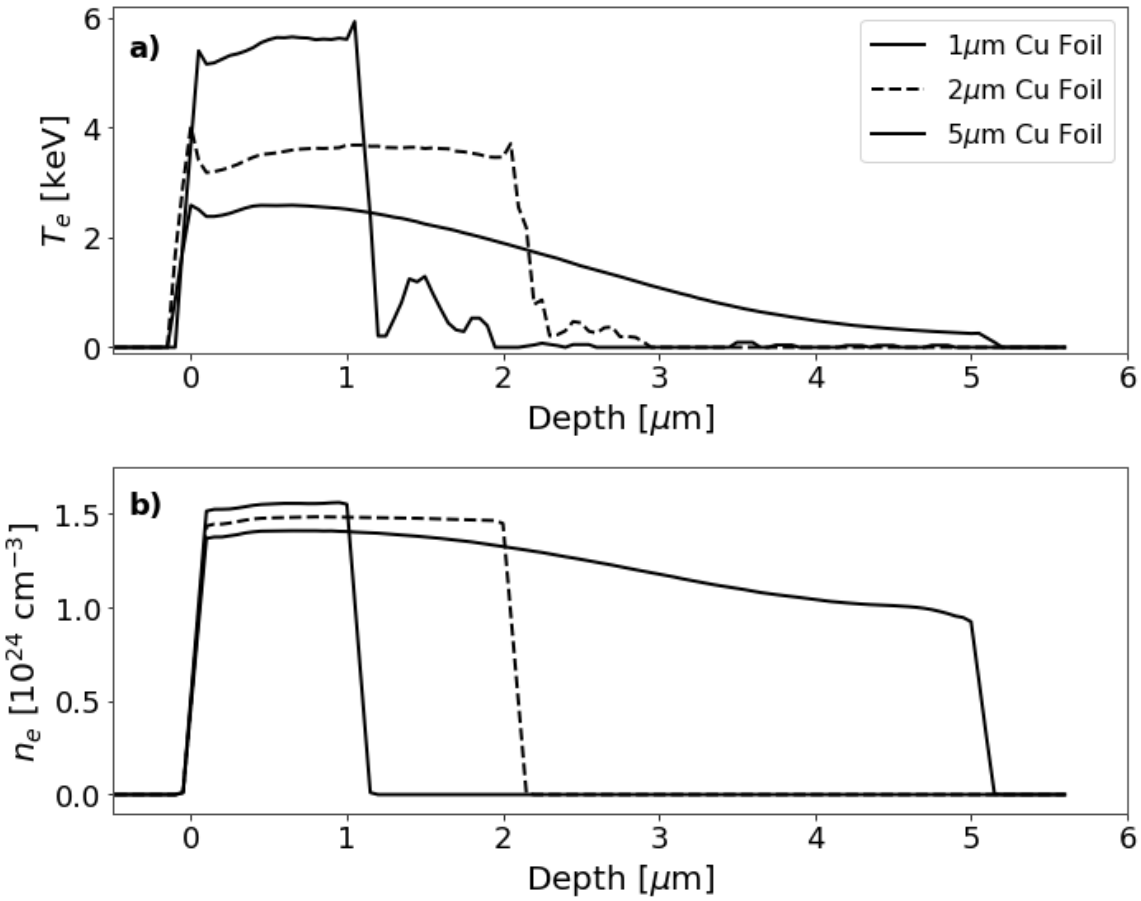

Figure 6.15: Three-dimensional PIC simulation for solid-density 1, 2, and 5 μm Cu foil targets.

6.5 Conclusion

Simultaneous front and rear-side x-ray measurements of Cu foils and buried layer targets irradiated at $I > 10^{21}$ W/cm^2 were taken at the ALEPH facility. Plasma temperatures were measured to exceed $T_e \geq 3$ keV for thin targets, with plasma densities remaining near solid-density. It was experimentally observed that a transition occurred for rear-side Cu x-ray emission as a function of target thickness. Considerable rear side Heα emission was observed for 0.5 and 1 μm thick Cu foils, while thicker targets had full absorption of the highly-ionized emission lines. A combination of PIC simulations and SCRAM modeling suggest that the thin foils experience a uniform heating through the entire depth, which does not occur for thicker targets. The utility in producing hot, uniformly-heated, solid-density plasmas through high-contrast, short-pulse lasers may be useful for the study of HED systems in future experiments.

The SCRAM modeling and PIC simulations represent a snapshot in time of the plasma conditions, whereas the experimental x-ray emission data is a time-integrated signal. Therefore, the difference in absolute values of temperature and density expected from SCRAM modeling and PIC simulations are expected, but there does appear to be a qualitative agreement between the two types of modeling. In future experiments, time-resolved data should be taken of either front or rear side emission to gain a better understanding of the emission times during the plasma lifetime. Furthermore, the rear side Lyα emission can be captured by adjustments to the high-resolution crystal geometry.

Chapter 7

Conclusion and Future Work

The progress of laser technology is reaching a point such that new laser systems are capable of generating relativistic intensities at high repetition rates with parameters spanning tabletop subterawatt to petawatt systems. New laser facilities are being constructed to allow multi-beam interactions at relativistic intensities. These systems and facilities present a paradigm shift in laser-plasma physics, where detailed studies can be performed by varying both laser and plasma parameters. For example, the Zettawatt-Equivalent Ultra-short pulse laser System (ZEUS) currently under construction at the University of Michigan Gerard Mourou Center for Ultrafast Optical Science will become one of the most intense laser systems in the world. ZEUS will have the unique capability of multi-beam, petawatt-class laser-solid experiments at high repetition rates. The High-Repetition-Rate Advanced Petawatt Laser System at Extreme Light Infrastructure (ELI) will deliver 30 J pulses in less than 30 fs with repetition rates up to 10 Hz. Finally, the proposed EP-OPAL at the Laboratory for Laser Energetics (LLE) would leverage the existing architecture of the OMEGA EP beamlines to produce two 25 PW beams driven by optical parametric amplification. Currently, a mid-scale version pumped by the Multi-Terrawatt laser (MTW-OPAL) is being constructed to produce 0.5 PW pulses delivered in 15 fs.

7.1 Two Color Relativistic Harmonic Generation

The investigation of two-color, relativistic harmonic generation represents a considerable experimental challenge. Significant theoretical studies have been undertaken to understand the physics of the relativistic HHG process, but to-date very little two-color experiments have been performed [126] due to their practical complexity. Circularly-polarized harmonics are proposed to be generated by two-color, collinear HHG when normally-incident on a target. This requires the use of two different-color beams such that counter-rotating fields can be focused onto a solid-density target. Developing bright circularly polarized sources from the ROM model would be exciting, as the technique would immediately be scalable to petawatt-class laser facilities. The first experiments could take place at UCI, where there exists a unique capability for non-commensurate wavelengths generated by OPA to be used in experiments, see Chapter 4. First, performed linear-polarized collinear experiments to observe the emission of non-commensurate harmonics expected from the interaction. Afterwards, colinear circularly-polarized experiments can be conducted to determine the applicability of the photon model to relativistic laser-plasma interactions.

Secondly, the introduction of a second, noncollinear beam in the high intensity laser-solid interactions can be explored. Studies using light generated from high intensity lasers contains some unique challenges. Traditional HHG experiments are performed such that the harmonic emission is collinear with the driving laser. This can cause problems for two reasons. The fundamental laser still contains considerable power after the interaction. This can cause damage to sensitive samples which prevents a long exposure series of a single target for attosecond dynamics. Secondly, in order to perform spectroscopic studies, the generated harmonics must then be spectrally separated through some diffractive element. The rejection of the fundamental can also be done using diffractive optics or rejector mirrors. But, these methods of harmonic selection and discrimination are extremely lossy, especially for higher order harmonic in the x-ray regime. Noncollinear harmonic generation is a method

to spatially separate the individual harmonics orders from their fundamental driving laser. The proposed experiment will attempt to determine the applicability of noncollinear geometries in the relativistic regime. It is unclear whether or not the photon model holds for the oscillating mirror model.

7.2 Novel Driving Laser Parameters

Laser-plasma interactions, due to their nature as nonlinear optical processes, are extremely intensity dependent. At UCI, we have access to optics that can shape the initial Gaussian profile of the laser to produce a flat top profile when focused. We can therefore study the differences between a flat-top intensity profile and Gaussian profile at the focus for high intensity laser-plasma experiments. The optics are also capable of generating different custom wavefronts, which can be used in a multitude of applications. Many simulations assume that there is a constant intensity profile at the focus, but this is not generally the case. One of the most significant differences between a flat-top and a Gaussian focal spot is through the ponderomotive force:

$$F_p \propto \nabla I. \tag{7.1}$$

The ponderomotive force is proportional to the gradient in the intensity profile of a laser, and acts to push charged particles away from regions of high intensity. A Gaussian has a very strong intensity variation across the beam profile, whereas an ideal flat-top profile has zero intensity variations across the focal spot.

7.3 Time-Resolved High Resolution X-ray Spectroscopy

The experimental results discussed in Chapter 6 as though short-pulse, high-contrast lasers are capable of generating solid-density plasmas with a uniform temperature profile. However, the experimental x-ray emission data is a time-integrated signal, which can produce misleading results as HED plasmas are highly-transient systems. Analysis of high-contrast experiments at intensities $\approx 10^{19}$ W/cm^2 have shown that the bulk electron temperature and density evolve quickly during the first 1 ps after the laser interaction [61]. In future experiments, time-resolved data should be taken of either front or rear side emission to gain a better understanding of the emission times during the plasma lifetime. Furthermore, the rear side Lyα emission can be captured by adjustments to the high-resolution crystal geometry. The deployment of electron spectrometers with sufficiently high signal-to-noise should be used to elucidate the hot electron heating mechanisms that take place during the interaction.

Bibliography

[1] G. Mourou and T. Tajima. Exploring fundamental physics at the highest-intensity-laser frontier | SPIE Homepage: SPIE.

[2] J. Schreiber, P. R. Bolton, and K. Parodi. Invited Review Article: "Hands-on" laser-driven ion acceleration: A primer for laser-driven source development and potential applications. *Review of Scientific Instruments*, 87(7):071101, July 2016. Publisher: American Institute of Physics.

[3] Yong Wang, Shoujun Wang, Alex Rockwood, Bradley M. Luther, Reed Hollinger, Alden Curtis, Chase Calvi, Carmen S. Menoni, and Jorge J. Rocca. 0.85 PW laser operation at 3.3 Hz and high-contrast ultrahigh-intensity second-harmonic beamline. *Optics Letters*, 42(19):3828–3831, October 2017. Publisher: Optical Society of America.

[4] D M Farinella. *Thin film compression toward the single-cycle regime for the advancement of high field.* Ph. D. Thesis, University of California, Irvine, 2018.

[5] B. L. Henke, E. M. Gullikson, and J. C. Davis. X-ray interactions: photoabsorption, scattering, transmission, and reflection at E=50-30000 eV, Z=1-92. In *Atomic Data and Nuclear Data Tables*, volume 54, pages 181–342. July 1993.

[6] N. Beier, T. Nguyen, J. Lin, J. Nees, K. Krushelnick, and F. Dollar. Relativistic short-pulse high harmonic generation at 1.3 and 2.1 micron wavelengths. *New Journal of Physics*, 21(4):043052, April 2019.

[7] T. H. Maiman. Stimulated Optical Radiation in Ruby. *Nature*, 187(4736):493, August 1960.

[8] P. A. Franken, A. E. Hill, C. W. Peters, and G. Weinreich. Generation of Optical Harmonics. *Physical Review Letters*, 7(4):118–119, August 1961.

[9] Donna Strickland and Gerard Mourou. Compression of amplified chirped optical pulses. *Opt. Commun*, pages 219–221, 1985.

[10] F. J. McClung and R. W. Hellwarth. Giant Optical Pulsations from Ruby. *Journal of Applied Physics*, 33(3):828–829, March 1962.

[11] Hans W. Mocker and R. J. Collins. Mode competition and self-locking effects in a q-switched ruby laser. *Applied Physics Letters*, 7(10):270–273, November 1965.

[12] A. J. DeMaria, D. A. Stetser, and H. Heynau. Self mode-locking of lasers with saturable absorbers. *Applied Physics Letters*, 8(7):174–176, April 1966. Publisher: American Institute of Physics.

[13] E. S. Bliss, D. R. Speck, J. F. Holzrichter, J. H. Erkkila, and A. J. Glass. Propagation of a high-intensity laser pulse with small-scale intensity modulation. *Applied Physics Letters*, 25(8):448–450, October 1974.

[14] G. Mourou. The ultrahigh-peak-power laser: present and future. *Applied Physics B*, 65(2):205–211, August 1997.

[15] T. Tajima and J. M. Dawson. Laser Electron Accelerator. *Physical Review Letters*, 43(4):267–270, July 1979.

[16] J. E. Murray and W. H. Lowdermilk. ND : YAG regenerative amplifier. *Journal of Applied Physics*, 51(7):3548–3556, July 1980.

[17] W. H. Lowdermilk and J. E. Murray. The multipass amplifier: Theory and numerical analysis. *Journal of Applied Physics*, 51(5):2436–2444, May 1980.

[18] Giulio Cerullo and Sandro De Silvestri. Ultrafast optical parametric amplifiers. *Review of Scientific Instruments*, 74(1):1–18, January 2003.

[19] V. Yanovsky, V. Chvykov, G. Kalinchenko, P. Rousseau, T. Planchon, T. Matsuoka, A. Maksimchuk, J. Nees, G. Cheriaux, G. Mourou, and K. Krushelnick. Ultra-high intensity- 300-TW laser at 0.1 Hz repetition rate. *Optics Express*, 16(3):2109–2114, February 2008.

[20] C. G. R. Geddes, Cs Toth, J. van Tilborg, E. Esarey, C. B. Schroeder, D. Bruhwiler, C. Nieter, J. Cary, and W. P. Leemans. High-quality electron beams from a laser wakefield accelerator using plasma-channel guiding. *Nature*, 431(7008):538–541, September 2004.

[21] E. L. Clark, K. Krushelnick, J. R. Davies, M. Zepf, M. Tatarakis, F. N. Beg, A. Machacek, P. A. Norreys, M. I. K. Santala, I. Watts, and A. E. Dangor. Measurements of Energetic Proton Transport through Magnetized Plasma from Intense Laser Interactions with Solids. *Physical Review Letters*, 84(4):670–673, January 2000.

[22] F. Dollar, C. Zulick, T. Matsuoka, C. McGuffey, S. S. Bulanov, V. Chvykov, J. Davis, G. Kalinchenko, G. M. Petrov, and L. Willingale. High contrast ion acceleration at intensities exceeding 10 21 W cm- 2. *Physics of Plasmas*, 20(5):056703, 2013.

[23] Roland Lichters, J. Meyer-ter Vehn, and A. Pukhov. Short-pulse laser harmonics from oscillating plasma surfaces driven at relativistic intensity. *Physics of Plasmas*, 3(9):3425–3437, 1996.

[24] B. Dromey, M. Zepf, A. Gopal, K. Lancaster, M. S. Wei, K. Krushelnick, M. Tatarakis, N. Vakakis, S. Moustaizis, and R. Kodama. High harmonic generation in the relativistic limit. *Nature Physics*, 2(7):456, 2006.

[25] Sterling Backus, Charles G. Durfee, Gerard Mourou, Henry C. Kapteyn, and Margaret M. Murnane. 0.2-TW laser system at 1 kHz. *Optics Letters*, 22(16):1256–1258, August 1997.

[26] O. Albert, H. Wang, D. Liu, Z. Chang, and G. Mourou. Generation of relativistic intensity pulses at a kilohertz repetition rate. *Optics Letters*, 25(15):1125–1127, August 2000.

[27] N. M. Naumova, J. A. Nees, I. V. Sokolov, B. Hou, and G. A. Mourou. Relativistic Generation of Isolated Attosecond Pulses in a ${\ensuremath{\lambda}}^{3}$ Focal Volume. *Physical Review Letters*, 92(6):063902, February 2004.

[28] J. Faure, D. Gustas, D. Guénot, A. Vernier, F. Böhle, M. Ouillé, S. Haessler, R. Lopez-Martens, and A. Lifschitz. A review of recent progress on laser-plasma acceleration at kHz repetition rate. *Plasma Physics and Controlled Fusion*, 61(1):014012, November 2018.

[29] Jinpu Lin, James H. Easter, Karl Krushelnick, Mark Mathis, Jian Dong, A. G. R. Thomas, and John Nees. Focus optimization at relativistic intensity with high numerical aperture and adaptive optics. *Optics Communications*, 421:79–82, August 2018.

[30] J. Lin, Y. Ma, R. Schwartz, D. Woodbury, J. A. Nees, M. Mathis, A. G. R. Thomas, K. Krushelnick, and H. Milchberg. Adaptive control of laser-wakefield accelerators driven by mid-IR laser pulses. *Optics Express*, 27(8):10912–10923, April 2019. Publisher: Optical Society of America.

[31] W. L. Kruer and Kent Estabrook. J×B heating by very intense laser light. *The Physics of Fluids*, 28(1):430–432, January 1985.

[32] S. C. Wilks, W. L. Kruer, M. Tabak, and A. B. Langdon. Absorption of ultra-intense laser pulses. *Physical Review Letters*, 69(9):1383–1386, August 1992. Publisher: American Physical Society.

[33] F. N. Beg, A. R. Bell, A. E. Dangor, C. N. Danson, A. P. Fews, M. E. Glinsky, B. A. Hammel, P. Lee, P. A. Norreys, and Ma Tatarakis. A study of picosecond laser–solid interactions up to 1019 W cm- 2. *Physics of plasmas*, 4(2):447–457, 1997.

[34] Yun-Qian Cui, Wei-Min Wang, Zheng-Ming Sheng, Yu-Tong Li, and Jie Zhang. Laser absorption and hot electron temperature scalings in laser–plasma interactions. *Plasma Physics and Controlled Fusion*, 55(8):085008, June 2013. Publisher: IOP Publishing.

[35] Xiaomei Zhang, Toshiki Tajima, Deano Farinella, Youngmin Shin, Gerard Mourou, Jonathan Wheeler, Peter Taborek, Pisin Chen, Franklin Dollar, and Baifei Shen. Particle-in-cell simulation of x-ray wakefield acceleration and betatron radiation in nanotubes. *Physical Review Accelerators and Beams*, 19(10):101004, October 2016.

[36] Sahel Hakimi, Tam Nguyen, Deano Farinella, Calvin K. Lau, Hsuan-Yu Wang, Peter Taborek, Franklin Dollar, and Toshiki Tajima. Wakefield in solid state plasma with the ionic lattice force. *Physics of Plasmas*, 25(2):023112, February 2018.

[37] Guibao Xu, Scott F. Wandel, and Igor Jovanovic. Nondegenerate parametric generation of 2.2mJ few-cycle 2.05-micron pulses using a mixed phase matching scheme. *Review of Scientific Instruments*, 85(2):023102, February 2014.

[38] R. L. Carman, D. W. Forslund, and J. M. Kindel. Visible Harmonic Emission as a Way of Measuring Profile Steepening. *Physical Review Letters*, 46(1):29–32, January 1981.

[39] S. V. Bulanov, N. M. Naumova, and F. Pegoraro. Interaction of an ultrashort, relativistically strong laser pulse with an overdense plasma. *Physics of Plasmas*, 1(3):745–757, March 1994.

[40] D. Von der Linde, T. Engers, G. Jenke, P. Agostini, G. Grillon, E. Nibbering, A. Mysyrowicz, and A. Antonetti. Generation of high-order harmonics from solid surfaces by intense femtosecond laser pulses. *Physical Review A*, 52(1):R25, 1995.

[41] Paul Gibbon. Harmonic generation by femtosecond laser-solid interaction: A coherent "water-window" light source? *Physical Review Letters*, 76(1):50, 1996.

[42] S. Gordienko, A. Pukhov, O. Shorokhov, and T. Baeva. Relativistic Doppler effect: Universal spectra and zeptosecond pulses. *Physical Review Letters*, 93(11):115002, 2004.

[43] Natalia M. Naumova, John A. Nees, and Gérard A. Mourou. Relativistic attosecond physics. *Physics of Plasmas*, 12(5):056707, April 2005.

[44] G. Mourou, S. Mironov, E. Khazanov, and A. Sergeev. Single cycle thin film compressor opening the door to Zeptosecond-Exawatt physics. *The European Physical Journal Special Topics*, 223(6):1181–1188, May 2014.

[45] Bruce A. Remington, R. Paul Drake, and Dmitri D. Ryutov. Experimental astrophysics with high power lasers and Z pinches. *Reviews of Modern Physics*, 78(3):755–807, August 2006. Publisher: American Physical Society.

[46] J. E. Bailey, G. A. Rochau, R. C. Mancini, C. A. Iglesias, J. J. MacFarlane, I. E. Golovkin, C. Blancard, Ph. Cosse, and G. Faussurier. Experimental investigation of opacity models for stellar interior, inertial fusion, and high energy density plasmas. *Physics of Plasmas*, 16(5):058101, May 2009. Publisher: American Institute of Physics.

[47] T. Nagayama, J. E. Bailey, G. P. Loisel, G. S. Dunham, G. A. Rochau, C. Blancard, J. Colgan, Ph. Cossé, G. Faussurier, C. J. Fontes, F. Gilleron, S. B. Hansen, C. A. Iglesias, I. E. Golovkin, D. P. Kilcrease, J. J. MacFarlane, R. C. Mancini, R. M. More, C. Orban, J.-C. Pain, M. E. Sherrill, and B. G. Wilson. Systematic Study of L-Shell Opacity at Stellar Interior Temperatures. *Physical Review Letters*, 122(23):235001, June 2019. Publisher: American Physical Society.

[48] John D. Lindl, Peter Amendt, Richard L. Berger, S. Gail Glendinning, Siegfried H. Glenzer, Steven W. Haan, Robert L. Kauffman, Otto L. Landen, and Laurence J. Suter. The physics basis for ignition using indirect-drive targets on the National Ignition Facility. *Physics of Plasmas*, 11(2):339–491, February 2004. Publisher: American Institute of Physics.

[49] M. H. Key. Status of and prospects for the fast ignition inertial fusion concept. *Physics of Plasmas*, 14(5):055502, May 2007. Publisher: American Institute of Physics.

[50] R. Betti and O. A. Hurricane. Inertial-confinement fusion with lasers. *Nature Physics*, 12(5):435–448, May 2016. Bandiera_abtest: a Cg_type: Nature Research Journals Number: 5 Primary_atype: Reviews Publisher: Nature Publishing Group Subject_term: Experimental nuclear physics;Laser-produced plasmas;Nuclear physics;Plasma physics Subject_term_id: experimental-nuclear-physics;laser-produced-plasmas;nuclear-physics;plasma-physics.

[51] J. R. Davies. Electric and magnetic field generation and target heating by laser-generated fast electrons. *Physical Review E*, 68(5):056404, November 2003. Publisher: American Physical Society.

[52] S. B. Hansen, E. C. Harding, P. F. Knapp, M. R. Gomez, T. Nagayama, and J. E. Bailey. Fluorescence and absorption spectroscopy for warm dense matter studies and ICF plasma diagnostics. *Physics of Plasmas*, 25(5):056301, March 2018. Publisher: American Institute of Physics.

[53] K. Yasuike, M. H. Key, S. P. Hatchett, R. A. Snavely, and K. B. Wharton. Hot electron diagnostic in a solid laser target by K-shell lines measurement from ultraintense laser–plasma interactions (3×1020 W/cm2,$\leq$400 J). *Review of Scientific Instruments*, 72(1):1236–1240, January 2001.

[54] G. Gregori, S. B. Hansen, R. Clarke, R. Heathcote, M. H. Key, J. King, R. I. Klein, N. Izumi, A. J. Mackinnon, S. J. Moon, H.-S. Park, J. Pasley, N. Patel, P. K. Patel, B. A. Remington, D. D. Ryutov, R. Shepherd, R. A. Snavely, S. C. Wilks, B. B. Zhang, and S. H. Glenzer. Experimental Characterization of a Strongly Coupled Solid Density Plasma Generated in a Short-pulse Laser Target Interaction. *Contributions to Plasma Physics*, 45(3-4):284–292, July 2005.

[55] W. Theobald, K. Akli, R. Clarke, J. A. Delettrez, R. R. Freeman, S. Glenzer, J. Green, G. Gregori, R. Heathcote, N. Izumi, J. A. King, J. A. Koch, J. Kuba, K. Lancaster, A. J. MacKinnon, M. Key, C. Mileham, J. Myatt, D. Neely, P. A. Norreys, H.-S. Park, J. Pasley, P. Patel, S. P. Regan, H. Sawada, R. Shepherd, R. Snavely, R. B. Stephens, C. Stoeckl, M. Storm, B. Zhang, and T. C. Sangster. Hot surface ionic line emission and cold K-inner shell emission from petawatt-laser-irradiated Cu foil targets. *Physics of Plasmas*, 13(4):043102, April 2006.

[56] K. U. Akli, M. H. Key, H. K. Chung, S. B. Hansen, R. R. Freeman, M. H. Chen, G. Gregori, S. Hatchett, D. Hey, N. Izumi, J. King, J. Kuba, P. Norreys, A. J. Mackinnon,

C. D. Murphy, R. Snavely, R. B. Stephens, C. Stoeckel, W. Theobald, and B. Zhang. Temperature sensitivity of Cu Kα imaging efficiency using a spherical Bragg reflecting crystal. *Physics of Plasmas*, 14(2):023102, February 2007. Publisher: American Institute of Physics.

[57] P. M. Nilson, W. Theobald, J. F. Myatt, C. Stoeckl, M. Storm, J. D. Zuegel, R. Betti, D. D. Meyerhofer, and T. C. Sangster. Bulk heating of solid-density plasmas during high-intensity-laser plasma interactions. *Physical Review E*, 79(1):016406, January 2009.

[58] C. M. Huntington, C. C. Kuranz, G. Malamud, R. P. Drake, H.-S. Park, and B. R. Maddox. Spectral analysis of x-ray emission created by intense laser irradiation of copper materialsa). *Review of Scientific Instruments*, 83(10):10E114, October 2012.

[59] P. Palmeri, G. Boutoux, D. Batani, and P. Quinet. Effects of target heating on experiments using $K\alpha$ and $K\beta$ diagnostics. *Physical Review E*, 92(3):033108, September 2015.

[60] I. Y. Skobelev, S. N. Ryazantsev, D. D. Arich, P. S. Bratchenko, A. Y. Faenov, T. A. Pikuz, P. Durey, L. Doehl, D. Farley, C. D. Baird, K. L. Lancaster, C. D. Murphy, N. Booth, C. Spindloe, P. McKenna, S. B. Hansen, J. Colgan, R. Kodama, N. Woolsey, and S. A. Pikuz. X-ray absorption spectroscopy study of energy transport in foil targets heated by petawatt laser pulses. *Photonics Research*, 6(4):234–237, April 2018. Publisher: Optical Society of America.

[61] O. N. Rosmej, Z. Samsonova, S. Höfer, D. Kartashov, C. Arda, D. Khaghani, A. Schoenlein, S. Zähter, A. Hoffmann, R. Loetzsch, A. Saevert, I. Uschmann, M. E. Povarnitsyn, N. E. Andreev, L. P. Pugachev, M. C. Kaluza, and C. Spielmann. Generation of keV hot near-solid density plasma states at high contrast laser-matter interaction. *Physics of Plasmas*, 25(8):083103, July 2018. Publisher: American Institute of Physics.

[62] Hui Chen, M. Bitter, K. W. Hill, S. Kerr, E. Magee, S. R. Nagel, J. Park, M. B. Schneider, G. Stone, G. J. Williams, and P. Beiersdorfer. A high-resolution imaging x-ray crystal spectrometer for high energy density plasmas. *Review of Scientific Instruments*, 85(11):11E606, November 2014.

[63] R. Hollinger, S. Wang, Y. Wang, A. Moreau, M. G. Capeluto, H. Song, A. Rockwood, E. Bayarsaikhan, V. Kaymak, A. Pukhov, V. N. Shlyaptsev, and J. J. Rocca. Extreme ionization of heavy atoms in solid-density plasmas by relativistic second-harmonic laser pulses. *Nature Photonics*, 14(10):607–611, October 2020. Number: 10 Publisher: Nature Publishing Group.

[64] B. F. Kraus, A. Chien, Lan Gao, K. W. Hill, M. Bitter, P. C. Efthimion, Hui Chen, M. B. Schneider, A. Moreau, R. Hollinger, Shoujun Wang, Huanyu Song, and J. J. Rocca. Comparing plasma conditions in short-pulse-heated foils via fine-structure x-ray emission. *Review of Scientific Instruments*, 92(3):033525, March 2021. Publisher: American Institute of Physics.

[65] J. Myatt, W. Theobald, J. A. Delettrez, C. Stoeckl, M. Storm, T. C. Sangster, A. V. Maximov, and R. W. Short. High-intensity laser interactions with mass-limited solid targets and implications for fast-ignition experiments on OMEGA EP. *Physics of Plasmas*, 14(5):056301, March 2007. Publisher: American Institute of Physics.

[66] Ahmed H. Zewail. Femtochemistry: Atomic-Scale Dynamics of the Chemical Bond. *The Journal of Physical Chemistry A*, 104(24):5660–5694, June 2000.

[67] Daniel B. Durham, Fabrizio Riminucci, Filippo Ciabattini, Andrea Mostacci, Andrew M. Minor, Stefano Cabrini, and Daniele Filippetto. Plasmonic Lenses for Tunable Ultrafast Electron Emitters at the Nanoscale. *Physical Review Applied*, 12(5):054057, November 2019.

[68] A. E. Hussein, N. Senabulya, Y. Ma, M. J. V. Streeter, B. Kettle, S. J. D. Dann, F. Albert, N. Bourgeois, S. Cipiccia, J. M. Cole, O. Finlay, E. Gerstmayr, I. Gallardo González, A. Higginbotham, D. A. Jaroszynski, K. Falk, K. Krushelnick, N. Lemos, N. C. Lopes, C. Lumsdon, O. Lundh, S. P. D. Mangles, Z. Najmudin, P. P. Rajeev, C. M. Schlepütz, M. Shahzad, M. Smid, R. Spesyvtsev, D. R. Symes, G. Vieux, L. Willingale, J. C. Wood, A. J. Shahani, and A. G. R. Thomas. Laser-wakefield accelerators for high-resolution X-ray imaging of complex microstructures. *Scientific Reports*, 9(1):1–13, March 2019.

[69] T. B. Norris, K. Kim, J. Urayama, Z. K. Wu, J. Singh, and P. K. Bhattacharya. Density and temperature dependence of carrier dynamics in self-organized InGaAs quantum dots. *Journal of Physics D: Applied Physics*, 38(13):2077–2087, June 2005.

[70] Zewei Shao, Xun Cao, Hongjie Luo, and Ping Jin. Recent progress in the phase-transition mechanism and modulation of vanadium dioxide materials. *NPG Asia Materials*, 10(7):581, July 2018.

[71] N. Böwering, T. Lischke, B. Schmidtke, N. Müller, T. Khalil, and U. Heinzmann. Asymmetry in Photoelectron Emission from Chiral Molecules Induced by Circularly Polarized Light. *Physical Review Letters*, 86(7):1187–1190, February 2001. Publisher: American Physical Society.

[72] G. Schütz, M. Knülle, and H. Ebert. Magnetic circular x-ray dichroism and its relation to local moments. *Physica Scripta*, T49A:302–306, January 1993. Publisher: IOP Publishing.

[73] P. Emma, R. Akre, J. Arthur, R. Bionta, C. Bostedt, J. Bozek, A. Brachmann, P. Bucksbaum, R. Coffee, F.-J. Decker, Y. Ding, D. Dowell, S. Edstrom, A. Fisher, J. Frisch, S. Gilevich, J. Hastings, G. Hays, Ph Hering, Z. Huang, R. Iverson, H. Loos, M. Messerschmidt, A. Miahnahri, S. Moeller, H.-D. Nuhn, G. Pile, D. Ratner, J. Rzepiela, D. Schultz, T. Smith, P. Stefan, H. Tompkins, J. Turner, J. Welch, W. White, J. Wu, G. Yocky, and J. Galayda. First lasing and operation of an ångstrom-wavelength free-electron laser. *Nature Photonics*, 4(9):641–647, September 2010. Bandiera_abtest: a Cg_type: Nature Research Journals Number: 9 Primary_atype:

Research Publisher: Nature Publishing Group Subject_term: Free-electron lasers;X-rays Subject_term_id: free-electron-lasers;x-rays.

[74] M. Hentschel, R. Kienberger, Ch Spielmann, G. A. Reider, N. Milosevic, T. Brabec, P. Corkum, U. Heinzmann, M. Drescher, and F. Krausz. Attosecond metrology. *Nature*, 414(6863):509–513, November 2001.

[75] P. B. Corkum and Ferenc Krausz. Attosecond science. *Nature Physics*, 3(6):381, June 2007.

[76] P. Tzallas, E. Skantzakis, L. a. A. Nikolopoulos, G. D. Tsakiris, and D. Charalambidis. Extreme-ultraviolet pump–probe studies of one-femtosecond-scale electron dynamics. *Nature Physics*, 7(10):781–784, October 2011. Number: 10 Publisher: Nature Publishing Group.

[77] Francesca Calegari, Giuseppe Sansone, Salvatore Stagira, Caterina Vozzi, and Mauro Nisoli. Advances in attosecond science. *Journal of Physics B: Atomic, Molecular and Optical Physics*, 49(6):062001, February 2016. Publisher: IOP Publishing.

[78] Dennis F. Gardner, Michael Tanksalvala, Elisabeth R. Shanblatt, Xiaoshi Zhang, Benjamin R. Galloway, Christina L. Porter, Robert Karl Jr, Charles Bevis, Daniel E. Adams, and Henry C. Kapteyn. Subwavelength coherent imaging of periodic samples using a 13.5 nm tabletop high-harmonic light source. *Nature Photonics*, 11(4):259, 2017.

[79] Aurélie Jullien, Jean-Philippe Rousseau, Brigitte Mercier, Laura Antonucci, Olivier Albert, Gilles Chériaux, Stoyan Kourtev, Nikolai Minkovski, and Solomon M. Saltiel. Highly efficient nonlinear filter for femtosecond pulse contrast enhancement and pulse shortening. *Optics Letters*, 33(20):2353–2355, October 2008.

[80] Ch. Ziener, P. S. Foster, E. J. Divall, C. J. Hooker, M. H. R. Hutchinson, A. J. Langley, and D. Neely. Specular reflectivity of plasma mirrors as a function of intensity, pulse duration, and angle of incidence. *Journal of Applied Physics*, 93(1):768–770, December 2002.

[81] P. Gibbon. *Short pulse laser interactions with matter*. Imperial College Press, London, 2005.

[82] Brice Quesnel and Patrick Mora. Theory and simulation of the interaction of ultraintense laser pulses with electrons in vacuum. *Physical Review E*, 58(3):3719–3732, September 1998.

[83] A. Einstein. Über einen die Erzeugung und Verwandlung des Lichtes betreffenden heuristischen Gesichtspunkt. *Annalen der Physik*, 322(6):132–148, 1905.

[84] L. V. Keldysh. Ionization in the field of a strong electromagnetic wave. *Zh. Eksperim. i Teor. Fiz.*, Vol: 47, November 1964.

[85] N. B. Delone and Vladimir P. Krainov. Tunneling and barrier-suppression ionization of atoms and ions in a laser radiation field. *Physics-Uspekhi*, 41(5):469, 1998.

[86] P. Mora. Plasma Expansion into a Vacuum. *Physical Review Letters*, 90(18):185002, May 2003.

[87] S. K. Mishra, A. Andreev, and M. P. Kalashinikov. Reflection of few cycle laser pulses from an inhomogeneous overdense plasma. *Optics Express*, 25(10):11637–11651, May 2017. Publisher: Optical Society of America.

[88] M. Zepf, G. D. Tsakiris, G. Pretzler, I. Watts, D. M. Chambers, P. A. Norreys, U. Andiel, A. E. Dangor, K. Eidmann, C. Gahn, A. Machacek, J. S. Wark, and K. Witte. Role of the plasma scale length in the harmonic generation from solid targets. *Physical Review E*, 58(5):R5253–R5256, November 1998.

[89] M. Behmke, D. an der Brügge, C. Rödel, M. Cerchez, D. Hemmers, M. Heyer, O. Jäckel, M. Kübel, G. G. Paulus, G. Pretzler, A. Pukhov, M. Toncian, T. Toncian, and O. Willi. Controlling the Spacing of Attosecond Pulse Trains from Relativistic Surface Plasmas. *Physical Review Letters*, 106(18):185002, May 2011. Publisher: American Physical Society.

[90] F. Dollar, P. Cummings, V. Chvykov, L. Willingale, M. Vargas, V. Yanovsky, C. Zulick, A. Maksimchuk, A. G. R. Thomas, and K. Krushelnick. Scaling High-Order Harmonic Generation from Laser-Solid Interactions to Ultrahigh Intensity. *Physical Review Letters*, 110(17):175002, April 2013.

[91] R. Fedosejevs, M. D. J. Burgess, G. D. Enright, and M. C. Richardson. Supercritical Density Profiles of C${\mathrm{O}}_{2}$-Laser-Irradiated Microballoons. *Physical Review Letters*, 43(22):1664–1667, November 1979.

[92] J. P. Freidberg, R. W. Mitchell, R. L. Morse, and L. I. Rudsinski. Resonant Absorption of Laser Light by Plasma Targets. *Physical Review Letters*, 28(13):795–799, March 1972. Publisher: American Physical Society.

[93] D. W. Forslund, J. M. Kindel, Kenneth Lee, E. L. Lindman, and R. L. Morse. Theory and simulation of resonant absorption in a hot plasma. *Physical Review A*, 11(2):679–683, February 1975. Publisher: American Physical Society.

[94] James Albritton and Paul Koch. Cold plasma wavebreaking: Production of energetic electrons. *The Physics of Fluids*, 18(9):1136–1139, September 1975. Publisher: American Institute of Physics.

[95] F. Brunel. Not-so-resonant, resonant absorption. *Physical Review Letters*, 59(1):52–55, July 1987.

[96] K. W. Hill, M. Bitter, L. Delgado-Aparacio, P. Efthimion, N. A. Pablant, J. Lu, P. Beiersdorfer, H. Chen, and E. Magee. Characterization of spatially resolved high

resolution x-ray spectrometers for high energy density physics and light source experiments. *Review of Scientific Instruments*, 85(11):11D612, July 2014. Publisher: American Institute of Physics.

[97] T. Tajima. Laser acceleration in novel media. *The European Physical Journal Special Topics*, 223(6):1037–1044, May 2014.

[98] F. Quéré, C. Thaury, P. Monot, S. Dobosz, Ph. Martin, J.-P. Geindre, and P. Audebert. Coherent Wake Emission of High-Order Harmonics from Overdense Plasmas. *Physical Review Letters*, 96(12):125004, March 2006.

[99] D. Von der Linde and K. Rzazewski. High-order optical harmonic generation from solid surfaces. *Applied Physics B*, 63(5):499–506, 1996.

[100] T. Baeva, S. Gordienko, and A. Pukhov. Theory of high-order harmonic generation in relativistic laser interaction with overdense plasma. *Physical review E*, 74(4):046404, 2006.

[101] Alexander Tarasevitch, Konstantin Lobov, Clemens Wünsche, and Dietrich von der Linde. Transition to the Relativistic Regime in High Order Harmonic Generation. *Physical Review Letters*, 98(10):103902, March 2007.

[102] C. Thaury and F. Quéré. High-order harmonic and attosecond pulse generation on plasma mirrors: basic mechanisms. *Journal of Physics B: Atomic, Molecular and Optical Physics*, 43(21):213001, October 2010.

[103] U. Teubner and P. Gibbon. High-order harmonics from laser-irradiated plasma surfaces. *Reviews of Modern Physics*, 81(2):445–479, April 2009.

[104] C. Rödel, D. an der Brügge, J. Bierbach, M. Yeung, T. Hahn, B. Dromey, S. Herzer, S. Fuchs, A. Galestian Pour, E. Eckner, M. Behmke, M. Cerchez, O. Jäckel, D. Hemmers, T. Toncian, M. C. Kaluza, A. Belyanin, G. Pretzler, O. Willi, A. Pukhov, M. Zepf, and G. G. Paulus. Harmonic Generation from Relativistic Plasma Surfaces in Ultrasteep Plasma Density Gradients. *Physical Review Letters*, 109(12):125002, September 2012.

[105] Julian Schwinger. On Gauge Invariance and Vacuum Polarization. *Physical Review*, 82(5):664–679, June 1951. Publisher: American Physical Society.

[106] S. Gordienko, A. Pukhov, O. Shorokhov, and T. Baeva. Coherent focusing of high harmonics: A new way towards the extreme intensities. *Physical review letters*, 94(10):103903, 2005.

[107] Rick Trebino, Kenneth W. DeLong, David N. Fittinghoff, John N. Sweetser, Marco A. Krumbügel, Bruce A. Richman, and Daniel J. Kane. Measuring ultrashort laser pulses in the time-frequency domain using frequency-resolved optical gating. *Review of Scientific Instruments*, 68(9):3277–3295, September 1997.

[108] S. Hakimi. *Exploring novel concepts of x-ray radiation generation.* Ph. D. Thesis, University of California, Irvine, 2020.

[109] Jeffrey A. Koch, Otto L. Landen, Troy W. Barbee, Peter Celliers, Luiz B. Da Silva, Sharon G. Glendinning, Bruce A. Hammel, Dan H. Kalantar, Charles Brown, John Seely, Guy R. Bennett, and Warren Hsing. High-energy x-ray microscopy techniques for laser-fusion plasma research at the National Ignition Facility. *Applied Optics*, 37(10):1784–1795, April 1998. Publisher: Optical Society of America.

[110] Yefim Aglitskiy, Thomas Lehecka, Stephen Obenschain, Stephen Bodner, Carl Pawley, Kent Gerber, John Sethian, Charles M. Brown, John Seely, Uri Feldman, and Glenn Holland. High-resolution monochromatic x-ray imaging system based on spherically bent crystals. *Applied Optics*, 37(22):5253–5261, August 1998. Publisher: Optical Society of America.

[111] J. A. Koch, Y. Aglitskiy, C. Brown, T. Cowan, R. Freeman, S. Hatchett, G. Holland, M. Key, A. MacKinnon, J. Seely, R. Snavely, and R. Stephens. 4.5- and 8-keV emission and absorption x-ray imaging using spherically bent quartz 203 and 211 crystals (invited). *Review of Scientific Instruments*, 74(3):2130–2135, March 2003. Publisher: American Institute of Physics.

[112] C. Stoeckl, G. Fiksel, D. Guy, C. Mileham, P. M. Nilson, T. C. Sangster, M. J. Shoup, and W. Theobald. A spherical crystal imager for OMEGA EP. *Review of Scientific Instruments*, 83(3):033107, March 2012. Publisher: American Institute of Physics.

[113] Daniel B. Sinars, Guy R. Bennett, David F. Wenger, Michael E. Cuneo, and John L. Porter. Evaluation of bent-crystal x-ray backlighting and microscopy techniques for the Sandia Z machine. *Applied Optics*, 42(19):4059–4071, July 2003. Publisher: Optical Society of America.

[114] P. Beiersdorfer, S. von Goeler, M. Bitter, K. W. Hill, R. A. Hulse, and R. S. Walling. High-resolution bent-crystal spectrometer for the ultrasoft x-ray region. *Review of Scientific Instruments*, 60(5):895–906, May 1989. Publisher: American Institute of Physics.

[115] G. Fiksel, F. J. Marshall, C. Mileham, and C. Stoeckl. Note: Spatial resolution of Fuji BAS-TR and BAS-SR imaging plates. *Review of Scientific Instruments*, 83(8):086103, August 2012. Publisher: American Institute of Physics.

[116] B. K. F. Young, A. L. Osterheld, D. F. Price, R. Shepherd, R. E. Stewart, A. Ya. Faenov, A. I. Magunov, T. A. Pikuz, I. Yu. Skobelev, F. Flora, S. Bollanti, P. Di Lazzaro, T. Letardi, A. Grilli, L. Palladino, A. Reale, A. Scafati, and L. Reale. High-resolution x-ray spectrometer based on spherically bent crystals for investigations of femtosecond laser plasmas. *Review of Scientific Instruments*, 69(12):4049–4053, December 1998. Publisher: American Institute of Physics.

[117] E. C. Harding, T. Ao, J. E. Bailey, G. Loisel, D. B. Sinars, M. Geissel, G. A. Rochau, and I. C. Smith. Analysis and implementation of a space resolving spherical crystal

spectrometer for x-ray Thomson scattering experiments. *Review of Scientific Instruments*, 86(4):043504, April 2015. Publisher: American Institute of Physics.

[118] R. A. Fonseca, L. O. Silva, F. S. Tsung, V. K. Decyk, W. Lu, C. Ren, W. B. Mori, S. Deng, S. Lee, T. Katsouleas, and J. C. Adam. OSIRIS: A Three-Dimensional, Fully Relativistic Particle in Cell Code for Modeling Plasma Based Accelerators. In Peter M. A. Sloot, Alfons G. Hoekstra, C. J. Kenneth Tan, and Jack J. Dongarra, editors, *Computational Science — ICCS 2002*, pages 342–351. Springer Berlin Heidelberg, 2002.

[119] James H. Easter, Aghapi G. Mordovanakis, Bixue Hou, Alexander GR Thomas, John A. Nees, Gérard Mourou, and Karl Krushelnick. High-order harmonic generation from solid targets with 2 mJ pulses. *Optics Letters*, 35(19):3186–3188, 2010.

[120] B. Dromey, D. Adams, R. Hörlein, Y. Nomura, S. G. Rykovanov, D. C. Carroll, P. S. Foster, S. Kar, K. Markey, and P. McKenna. Diffraction-limited performance and focusing of high harmonics from relativistic plasmas. *Nature Physics*, 5(2):146, 2009.

[121] Aghapi G. Mordovanakis, James Easter, Natalia Naumova, Konstantin Popov, Paul-Edouard Masson-Laborde, Bixue Hou, Igor Sokolov, Gérard Mourou, Igor V. Glazyrin, Wojciech Rozmus, Valery Bychenkov, John Nees, and Karl Krushelnick. Quasimonoenergetic Electron Beams with Relativistic Energies and Ultrashort Duration from Laser-Solid Interactions at 0.5 kHz. *Physical Review Letters*, 103(23):235001, December 2009.

[122] S. Mirzanejad and M. Salehi. Two-color high-order-harmonic generation: Relativistic mirror effects and attosecond pulses. *Physical Review A*, 87(6):063815, June 2013. Publisher: American Physical Society.

[123] Matthew R. Edwards, Victor T. Platonenko, and Julia M. Mikhailova. Enhanced attosecond bursts of relativistic high-order harmonics driven by two-color fields. *Optics Letters*, 39(24):6823–6826, December 2014. Publisher: Optical Society of America.

[124] Matthew R. Edwards and Julia M. Mikhailova. Waveform-Controlled Relativistic High-Order-Harmonic Generation. *Physical Review Letters*, 117(12):125001, September 2016. Publisher: American Physical Society.

[125] Matthew R. Edwards and Julia M. Mikhailova. Multipass relativistic high-order-harmonic generation for intense attosecond pulses. *Physical Review A*, 93(2):023836, February 2016. Publisher: American Physical Society.

[126] M. Yeung, S. Rykovanov, J. Bierbach, L. Li, E. Eckner, S. Kuschel, A. Woldegeorgis, C. Rödel, A. Sävert, G. G. Paulus, M. Coughlan, B. Dromey, and M. Zepf. Experimental observation of attosecond control over relativistic electron bunches with two-colour fields. *Nature Photonics*, 11(1):32–35, January 2017. Number: 1 Publisher: Nature Publishing Group.

[127] Zi-Yu Chen. Spectral control of high harmonics from relativistic plasmas using bicircular fields. *Physical Review E*, 97(4):043202, April 2018. Publisher: American Physical Society.

[128] Duan Xie, Yan Yin, Tongpu Yu, Hongyu Zhou, Ziyu Chen, and Hongbin Zhuo. High harmonic generation driven by two-color relativistic circularly polarized laser pulses at various frequency ratios. *Plasma Science and Technology*, 23(4):045502, March 2021. Publisher: IOP Publishing.

[129] Avner Fleischer, Ofer Kfir, Tzvi Diskin, Pavel Sidorenko, and Oren Cohen. Spin angular momentum and tunable polarization in high-harmonic generation. *Nature Photonics*, 8(7):543–549, July 2014. Number: 7 Publisher: Nature Publishing Group.

[130] Ofer Kfir, Patrik Grychtol, Emrah Turgut, Ronny Knut, Dmitriy Zusin, Dimitar Popmintchev, Tenio Popmintchev, Hans Nembach, Justin M. Shaw, Avner Fleischer, Henry Kapteyn, Margaret Murnane, and Oren Cohen. Generation of bright phase-matched circularly-polarized extreme ultraviolet high harmonics. *Nature Photonics*, 9(2):99–105, February 2015. Number: 2 Publisher: Nature Publishing Group.

[131] Daniel D. Hickstein, Franklin J. Dollar, Patrik Grychtol, Jennifer L. Ellis, Ronny Knut, Carlos Hernández-García, Dmitriy Zusin, Christian Gentry, Justin M. Shaw, Tingting Fan, Kevin M. Dorney, Andreas Becker, Agnieszka Jaroń-Becker, Henry C. Kapteyn, Margaret M. Murnane, and Charles G. Durfee. Non-collinear generation of angularly isolated circularly polarized high harmonics. *Nature Photonics*, 9(11):743–750, November 2015.

[132] J. Bromage, S.-W. Bahk, I. A. Begishev, C. Dorrer, M. J. Guardalben, B. N. Hoffman, J. B. Oliver, R. G. Roides, E. M. Schiesser, M. J. Shoup Iii, M. Spilatro, B. Webb, D. Weiner, and J. D. Zuegel. Technology development for ultraintense all-OPCPA systems. *High Power Laser Science and Engineering*, 7, 2019. Publisher: Cambridge University Press.

[133] K. U. Akli, R. B. Stephens, M. H. Key, T. Bartal, F. N. Beg, S. Chawla, C. D. Chen, R. Fedosejevs, R. R. Freeman, H. Friesen, E. Giraldez, J. S. Green, D. S. Hey, D. P. Higginson, J. Hund, L. C. Jarrott, G. E. Kemp, J. A. King, A. Kryger, K. Lancaster, S. LePape, A. Link, T. Ma, A. J. Mackinnon, A. G. MacPhee, H. S. McLean, C. Murphy, P. A. Norreys, V. Ovchinnikov, P. K. Patel, Y. Ping, H. Sawada, D. Schumacher, W. Theobald, Y. Y. Tsui, L. D. Van Woerkom, M. S. Wei, B. Westover, and T. Yabuuchi. Hot electron generation and transport using K$\upalpha$ emission. *Journal of Physics: Conference Series*, 244(2):022026, August 2010. Publisher: IOP Publishing.

[134] P. M. Nilson, A. A. Solodov, J. F. Myatt, W. Theobald, P. A. Jaanimagi, L. Gao, C. Stoeckl, R. S. Craxton, J. A. Delettrez, B. Yaakobi, J. D. Zuegel, B. E. Kruschwitz, C. Dorrer, J. H. Kelly, K. U. Akli, P. K. Patel, A. J. Mackinnon, R. Betti, T. C. Sangster, and D. D. Meyerhofer. Scaling hot-electron generation to long-pulse, high-intensity laser–solid interactions. *Physics of Plasmas*, 18(5):056703, May 2011.

[135] C. R. D. Brown, D. J. Hoarty, S. F. James, D. Swatton, S. J. Hughes, J. W. Morton, T. M. Guymer, M. P. Hill, D. A. Chapman, J. E. Andrew, A. J. Comley, R. Shepherd, J. Dunn, H. Chen, M. Schneider, G. Brown, P. Beiersdorfer, and J. Emig. Measurements of Electron Transport in Foils Irradiated with a Picosecond Time Scale Laser Pulse. *Physical Review Letters*, 106(18):185003, May 2011. Publisher: American Physical Society.

[136] M. Makita, G. Nersisyan, K. McKeever, T. Dzelzainis, S. White, B. Kettle, B. Dromey, D. Doria, M. Zepf, C. L. S. Lewis, A. P. L. Robinson, S. B. Hansen, and D. Riley. Fast electron propagation in Ti foils irradiated with sub-picosecond laser pulses at Iλ2>1018 Wcm-2μm2. *Physics of Plasmas*, 21(2):023113, February 2014. Publisher: American Institute of Physics.

[137] E. Martinolli, M. Koenig, S. D. Baton, J. J. Santos, F. Amiranoff, D. Batani, E. Perelli-Cippo, F. Scianitti, L. Gremillet, R. Mélizzi, A. Decoster, C. Rousseaux, T. A. Hall, M. H. Key, R. Snavely, A. J. MacKinnon, R. R. Freeman, J. A. King, R. Stephens, D. Neely, and R. J. Clarke. Fast-electron transport and heating of solid targets in high-intensity laser interactions measured by $K\ensuremath{\alpha}$ fluorescence. *Physical Review E*, 73(4):046402, April 2006. Publisher: American Physical Society.

[138] R. J. Garland, M. Borghesi, and A. P. L. Robinson. Analysis of the fast electron scaling theory for the heating of a solid target. *Physics of Plasmas*, 23(8):083116, August 2016. Publisher: American Institute of Physics.

[139] A. P. Shevelko, Yu. S. Kasyanov, O. F. Yakushev, and L. V. Knight. Compact focusing von Hamos spectrometer for quantitative x-ray spectroscopy. *Review of Scientific Instruments*, 73(10):3458–3463, September 2002. Publisher: American Institute of Physics.

[140] A. H. Gabriel. Dielectronic Satellite Spectra for Highly-Charged Helium-Like Ion Lines. *Monthly Notices of the Royal Astronomical Society*, 160(1):99–119, October 1972.

[141] S. H. Glenzer, C. A. Back, K. G. Estabrook, B. J. MacGowan, D. S. Montgomery, R. K. Kirkwood, J. D. Moody, D. H. Munro, and G. F. Stone. Electron temperature and density measurements in laser-produced large-scale-length gas-bag plasmas by x-ray spectroscopy. *Physical Review E*, 55(1):927–938, January 1997. Publisher: American Physical Society.

[142] F. Pisani, A. Bernardinello, D. Batani, A. Antonicci, E. Martinolli, M. Koenig, L. Gremillet, F. Amiranoff, S. Baton, J. Davies, T. Hall, D. Scott, P. Norreys, A. Djaoui, C. Rousseaux, P. Fews, H. Bandulet, and H. Pepin. Experimental evidence of electric inhibition in fast electron penetration and of electric-field-limited fast electron transport in dense matter. *Physical Review E*, 62(5):R5927–R5930, November 2000.

[143] Sophie D. Baton, Michel Koenig, Perceval Guillou, Bérénice Loupias, Alessandra Benuzzi-Mounaix, Julien Fuchs, Christophe Rousseaux, Laurent Gremillet, Dimitri

Batani, Alessio Morace, Motoaki Nakatsutsumi, Ryosuke Kodama, and Yefim Aglitskiy. Relativistic electron transport and confinement within charge-insulated, mass-limited targets. *High Energy Density Physics*, 3(3):358–364, October 2007.

[144] S. N. Chen, P. K. Patel, H.-K. Chung, A. J. Kemp, S. Le Pape, B. R. Maddox, S. C. Wilks, R. B. Stephens, and F. N. Beg. X-ray spectroscopy of buried layer foils irradiated at laser intensities in excess of 10^{20}W/cm^2. *Physics of Plasmas*, 16(6):062701, June 2009. Publisher: American Institute of Physics.

[145] Xiaohu Yang, Han Xu, Hongbin Zhuo, Yanyun Ma, Fuqiu Shao, Yan Yin, and Marco Borghesi. Effects of buried high-Z layers on fast electron propagation. *The European Physical Journal D*, 68(2):30, February 2014.

[146] F. F. Goryaev, L. A. Vainshtein, and A. M. Urnov. Atomic data for doubly-excited states 2lnl' of He-like ions and 1s2lnl' of Li-like ions with Z=6–36 and n=2,3. *Atomic Data and Nuclear Data Tables*, 113:117–257, January 2017.

[147] Marco Antonio Gigosos. Stark broadening models for plasma diagnostics. *Journal of Physics D: Applied Physics*, 47(34):343001, August 2014. Publisher: IOP Publishing.

[148] J. Stark and H. Kirschbaum. Beobachtungen über den Effekt des elektrischen Feldes auf Spektrallinien. III. Abhängigkeit von der Feldstärke. *Annalen der Physik*, 348(7):991–1016, 1914. _eprint: https://onlinelibrary.wiley.com/doi/pdf/10.1002/andp.19143480704.

[149] S. B. Hansen, J. Bauche, C. Bauche-Arnoult, and M. F. Gu. Hybrid atomic models for spectroscopic plasma diagnostics. *High Energy Density Physics*, 3(1):109–114, May 2007.

[150] J. Colgan, J. Abdallah, A. Ya. Faenov, S. A. Pikuz, E. Wagenaars, N. Booth, O. Culfa, R. J. Dance, R. G. Evans, R. J. Gray, T. Kaempfer, K. L. Lancaster, P. McKenna, A. L. Rossall, I. Yu. Skobelev, K. S. Schulze, I. Uschmann, A. G. Zhidkov, and N. C. Woolsey. Exotic Dense-Matter States Pumped by a Relativistic Laser Plasma in the Radiation-Dominated Regime. *Physical Review Letters*, 110(12):125001, March 2013. Publisher: American Physical Society.

[151] P. M. Nilson, W. Theobald, J. Myatt, C. Stoeckl, M. Storm, O. V. Gotchev, J. D. Zuegel, R. Betti, D. D. Meyerhofer, and T. C. Sangster. High-intensity laser-plasma interactions in the refluxing limit. *Physics of Plasmas*, 15(5):056308, May 2008.

[152] S. B. Hansen and A. S. Shlyaptseva. Effects of the electron energy distribution function on modeled x-ray spectra. *Physical Review E*, 70(3):036402, September 2004. Publisher: American Physical Society.

[153] David R. Lide. *CRC Handbook of Chemistry and Physics*. CRC Press, 84 edition, 2003.